1 **Myristoylated Neuronal Calcium Sensor-1 captures the ciliary vesicle at distal appendages**

2

3 Tomoharu Kanie[1,2,4], Roy Ng[1], Keene L. Abbott[1], Olaf Pongs[3], and Peter K. Jackson[1,4]

4

5

6 [1]Baxter Laboratory, Department of Microbiology & Immunology and Department of Pathology,

7 Stanford University, Stanford, CA, 94305

8 [2]Department of Cell Biology, University of Oklahoma Health Sciences Center, Oklahoma, OK,

9 73112

10 [3]Institute for Physiology, Center for Integrative Physiology and Molecular Medicine (CIPPM),

11 Saarland University, Homburg, Germany

12 [4]Corresponding authors

13   **Summary** (230 Words)

14   The primary cilium is a microtubule-based organelle that cycles through assembly and

15   disassembly. In many cell types, formation of the cilium is initiated by recruitment of ciliary

16   vesicles to the distal appendage of the mother centriole. However, the distal appendage

17   mechanism that directly captures ciliary vesicles is yet to be identified. In an accompanying

18   paper, we show that the distal appendage protein, CEP89, is important for thef ciliary vesicle

19   recruitment, but not for other steps of cilium formation (Tomoharu Kanie, Love, Fisher,

20   Gustavsson, & Jackson, 2023). The lack of a membrane binding motif in CEP89 suggests that it

21   may indirectly recruit ciliary vesicles via another binding partner. Here, we identify Neuronal

22   Calcium Sensor-1 (NCS1) as a stoichiometric interactor of CEP89. NCS1 localizes to the

23   position between CEP89 and a ciliary vesicle marker, RAB34, at the distal appendage. This

24   localization was completely abolished in CEP89 knockouts, suggesting that CEP89 recruits

25   NCS1 to the distal appendage. Similarly to CEP89 knockouts, ciliary vesicle recruitment as well

26   as subsequent cilium formation was perturbed in NCS1 knockout cells. The ability of NCS1 to

27   recruit the ciliary vesicle is dependent on its myristoylation motif and NCS1 knockout cells

28   expressing myristoylation defective mutant failed to rescue the vesicle recruitment defect despite

29   localizing proper localization to the centriole. In sum, our analysis reveals the first known

30   mechanism for how the distal appendage recruits the ciliary vesicles.

Introduction

The primary cilium is an organelle that consists of the microtubule-based axoneme surrounded

by the ciliary membrane, which accumulates specific membrane proteins (e.g., G-protein

coupled receptors) to serve as a sensor for extracellular environmental cues (Reiter & Leroux,

2017). The cilium extends from the mother centriole, and cycles assembly and disassembly, as

the cell needs to disassemble the cilium prior to mitosis (Vorobjev & Chentsov Yu, 1982) to

allow the centrosome to function within the spindle pole during mitosis. The processes of the

cilium formation were described in great detail through electron microscopy by Sergei Sorokin

in 1960s (S. Sorokin, 1962) (S. P. Sorokin, 1968) and is known to be subdivided to two types

called the extracellular and intracellular pathways (Molla-Herman et al., 2010). In the

extracellular pathway used, for example, by mouse inner medullary collecting duct cells

(mIMCD3 cells), the mother centriole is believed to first dock to the plasma membrane before

the extension of the axonemal microtubule as well as ciliary membrane (Molla-Herman et al.,

2010). In the intracellular pathway used, for example, by Retinal Pigment Epithelia (RPE) cells

(Molla-Herman et al., 2010) and fibroblasts (S. Sorokin, 1962) (Molla-Herman et al., 2010), the

first step of cilium formation is attachment of the small vesicles, or so-called ciliary vesicles, to

the distal end of the mother centriole (S. Sorokin, 1962), or more specifically to the distal

appendage (Schmidt et al., 2012; Sillibourne et al., 2013). The distal appendage is a nine-fold

blade-like structure attached to the distal end of the mother centriole (Anderson, 1972; Bowler et

al., 2019; Paintrand, Moudjou, Delacroix, & Bornens, 1992). The ciliary vesicle recruitment is

followed by the fusion of the small vesicles (Lu et al., 2015), removal of CP110 (Lu et al., 2015),

which is believed to cap the distal end of the mother centriole (Spektor, Tsang, Khoo, &

Dynlacht, 2007), and subsequently axonemal extension, which is mediated at least partially by

54   intraflagellar transport (IFT) (Craft, Harris, Hyman, Kner, & Lechtreck, 2015). While the distal

55   appendage is indispensable for all those steps, how exactly the distal appendage controls these

56   multiple processes is largely unknown.

57   To understand the molecular roles of the distal appendage, we first need to uncover its

58   molecular composition and identify critical functions of distal appendage proteins. In an

59   accompanying paper, we comprehensively analyzed all known distal appendage proteins to date

60   and revealed that the Centrosomal Protein 89 (CEP89) is important for ciliary vesicle

61   recruitment, but not for other processes organizing cilium formation (Tomoharu Kanie et al.,

62   2023). Since CEP89 lacks apparent lipid binding motifs, we hypothesized that an interacting

63   partner of CEP89 may bind to ciliary vesicle directly. We sought to identify and understand the

64   protein directly recruiting the ciliary vesicle.

65   **Results**

66   **Discovery of Neuronal Calcium Sensor-1 as a stoichiometric interactor of CEP89**

67   To identify interacting partners of CEP89, we performed tandem affinity purification and mass

68   spectrometry (TAP-MS) (Rigaut et al., 1999). Localization and affinity purification (LAP)

69   (Cheeseman & Desai, 2005) tagged CEP89 was expressed in retinal pigment epithelia

70   immortalized with human telomerase (RPE-hTERT), and CEP89 was immunoprecipitated first

71   by Green Fluorescent Protein (GFP) antibody beads followed by a second affinity precipitation

72   by S protein beads. Final eluates were resolved by SDS-PAGE gel and analyzed by silver-

73   staining (Figure 1A) and mass spectrometry (Figure 1B). This analysis identified two

74   stoichiometric interactors, Neuronal Calcium Sensor-1 (NCS1) and C3ORF14, consistent with

75   the previous high-throughput proteome analyses, which identified both proteins as either CEP89

76   interactors (Huttlin et al., 2021) or neighbors (Gupta et al., 2015). Consistent with the TAP-MS

77 data, endogenous NCS1 strongly coimmunoprecipitated with endogenous CEP89 (Figure 1-

78 figure supplement 1A).

79   NCS1 is a member of NCS family proteins, which are characterized as containing

80 calcium binding EF-hand motifs as well as a myristoylation signal for N-terminal addition of

81 myristate (Burgoyne & Weiss, 2001). NCS1 was first identified as Frequenin in Drosophila, a

82 protein that can facilitate neurotransmitter release in neuromuscular junction (Pongs et al., 1993).

83 Since then, numerous papers propose models wherein NCS1 is involved in both presynaptic and

84 postsynaptic functions (reviewed in (Dason, Romero-Pozuelo, Atwood, & Ferrus, 2012)).

85 However, how exactly NCS-1 regulates neuronal function is still not well understood. As

86 described later in this paper, NCS-1 is expressed ubiquitously in various tissues, consistent with

87 the previous report (Gierke et al., 2004). While the previous literatures reported the role of NCS1

88 in other cell types including cardiomyocytes (Nakamura, Jeromin, Mikoshiba, & Wakabayashi,

89 2011) and adipocytes (Ratai, Hermainski, Ravichandran, & Pongs, 2019), molecular mechanisms

90 regulating non-neuronal functions of NCS1 remains enigmatic. A centrosomal role of NCS1 has

91 never been described.

92   CEP89 binding to NCS1 required the N-terminal region (1-343a.a.) (Figure 1C and D).

93 The C-terminal portion of CEP89 (344-783a.a.) is required for its centrosomal localization

94 (Figure 1- figure supplement 1B), consistent with a previous report (Sillibourne et al., 2013). An

95 *in vitro* binding assay using *in vitro* translated proteins revealed that HA tagged CEP89 directly

96 binds to MYC tagged C3ORF14 and NCS1 (Figure 1E), whereas HA-C3ORF14 did not bind to

97 NCS1 (Figure 1F). A negative control, CEP350 fragment (2470-2836 a.a.), which binds to its

98 binding partner FGFR1OP (or FOP) efficiently (Figure 1-figure supplement 2A) as previously

99 described (T. Kanie et al., 2017), did not bind to either HA-CEP89, nor HA-C3ORF14 (Figure

100   1E and F). Thus, CEP89 serves to bridge NCS1 and C3ORF14 (Figure 1G).

101

102   **NCS1 is recruited to the distal appendage by CEP89 and is positioned between CEP89 and**

103   **the ciliary vesicle marker, RAB34**

104   We next sought to determine the precise localization of NCS1 and C3ORF14. When observed

105   via a wide-field microscopy, NCS1 localized to the mother centriole, marked by CEP170 (Figure

106   2A). Some cytoplasmic staining was also observed. Both centriolar and cytoplasmic staining was

107   highly specific as the signal was strongly reduced in NCS1 knockout cells (Figure 2A). The

108   cytoplasmic localization of NCS1 is inconsistent with a previous study, where C-terminally

109   Enhanced Yellow Fluorescent Protein (EYFP) tagged NCS1 constitutively localized to

110   membranous compartments (O'Callaghan et al., 2002). We tested if the difference in localization

111   is due to the tagging. We also tested whether membrane binding, myristoylation motif, of NCS1

112   affects its localization by making the myristoylation defective mutant by converting the position

113   2 glycine to alanine (NCS1-G2A). N-terminally LAP (EGFP and S) tagged wild-type or G2A

114   mutant of NCS1 localized to mother centriole as well as cytoplasm, similar to endogenous NCS1

115   (Figure 2- figure supplement 1A and B). Consistent with the previous paper (O'Callaghan et al.,

116   2002), C-terminally LAP tagged wild-type NCS1 localized to membrane compartments, such as

117   plasma membrane and endoplasmic reticulum, whereas the myristoylation defective mutant

118   (G2A) diffusely localized to cytoplasm (Figure 2-figure supplement 1C and D). This result

119   suggests that C-terminal tagging of NCS1 changes its localization potentially via exposing the

120   myristoylation motif of NCS1, and endogenous NCS1 may sequester its myristoylation motif to

121   allow localization to cytoplasm. A small amount of nuclear localization observed in LAP tagged

122   NCS1 likely derives from LAP tagging (Figure 2- figure supplement 1), as the endogenous

123   NCS1 did not localize to nucleus (Figure 2A). Similar to NCS1, C-terminally LAP tagged

124   C3ORF14 localized to the location between acetylated tubulin, a cilium marker, and Pericentrin,

125   a centrosome marker, suggesting that it also localizes specifically to the mother centriole (Figure

126   2B). NCS1 localization to the mother centriole was enhanced upon serum deprivation (Figure

127   2C), a condition that induces cilium formation in RPE cells, much like several other distal

128   appendage proteins (see Figure 1D of (Tomoharu Kanie et al., 2023)). When observed via 3D

129   structured illumination microscopy, of which resolution is twice as high as a diffraction limited

130   microscopy (Y. Wu & Shroff, 2018), C-terminally LAP (EGFP-S) tagged C3ORF14 localized to

131   a position slightly distal to the distal appendage protein, CEP164, in side-view (Figure 2D).

132   When top (or axial) view of the mother centriole was visualized, LAP-C3ORF14 formed a ring-

133   like structure that is slightly smaller than the CEP164 ring (Figure 2E), which is reminiscent of

134   the 9-fold symmetrical structure of the distal appendage (Paintrand et al., 1992). Similarly, NCS1

135   localized slightly distal to CEP164 (Figure 2F) as well as the binding partner, CEP89 (Figure

136   2G), and slightly proximal to the ciliary vesicle marker, RAB34 (Stuck, Chong, Liao, & Pazour,

137   2021) (Tomoharu Kanie et al., 2023) (Figure 2H). Like C3ORF14, NCS1 formed a slightly

138   smaller ring than CEP164 (Figure 2I). Consistent with this, the ring diameter of NCS1 and

139   C3ORF14 was 319.5±7.7 nm (n=13, average±SEM) and 348.8±8.0 nm (n=16, average±SEM),

140   respectively (see Figure 1C of (Tomoharu Kanie et al., 2023)). It is notable that both C3ORF14

141   and NCS1 also localized to the region close to subdistal appendage in some but not all centrioles

142   (Figure 2D and F), consistent with what was observed for CEP89 localization (Chong et al.,

143   2020). This near subdistal appendage localization explains why C3ORF14 was previously

144   classified as a subdistal appendage protein (Gupta et al., 2015). These results suggest that NCS1

145   localizes to the distal appendage and more precisely to the position sandwiched between CEP89

146   and the ciliary vesicle (Figure 2J).

147   We next determined the hierarchy of the three proteins. Centriolar localization of CEP89 was not

148   affected by depletion of either NCS1 nor C3ORF14 (Figure 2K and Figure 2-figure supplement

149   2A). NCS1 failed to localize to the mother centriole without altering its cytoplasmic localization

150   in CEP89 knockout cells but not in C3ORF14 knockout cells (Figure 2L and Figure 2-figure

151   supplement 2B), indicating that CEP89 recruits NCS1 to the distal appendage. The lack of NCS1

152   localization at the centriole in CEP89 knockouts cells was rescued by expressing untagged

153   CEP89 (Figure 2L and Figure 2- figure supplement 2B). C3ORF14 localization required CEP89,

154   but not NCS1 (Figure 2M and Figure 2- figure supplement 2C). The expression level of neither

155   NCS1, nor C3ORF14 was affected by CEP89 depletion (Figure 2- figure supplement 2D and E).

156   These results suggest that both NCS1 and C3ORF14 are recruited to the distal appendage by

157   CEP89 (Figure 2N). We also tested whether the three proteins affect localization of other distal

158   appendage proteins and found that the localization of other distal appendage proteins were

159   unchanged in cells deficient in CEP89, NCS1, or C3ORF14 (Figure 2-figure supplement 3A-C)

160   (see also Figure 2A-L of (Tomoharu Kanie et al., 2023)). Similar to the centriolar localization of

161   CEP89, which was significantly reduced in CEP83 or SCLT1 knockouts, NCS1 localization was

162   also greatly diminished in these knockouts (Figure 2-figure supplement 3D). This is consistent

163   with the observation that CEP83-SCLT1 module serves as a structural component of the distal

164   appendage (see (Tomoharu Kanie et al., 2023) for the detail). In contrast, the feedback complex

165   CEP164-TTBK2 (see (Tomoharu Kanie et al., 2023) for the detail) was required for proper

166   centriolar localization of NCS1 (Figure 2- figure supplement 3D) but not for CEP89 (Figure 2F

167   of (Tomoharu Kanie et al., 2023)). Given that CEP89 is a substrate of TTBK2 (Bernatik et al.,

168   2020; Lo et al., 2019), this might suggest that phosphorylation of TTBK2 could affect the

169   interaction between CEP89 and NCS1. It is also possible that NCS1 may be a phosphorylation

170   target of TTBK2. These questions warrant future investigation.

171

172   **NCS1 is important for efficient ciliary vesicle recruitment at the distal appendage**

173   We next sought to understand the role of NCS1 at the distal appendage and performed kinetic

174   analysis of ciliation in control (sgGFP) and knockouts of CEP89, NCS1, or C3ORF14 in RPE

175   cells, in which serum starvation induces cilium formation (Figure 3A). Control RPE cells form

176   cilia over 24 hours after serum starvation, and almost of all cells completed cilium formation

177   between 24 and 48 hours. CEP89 and NCS1 knockouts displayed a notable delay in initiating

178   ciliation (see 12-hour in Figure 3A), but gradually catch up on ciliogenesis and exhibited only

179   mild ciliary formation defects at later time points (see 48 hours in Figure 3A). The cilium

180   formation defect was rescued by expressing untagged CEP89 in CEP89 knockouts or untagged

181   NCS1 in NCS1 knockouts (Figure 3B). This kinetic defect is strongly consistent with the

182   knockouts of several other distal appendage proteins, namely ANKRD26 and FBF1 (Figure 5A

183   and B of (Tomoharu Kanie et al., 2023)). Consistent with the cells deficient in ANKRD26 or

184   FBF1 (see Figure 5- figure supplement 1 of (Tomoharu Kanie et al., 2023)), ciliary ARL13B

185   signal intensity was reduced in CEP89 or NCS1 knockouts even after the cells complete cilium

186   formation (Figure 3-figure supplement 1A-C). This suggests that even though the NCS1 or

187   CEP89 knockouts can eventually form primary cilia, those cilia may be functionally different

188   from wild-type cilia. C3ORF14 knockouts showed similar but much milder kinetic defect of

189   cilium formation than CEP89 or NCS1 knockouts, therefore, we focused on NCS1 in the

190   subsequent investigation.

191   We then sought to understand how NCS1 is involved in cilium formation. In an

192 accompanying paper (Tomoharu Kanie et al., 2023), we showed that CEP89 participates in

193 cilium formation by regulating ciliary vesicle recruitment without affecting IFT88::CEP19

194 recruitment, important steps that require distal appendage proteins (Schmidt et al., 2012)

195 (Dateyama et al., 2019)(see Figure 5 of (Tomoharu Kanie et al., 2023)). We tested if NCS1 has

196 similar roles to its binding partner, CEP89. Indeed, NCS1 knockouts exhibited moderate ciliary

197 vesicle recruitment defect, similar to CEP89 knockouts, when assessed using RAB34 as a ciliary

198 vesicle marker (Figure 3C). Transmission electron microscopy analysis confirmed the ciliary

199 vesicle recruitment defect in NCS1 knockouts (Figure 3D and E). The presence of fused vesicles,

200 albeit much lower percentage than control cells, in NCS1 knockouts (Figure 3D and E) suggests

201 that NCS1 is important for recruitment but not fusion of the ciliary vesicle. Removal of CP110,

202 which is believed to act as a cap of axonemal microtubule, was partially, but measurably affected

203 in NCS1 knockout cells (Figure 3F), consistent with the fact that CP110 removal is in part

204 downstream of ciliary vesicle recruitment (Figure 4D of (Tomoharu Kanie et al., 2023)). Neither

205 IFT88 nor CEP19 recruitment to the centriole was affected in NCS1 knockout cells (Figure 3G

206 and H). These results suggest that NCS1 plays an important role in cilium formation by

207 regulating ciliary vesicle recruitment, but not other known processes of cilium formation,

208 consistent with the role of CEP89 in ciliary vesicle recruitment.

209 **Yet unknown distal appendage proteins may compensate the lack of NCS1 in ciliary vesicle**

210 **recruitment**

211 As we showed in an accompanying paper, the distal appendage is indispensable for the

212 recruitment of the ciliary vesicle to the mother centriole. Virtually no RAB34 positive ciliary

213 vesicle was observed at mother centriole in cells deficient in CEP164, CEP83, or TTBK2, which

214 are critical for structural integrity of the distal appendage (Figure 5C of (Tomoharu Kanie et al.,

215 2023)). This phenotype is much stronger than what we observed in CEP89 or NCS1 knockouts

216 (Figure 3C), suggesting that some other distal appendage proteins may compensate the lack of

217 NCS1 for the ciliary vesicle recruitment. To address this question, we created cells lacking both

218 NCS1 and each of the other distal appendage proteins (FBF1, CEP89, ANKRD26, KIZ,

219 LRRC45) as well as the distal appendage associated protein, INPP5E (Figure 4A). We omitted

220 the integral components of the distal appendage proteins (CEP164, TTBK2, CEP83, SCLT1)

221 from the analysis, as the knockouts of these proteins showed very strong ciliary vesicle

222 recruitment defects on their own, therefore making it difficult to test if the NCS1 depletion

223 shows additive effects. Cilium formation assay revealed that depletion of NCS1 decreased the

224 percentage of ciliated cells in each single knockout cells, except CEP89 (Figure 4B and C). This

225 suggests that CEP89, but no other distal appendage protein regulates the same ciliary formation

226 pathway as NCS1. Similarly, depletion of NCS1 decreased the RAB34 positive centriole in each

227 of the single distal appendage knockout cells, except CEP89 knockouts (Figure 4D). These

228 results suggest that yet unknown distal appendage proteins would be required to compensate for

229 the ciliary vesicle recruitment defect of NCS1 knockout cells. Another possibility is that one or

230 more integral components (CEP164, TTBK2, SCLT1, and CEP83) may be directly involved in

231 ciliary vesicle recruitment. These hypotheses warrant future investigation.

232 **NCS1 captures ciliary vesicle via its myristoylation motif**

233 Since NCS1 is myristoylated, we wondered whether the membrane association motif is

234 necessary for NCS1 to recruit the ciliary vesicle. We tested this hypothesis by creating a

235 myristoylation defective mutant (NCS1-G2A). We tested whether the mutant indeed lost the

236 ability to bind membrane using differential centrifugation following nitrogen cavitation. We first

237 determined which fraction is the most optimal to assess membrane association in our

11

238   experimental setting. While the microsomal fraction prepared from the pellet following

239   ultracentrifugation at 100,000 g is often used to analyze membrane fraction of the cells (Graham,

240   2015), the plasma membrane marker, Epidermal Growth Factor Receptor (EGFR), was enriched

241   mostly in the pellet following centrifugation at 15,000 *g* in our experiment (Figure 5A; see

242   Methods for further explanation of the technical design). In addition, NCS1-G2A was

243   fractionated in the 100,000 *g* pellet to similar extent as wild-type NCS1 (Figure 5A), indicating

244   that centrifugation at 100,000 *g* may also pellet some soluble proteins, even though cytoplasmic

245   protein RabGDI remained in the 100,000 *g* supernatant. Thus, we decided to use 15,000 *g* pellet

246   to assess membrane fraction in our experiment. In control cells (sgSafe), both NCS1 and CEP89

247   was found in both soluble fraction (15,000 *g* supernatant) and membrane fraction (15,000 *g*

248   pellet) (Figure 5A). In contrast, NCS1-G2A was only found in the soluble fraction (15,000 *g*

249   supernatant) (Figure 5A), suggesting that myristoylation is required for membrane localization of

250   NCS1. Interestingly, CEP89 was only found in the soluble fraction (15,000 *g* supernatant) in

251   NCS1 knockout cells expressing either empty vector or NCS1-G2A, but not NCS1-WT. This

252   suggests that membrane localization of CEP89 requires NCS1 with an intact myristoylation

253   motif. When expressed at similar level to endogenous NCS1 (Figure 5B), both wild-type and the

254   myristoylation defective (G2A) NCS1 localizes to the mother centriole to a similar extent

255   (Figure 5C and D). However, the myristoylation defective mutant almost completely failed to

256   rescue ciliation and ciliary vesicle recruitment defect of NCS1 knockout cells (Figure 5E and F).

257   These data suggest that NCS1 recruits ciliary vesicle to the distal appendage via its

258   myristoylation motif (Figure 5G).

259   **Calcium binding is needed for stability of NCS1**

260   In addition to myristoylation motif, human NCS1 also has three functional and one apparently

12

261 non-functional (due to the mutation in critical amino acids needed for co-ordination bond with

262 calcium) EF-hand motifs (Bourne, Dannenberg, Pollmann, Marchot, & Pongs, 2001). Several

263 other NCS family proteins, including Recoverin and Hippocalcin, show a calcium-myristoyl

264 switch (Ames et al., 1997; O'Callaghan, Tepikin, & Burgoyne, 2003). In this mechanism, the

265 sequestered myristoylation motif is exposed to allow the protein to bind membrane upon calcium

266 binding. It has been proposed that NCS1 may employ a similar molecular switch. While the

267 structure of fission yeast Ncs1, solved by nuclear magnetic resonance spectroscopy showed the

268 calcium-myristoyl switch (Lim, Strahl, Thorner, & Ames, 2011), several lines of evidence

269 suggest the absence of that type of switch in budding yeast and mammalian NCS1(Ames et al.,

270 2000; O'Callaghan et al., 2002) (Lemire, Jeromin, & Boisselier, 2016). Since a myristoylation

271 defective mutant of NCS1 failed to form cilia efficiently without affecting its centrosomal

272 localization (Figure 5C and E), we tested if there is a calcium-myristoylation switch by making

273 various EF-hand mutations, where each or combination of the three active EF-hand motif was

274 disabled by mutating invariant glutamate at -Z position to glutamine (E84Q for the 1st, E120Q

275 for the 2nd, and E168Q for the 3rd active EF-hand mutation). We expressed *wild type* or EF-hand

276 mutants of untagged NCS1 in NCS1 knockout cells and detected the expression and the

277 localization of each mutant using α-NCS1 antibody. The wild-type and the mutants of NCS1

278 were functionally tested via ciliation assay rather than the ciliary vesicle recruitment assay,

279 because the ciliation assay is much less variable than the vesicle recruitment assay. Although the

280 E84Q mutant as well as any double and triple EF-hand mutants were highly destabilized (See

281 input in Figure 5- figure supplement 1A), centriolar NCS1 signal intensity of the mutant was

282 reduced in parallel to its diminished expression level. This suggests that the first EF hand is

283 indispensable for stability of NCS1. E120Q mutant had similar expression level, but its

284   centrosomal signal was significantly reduced (Figure 5- figure supplement 1B), consistent with

285   its diminished interaction with CEP89 (see IP: GFP in Figure 5- figure supplement 1A), a protein

286   that recruits NCS1 to the mother centriole (Figure 2L). This suggests that the second EF-hand is

287   involved in keeping its structure to interact with CEP89. E168Q had a negligible effect in

288   stability and localization of NCS1. The ciliation assay revealed that none of single EF-hand

289   mutants showed significant cilium formation defect (Figure 5- figure supplement 1C) despite the

290   partial reduction of centriolar signal intensity for E84Q and E120Q. The double or triple mutants

291   almost completely failed to rescue ciliation defect of NCS1 knockout cells (Figure 5-figure

292   supplement 5C), reflecting their very low expression level (Figure 5-figure supplement 1A).

293   These results suggest that calcium binding is primarily required for the structure and stability of

294   NCS1 and NCS1 does not clearly exhibit a calcium-myristoylation switch. The structural role of

295   calcium on NCS1 is largely consistent with NCS1's high binding affinity to calcium (-90 nM)

296   (Aravind et al., 2008).

297   **NCS1 is recruited to the centriole in a microtubule-independent manner where it captures**

298   **ciliary vesicles**

299   We next sought to understand where NCS1 captures ciliary vesicle. One possibility is that NCS1

300   captures the ciliary vesicle in the cytoplasm and then traffics it to the centriole by dynein-

301   dependent transport via microtubule. Another possibility is that NCS1 traffics to the centriole

302   first and then captures ciliary vesicles. To distinguish these two possibilities, we treated RPE

303   cells with nocodazole to destabilize microtubules, as microtubules were previously shown to be

304   indispensable for ciliary vesicle recruitment (C. T. Wu, Chen, & Tang, 2018). Consistent with

305   the previous report (C. T. Wu et al., 2018), destabilization of microtubule by nocodazole (Figure

306   6A and B) immediately inhibited ciliary vesicle recruitment and subsequent cilium formation

14

307   (Figure 6C and D), suggesting that ciliary vesicles are trafficked to the mother centriole via

308   microtubules. In contrast, centriolar NCS1 signal was gradually increased upon serum starvation

309   even in the presence of nocodazole (Figure 6E), suggesting that NCS1 accumulates at the distal

310   appendage by microtubule-independent mechanisms, possibly by diffusion, similar to the

311   previously proposed diffusion-to-capture model of IFT trafficking to the ciliary base (Hibbard,

312   Vazquez, Satija, & Wallingford, 2021). Because NCS1 is an N-terminally myristoylated protein,

313   we also considered whether NCS1 might be trafficked to the distal appendage through UNC119,

314   a chaperone that binds to N-myristoylated ciliary proteins like NPHP3 and cystin and traffics

315   them to the primary cilium (K. J. Wright et al., 2011). We conclude that NCS1 unlikely uses

316   UNC119 pathway, as we did not observe UNC119A/UNC119B in our AP/MS analysis of

317   CEP89 (Figure 1B-Source Data), nor in purifications of UNC119A/UNC119B proteins

318   themselves (K. J. Wright et al., 2011). In a complementary approach to the microtubule

319   destabilization, we tested if NCS1 localizes to the distal appendage even if the ciliary vesicle

320   recruitment is inhibited by RAB34 depletion (see Figure 4B and C of (Tomoharu Kanie et al.,

321   2023)). We confirmed that centriolar NCS1 was comparable between control (sgSafe) and

322   RAB34 knockout cells (Figure 6F), suggesting that NCS1 is recruited to the centriole

323   independently from the ciliary vesicle. These results suggest that NCS1 moves to the distal

324   appendage possibly by diffusion or an alternative trafficking mechanism and there it captures the

325   ciliary vesicle that is trafficked to the centriole by microtubule-dependent trafficking.

326   **NCS1 localizes to the ciliary base in neuronal and non-neuronal cells**

327   While the majority of papers to date focused on the role of NCS1 in neurons given its original

328   discovery as a protein that facilitates neurotransmitter release (Pongs et al., 1993), expression

329   analysis revealed that the protein is expressed ubiquitously in non-neuronal tissues (Gierke et al.,

330   2004). Since we discovered that NCS1 localizes to the centriole, a major microtubule organizing

331   center in animal cells (Bornens, 2012), we tested the expression and the localization of NCS1 in

332   neuronal and non-neuronal cell types. We first tested the expression of NCS1 in various murine

333   tissues and confirmed that NCS1 is expressed in a wide-range of tissues (Figure 7-figure

334   supplement 1A). The low expression level of NCS1 in liver, skeletal muscle, and fat might

335   reflect that most of the cells (hepatocyte, myocyte, and adipocytes, respectively) in those tissues

336   do not retain cilia, or because of the difference in ratio between intracellular and extracellular

337   proteins. When we performed immunofluorescence assay, NCS1 localized to both cytoplasm and

338   the ciliary base (a dot next to ciliary markers, ARL13B or AC3) in isolated hippocampal neuron

339   (top panel in Figure 7A) as well as cells in hypothalamus (Figure 7B) and the dentate gyrus of

340   the hippocampus (Figure 7-figure supplement 2C). Both cytoplasmic and the centriole signal was

341   specific for NCS1 as we detected no signal in NCS1 knockout cells (bottom panel in Figure 7A

342   and B, and Figure 7-figure supplement 2C). NCS1 also localized to the ciliary base in virtually

343   all the non-neuronal ciliated cells that we tested, including kidney epithelia, pancreatic islet cells,

344   airway epithelia, ependymal cells, and mouse embryonic fibroblasts (MEFs) (Figure 7C and D,

345   Figure 7-figure supplement 2A-D). Only ciliated cells where we failed to detect NCS1 at the

346   ciliary base was photoreceptor cells (Figure 7-figure supplement 2E). We next sought to

347   determine whether NCS1 is involved in cilium formation in those cells, as we saw in RPE cells

348   (Figure 3A and B). In MEFs, cilium formation is modestly perturbed in Ncs1 depleted cells

349   (Figure 7E and F), consistent with the kinetic cilium formation defect in RPE cells (Figure 3A).

350   Decrease in ciliary ARL13B signal was also detected in $Ncs1^{-/-}$ MEFs (Figure 7F), similar to

351   NCS1 knockout RPE cells (Figure 3-figure supplement 1). In contrast, we did not detect a

352   measurable cilium formation defect in hippocampal neurons that lack Ncs1 (Figure 7G), whereas

16

353 the signal of ciliary membrane protein, type III adenylyl cyclase (ADCY3) (Bishop, Berbari,

354 Lewis, & Mykytyn, 2007) (Berbari, Bishop, Askwith, Lewis, & Mykytyn, 2007), was

355 significantly decreased (Figure 7H). Other ciliary GPCRs, such as SSTR3 and GPR161, were

356 also decreased in *Ncs1$^{-/-}$* neurons, but did not show statistical significance with the small number

357 of samples analyzed (Figure 7-fiure supplement 3A and B). The difference in the cilium

358 formation defect in different cell types (modest ciliation defects in RPE and MEFs, but no defect

359 in neurons) as well as potential signaling function of NCS1 will be discussed in the Discussion.

360 **_Ncs1_ knockout mice exhibit obesity, but not other phenotypes related to ciliopathies**

361   To date, NCS1 has been characterized mainly in neuronal aspects, as NCS1 was classically

362 believed to be a neuron-specific calcium sensor (Olafsson et al., 1997). Ncs1 was shown to be

363 essential for memory formation in C. elegans. Mice lacking Ncs1 exhibited impairment of

364 memory formation (de Rezende et al., 2014; Saab et al., 2009) (Nakamura et al., 2017). Since

365 NCS1 is now shown to localize to the distal appendage in both neuronal and non-neuronal cells

366 and regulate efficient cilium formation at least in some cell types, we sought to test if *Ncs1*

367 knockout mice show phenotypes related to ciliopathies, pleiotropic disorders caused by

368 functional and structural dysfunction of cilia (Reiter & Leroux, 2017). A series of previous

369 mouse genetic studies showed that the loss of ciliary function in mice result in partially penetrant

370 pre-weaning lethality, obesity, retinal degeneration, and male infertility (Nishimura et al., 2004)

371 (Ding et al., 2020; Fath et al., 2005; Mykytyn et al., 2004). We assessed whether the previously

372 generated *Ncs1$^{-/-}$* mice (Hermainski, 2012; Ng et al., 2016) exhibit ciliopathy phenotypes.

373 Inconsistent with the previous two reports (Nakamura et al., 2011) (Dickinson et al., 2016),

374 which generated *Ncs1* knockout mice independently, our *Ncs1$^{-/-}$* mice did not exhibit pre-

375 weaning lethality (Figure 7A, p=0.369 in Chi-square test in data with male and female

17

376   combined). The difference between our data and the previous studies might derive from the

377   background of mice (C57BL6/J in our study and C57BL6/N in the previous studies). When body

378   weight was analyzed, both male and female $Ncs1^{-/-}$ mice became more obese than their

379   littermates starting at 9-10 weeks of age, and gained 10% more weight than the controls at 20

380   weeks (Figure 7B-C). The obesity phenotype is consistent with the previous reports (Nakamura

381   et al., 2011; Ratai et al., 2019) and is similar to what was observed in cilia-defective mice, which

382   became obese starting between 8-12 weeks (Ding et al., 2020; Fath et al., 2005; Mykytyn et al.,

383   2004; Nishimura et al., 2004). $Ncs1^{-/-}$ accumulated more fat than their littermate $Ncs1^{+/-}$ mice,

384   suggesting that the obesity phenotype at least partially comes from the increased fat amount in

385    $Ncs1^{-/-}$ mice. We also assessed other ciliopathy phenotypes, but $Ncs1^{-/-}$ did not show other cilia-

386   related symptoms, such as retinal degeneration (judged by thickness of outer nuclear layer),

387   polycystic kidney, and male infertility (Figure 8E-H). The absence of retinal degeneration, one of

388   the most penetrant phenotypes besides obesity in Bardet-Biedl syndrome (Forsythe & Beales,

389   2013) (Forsyth & Gunay-Aygun, 2020), might reflect the lack of Ncs1 at the ciliary base in

390   photoreceptors (Figure 7-figure supplement 2E). The milder phenotype of $Ncs1^{-/-}$ mice than the

391   previously reported cilia-defective mice may reflect mild-modest cilium formation defect of

392    $Ncs1^{-/-}$ mice (Figure 7E and G). Further investigations are needed to determine whether the

393   obesity phenotype singularly come from cilia defect, and how exactly dysfunction of cilia leads

394   to obesity in $Ncs1^{-/-}$ mice.

395   **Discussion**

396   In 1962, Sorokin described through electron micrographs that cilium biogenesis in fibroblasts is

397   initiated by attachment of a small vesicle to the distal end of the centriole (S. Sorokin, 1962), or

398   more precisely to the distal appendage of the mother centriole (Schmidt et al., 2012). Since the

18

399   distal appendage proteins that have been discovered so far (CEP83 (Tanos et al., 2013), CEP164

400   (Graser et al., 2007), TTBK2 (Cajanek & Nigg, 2014), SCLT1 (Tanos et al., 2013), FBF1 (Tanos

401   et al., 2013), CEP89 (Sillibourne et al., 2011), ANKRD26 (Bowler et al., 2019), LRRC45

402   (Kurtulmus et al., 2018)) lack apparent lipid binding motifs, how exactly the ciliary vesicle is

403   captured by the distal appendage is poorly understood. In an accompanying paper, we screened

404   all the previously and newly discovered distal appendage proteins and found that CEP89 is

405   important for ciliary vesicle recruitment but not for other processes of cilium formation, such as

406   IFT and CEP19 recruitment (see Figure 6 of (Tomoharu Kanie et al., 2023)). Since CEP89 also

407   lacks any identifiable lipid binding domain, we hypothesized that an interactor of CEP89 would

408   be directly involved in the ciliary vesicle recruitment. In this paper, we discovered NCS1 as a

409   stoichiometric interactor of CEP89. We further show that NCS1 captures the ciliary vesicle via

410   its myristoylation motif.

411   **How NCS1 captures ciliary vesicles only at distal appendages?**

412   To make cilium formation efficient and error-free, we assume that the cells would have

413   mechanisms where NCS1 only captures the ciliary vesicle at the distal appendage but not at other

414   location of the cells (e.g. cytoplasm). In addition to its centriolar localization, NCS1 localizes

415   throughout cytoplasm, of which signal is completely lost in NCS1 knockout cells (Figure 2A).

416   This implies that NCS1 may sequester its myristoylation motif to remain in cytoplasm and may

417   expose the membrane association motif to capture the ciliary vesicle only at the distal

418   appendage. One very intriguing possibility is that NCS1 may protrude its myristoyl group in

419   response to increase in local calcium concentration (calcium-myristoyl switch), as shown in

420   other NCS family proteins, such as Recoverin and Hippocalcin (Ames et al., 1997; O'Callaghan

421   et al., 2003). The local calcium concentration may be higher at the centriole because of the high

422   calcium concentration in the cilium (Delling, DeCaen, Doerner, Febvay, & Clapham, 2013). We

423   addressed this question by making a series of EF-hand mutants of NCS1, where the amino acids

424   at the -z position required for calcium binding were mutated. Our data emphasizes the

425   importance of calcium in the stability of NCS1 (Figure 5-figure supplement 1A). As long as the

426   expression level of NCS1 is maintained, the mutation did not strongly affect either centriolar

427   localization or cilium formation (Figure 5-figure supplement 1B and C). These data suggest that

428   calcium may be required for the structural integrity of NCS1 but may not regulate protrusion of

429   myristoyl moiety, which is required for efficient ciliary vesicle recruitment and subsequent

430   cilium formation (Figure 5E and F). Our data aligns with the previous reports that suggest the

431   absence of calcium-myristoyl switch in NCS1 (Ames et al., 2000; O'Callaghan et al., 2002)

432   (Lemire et al., 2016). The second possibility is that NCS1 exposes its myristoyl group only when

433   the protein binds to another protein at the distal appendage. Given that CEP89 recruits NCS1 to

434   the distal appendage (Figure 2L), we wondered if NCS1 associates with membranes only when

435   the protein binds to CEP89. However, a fractionation experiment showed that NCS1 purifies

436   with the membrane fraction even in the absence of CEP89 (Figure 5A), indicating the absence of

437   CEP89-myristoyl switch. The third possibility is that NCS1 continuously expose its

438   myristoylation motif but remains in cytoplasm because of a weak membrane association. This

439   hypothesis is in agreement with the low affinity of myristoylated peptides for lipid with the

440   dissociation constant of 100 μM, which is barely sufficient to keep its membrane association

441   (Peitzsch & McLaughlin, 1993). Myristoylated proteins typically require additional mechanisms

442   to bind membranes (M. H. Wright, Heal, Mann, & Tate, 2010): 1) another acyl chain (e.g.,

443   palmitoylation), 2) a cluster of basic amino acids that help association with negatively charged

444   head group of the membrane, 3) an interacting partner that has affinity for membrane. Since

445 NCS1 does not appear to have another acyl chain, membrane binding of NCS1 is likely enhanced

446 by either basic amino acids or another distal appendage protein that is in close proximity to

447 NCS1 keeps the protein associated with membrane. Interestingly, a recent paper showed that

448 lysine residues at position 3, 7, and 9 may be also involved in membrane binding of NCS1

449 (Baksheeva et al., 2020). In terms of the binding partner induced membrane association, this

450 process is likely regulated by yet unknown distal appendage protein(s) and not by CEP89 as

451 membrane association of NCS1 does not require CEP89 (Figure 5A). The rise in the local

452 concentration of NCS1 as well as membrane vesicle at the centriole may also help NCS1's

453 membrane association at that location. The weak association between myristoylated NCS1 and

454 membrane could also explain why cells can capture ciliary vesicles, albeit less efficiently, even

455 in the absence of NCS1 (Figure 3C and 5F). We currently do not have an obvious candidate for a

456 distal appendage protein that may compensate the lack of NCS1, as the depletion of NCS1 in any

457 of the knockouts of the known distal appendage proteins did not further inhibit the ciliary vesicle

458 recruitment and cilium formation (Figure 4B-D). Future study will focus on identifying

459 additional protein(s) that recruit the ciliary vesicle to the centriole.

460 **How the ciliary vesicle is transported to the distal appendage.**

461 Our model suggests that the ciliary vesicle is recruited to the distal appendage in a microtubule-

462 dependent manner, whereas NCS1 can reach to the mother centriole without intact microtubules

463 (Figure 6). How is the ciliary vesicle recruited to the distal appendage? Classically, subdistal

464 appendages were considered as the site where the microtubule anchoring occurs, as the electron

465 micrograph showed that microtubule are in contact with the head of the subdistal appendage (see

466 Figure 12 of the (Vorobjev & Chentsov Yu, 1982)). The subdistal appendage localization of

467 Ninein, which was shown to be indispensable for microtubule anchoring at the centriole

468 (Delgehyr, Sillibourne, & Bornens, 2005), further supports that subdistal appendages are the

469 contact site of the microtubule. Therefore, one can hypothesize that the ciliary vesicle is

470 transported first to the subdistal appendage and then subsequently moves to the distal appendage

471 by an unknown mechanism. Interestingly, CEP89 and its interactors, NCS1 and C3ORF14, each

472 localize to positions near the subdistal appendage in addition to their distal appendage

473 localization (Figure 2D and F) (Chong et al., 2020). NCS1 may bind to ciliary vesicle at the

474 subdistal appendage and then move to the distal appendage to anchor the vesicle and promote

475 cilium formation. Possibly this process is rapid, so that any vesicle attached to the subdistal

476 appendage has never been observed in electron micrographs. However, this model conflicts with

477 the observation that subdistal appendages are dispensable for cilium formation (Mazo, Soplop,

478 Wang, Uryu, & Tsou, 2016). Alternatively, microtubules may populate a structural site around

479 the distal appendages as shown by recent dSTORM imaging (Chong et al., 2020). γ-tubulin

480 observed in vicinity of the distal appendage may nucleate those microtubules. If this is the case,

481 the ciliary vesicle may be transported directly to the distal appendage and then be captured by

482 NCS1. To address this question, it would be greatly informative if the entire ciliary vesicle

483 recruitment process could be visualized by super-resolution microscopy in live cells in a future

484 study. Another important question is whether NCS1 specifically recognizes a receptor on the

485 ciliary vesicle or NCS1 randomly captures the membrane of vesicles that arrive at the distal

486 appendage. NCS1 may recognize specific vesicles via the membrane curvature or specific lipid

487 components. Interestingly, a recent study showed that NCS1 preferentially binds to

488 phosphatidylinositol-3-phosphate (Baksheeva et al., 2020). This warrants future study.

489 **Requirement of NCS1 in cilium formation differs among cell types**

490 Cilium formation can be classified into two types (S. P. Sorokin, 1968) (Molla-Herman et al.,

491   2010): 1) the intracellular pathway, which is initiated by ciliary vesicle recruitment to the distal

492   appendage, and 2) the extracellular pathway, where the centriole first docks to plasma

493   membrane. While specific cell types have been observed to selectively use one of the two

494   pathways, the distinction between the pathways might not be so definite. For example, mouse

495   inner medullary collecting duct cells (mIMCD3), typically classified as using the extracellular

496   pathway, can use the intracellular pathway in less confluent cells (Stuck et al., 2021).

497   Nonetheless, the requirement for RAB34, a ciliary vesicle marker, in ciliogenesis is more

498   pronounced in the cells that use the intracellular pathway (Ganga et al., 2021; Oguchi, Okuyama,

499   Homma, & Fukuda, 2020; Stuck et al., 2021), indicating that ciliary vesicle recruitment is an

500   indispensable step for that pathway. Our data showed that cilium formation is modestly affected

501   by NCS1 depletion in the cell types that are known to use intracellular pathway (Molla-Herman

502   et al., 2010), such as RPE and MEFs (Figure 3A and Figure 7E). While the ciliogenesis pathway

503   is not well characterized in neurons, the presence of the ciliary pocket, a sign of the intracellular

504   pathway (Molla-Herman et al., 2010), is apparent in electron micrographs of neurons and neural

505   progenitors (Barnes, 1961; Brechbuhl, Klaey, & Broillet, 2008; Breunig et al., 2008; Dingemans,

506   1969; Han et al., 2008; Mirzadeh, Merkle, Soriano-Navarro, Garcia-Verdugo, & Alvarez-Buylla,

507   2008). Thus, we can predict that neurons would use the intracellular pathway. However,

508   inconsistently with RPE and MEFs, we did not observe a ciliary formation defect in cultured

509   hippocampal neurons isolated from E18.5 mice, suggesting that the requirement for NCS1 may

510   differ among cell types even though they use the same cilium formation pathway. Another

511   possible explanation for a failure to see cilium formation defects is that it is not easy to assess the

512   kinetics of ciliation in isolated hippocampal neurons because culture conditions are very different

513   from RPE cells. Notably, cilium formation is not induced by serum starvation in isolated

514 hippocampal neurons. In tissues *in vivo*, it was not easy to assess whether the *Ncs1⁻/⁻* mice have

515 fewer cilia than the control mice for several reasons. First, cilium structure is greatly affected by

516 sample preparation. For example, we cannot visualize cilia if we do not fix the tissues by cardiac

517 perfusion with 4% paraformaldehyde and it is difficult to achieve perfectly efficient perfusion.

518 Second, orientation of cilia is affected by the orientation of how the tissue is sectioned and it is

519 thus difficult to analyze cilia that elongate perpendicularly to the slice. Therefore, we could not

520 test whether NCS1 is required for cilium formation in cells that typically use extracellular

521 pathway. These questions warrant future studies. Importantly, we did observe a decrease in

522 ciliary localization of several membrane proteins, such as ARL13B (Figure 3-figure supplement

523 1A-C) and ADCY3 (Figure 7H) in *Ncs1⁻/⁻* cells, even when the percentage of ciliated cells was

524 comparable to the control cells. This may suggest that NCS1 might be involved in recruiting

525 membrane signaling proteins to the cilium besides its function in ciliary vesicle recruitment and

526 cilium formation. It would be interesting to test in the future study if other ciliary membrane

527 proteins are also brought to the cilium via ciliary vesicles.

528 **NCS1 may be a ciliopathy gene**

529 Given that NCS1 is involved in ciliary vesicle recruitment and subsequent cilium formation, we

530 tested if *Ncs1⁻/⁻* mice exhibit ciliopathy phenotypes. Our data showed that *Ncs1⁻/⁻* mice display a

531 modest obesity phenotype, but no other apparent ciliopathy related phenotypes, including retinal

532 degeneration. The absence of retinal degeneration may be explained by the lack of Ncs1 at the

533 ciliary base in photoreceptors. A possible explanation for the lack of other ciliopathy phenotypes

534 is the partial penetrance of these other symptoms. In human, obesity and retinal degeneration is

535 observed in most Bardet-Biedl syndrome patients (-90%), whereas other phenotypes, such as

536 hypogonadism and kidney disease are often absent (Forsyth & Gunay-Aygun, 2020). Mice

537 lacking the distal appendage protein, FBF1(Zhang et al., 2021) or ANKRD26 (Acs et al., 2015)

538 (Bera et al., 2008), or the distal appendage associate protein, CEP19 (Shalata et al., 2013),

539 display morbid obesity with few other ciliopathy-related phenotypes (e.g., preweaning lethality

540 and hydrocephalus in $Fbf1^{-/-}$ and male infertility in $Cep19^{-/-}$ mice). Interestingly, our data

541 revealed that knockouts of each of these genes show a kinetic defect in ciliation, but the cells

542 also are observed to eventually catch up for cilium formation (Figure 5A and B in (Tomoharu

543 Kanie et al., 2023) paper for ANKRD26 and FBF1) (Figure 3C of (T. Kanie et al., 2017) for

544 CEP19). This phenotype is almost identical to what was observed in CEP89 or NCS1 knockout

545 cells (Figure 3A), suggesting that mild cilium formation defect may result in obesity with few

546 other ciliopathy-related defects. Another explanation for the lack of other ciliopathy phenotypes

547 besides obesity is the background of our $Ncs1^{-/-}$ mice (C57BL6/J). It is well known that depletion

548 of the same gene could cause different severity of the phenotypes in different background of

549 mice. For example, mice lacking Bbip10, a BBSome associated protein (Loktev et al., 2008), in

550 pure C57BL6/J background show complete perinatal lethality, while approximately half of the

551 $Bbip10^{-/-}$ mice in 129/SvJ background can survive into adulthood (Loktev & Jackson, 2013).

552 Interestingly, two independent reports showed that $Ncs1^{-/-}$ exhibit partial (-50%) preweaning

553 lethality (Dickinson et al., 2016; Nakamura et al., 2011) in C57BL6/N mice. The difference in

554 the severity of the phenotypes in $Ncs1^{-/-}$ mice between previous reports and our results may be

555 explained by the difference between C57BL6/J and C57BL6/N. Genetic and phenotypic

556 differences between these two strains were extensively described in the previous paper (Simon et

557 al., 2013). Thus, NCS1 may be a ciliopathy gene and obesity caused by NCS1 depletion may be

558 attributable to ciliary defect. This warrants future genetic study. If obesity accompanied with

559 NCS1 depletion is due to a cilia defect, what kind of cilia defect exist in the $Ncs1$ defective

560   animals *in vivo*? A simple defect may be the reduced number of ciliated cells because of the

561   cilium formation defect. While we did not see an apparent decrease in the number of cilia in

562   *Ncs1*$^{-/-}$ mice in any tissues that we examined (e.g., brain, kidney, pancreatic islets, and airway

563   epithelia) (Figure 7B-D, Figure 7-figure supplement 2), more accurate characterization is needed

564   to make a conclusion. It is possible that cilium formation is abolished in developmentally and

565   spatially regulated manner, so that the defect may be only apparent in specific cell types and

566   developmental stage. Another possibility that may cause cilia-related obesity phenotype in *Ncs1*$^{-}$

567     $^{/-}$ mice is that localization of some of the ciliary membrane proteins may be abolished in *Ncs1*$^{-/-}$

568   cells as shown in the cultured hippocampal neurons (Figure 7H). Unfortunately, it is not easy to

569   assess the number and morphology of the cilia as well as signal intensity of the ciliary membrane

570   proteins *in vivo* because of the issues described above. Technical improvement in the future may

571   allow us to more accurately characterize the cilia *in vivo* and determine whether ciliary defects in

572   *Ncs1*$^{-/-}$ mice indeed cause obesity. Alternatively, it would be interesting to see if *Cep89* knockout

573   mice display the similar phenotypes as *Ncs1* knockout mice.

574   **The connection between NCS1-related neurological disorder and cilia defect.**

575   NCS1 has been shown to participate in memory formation in *C. elegans* (Gomez et al., 2001) and

576   mice (Saab et al., 2009) (Nguyen et al., 2021) (Nakamura et al., 2017; Ng et al., 2016) (de

577   Rezende et al., 2014). While the neurological phenotypes in *Ncs1*$^{-/-}$ mice are not consistent

578   across studies, possibly because of the differences in mouse background, it seems that many

579   studies agree that the overall phenotypes are mild, and the mice display defects in memory

580   formation, when tested for novel object recognition (de Rezende et al., 2014) or displaced object

581   recognition (Mun et al., 2015; Ng et al., 2020; Nguyen et al., 2021). It is intriguing to consider

582   whether the memory formation defect in *Ncs1*$^{-/-}$ mice is attributable to ciliary defects. Several

583   lines of evidence suggest that loss of cilia in brain results in memory formation defects. If IFT88,

584   an IFT component critical for formation of the cilium, is depleted in telencephalon by Emx-1

585   Cre, the mice display impaired recognition memory assessed through novel object recognition

586   test (Berbari et al., 2014). The depletion of IFT20 in dentate gyrus of the hippocampus using

587   AAV-CAMKII-Cre caused the defect in displaced object recognition test (Rhee, Kirschen, Gu,

588   & Ge, 2016). Both mice lacking ADCY3 or SSTR3, ciliary membrane proteins that are

589   prominent in neurons (Bishop et al., 2007), exhibit defect in novel object recognition (Einstein et

590   al., 2010; Wang, Phan, & Storm, 2011). The similarity between cilia-defective mice and $Ncs1^{-/-}$

591   mice may suggest that the memory formation defect in $Ncs1^{-/-}$ deficient mice may be due to

592   ciliary dysfunction. It would be interesting to test whether SSTR3 agonist, which induces long-

593   term potentiation (LTP) (Einstein et al., 2010) likely via binding to the ciliary G-protein coupled

594   receptor, SSTR3, can induce LTP in $Ncs1^{-/-}$ mice. It would be also interesting to see if Cep89

595   depletion in mice causes similar memory formation defect, since NCS1 knockouts and CEP89

596   knockouts showed almost identical cilium formation defects (Figure 3). The importance of cilia

597   in neurological deficiencies should be an area of extensive future study.

598

599   **Author Contributions**

600   Conceptualization, T. K. and P. K. J.; Methodology, T. K., R.N., K.A., and P. K. J.;

601   Investigation, T. K., R.N., K.A., and P. K. J.; Writing – Original Draft, T. K.; Writing – Review

602   & Editing, T. K., R.N., K.A., O.P., and P. K. J.; Funding Acquisition, T.K. and P. K. J.;

603   Resources, T.K. and P. K. J.; Supervision, T. K. and P. K. J.

604

605   **Acknowledgments**

621

Materials and Methods

Plasmids

pMCB306, a lenti-viral vector containing loxP-mU6-sgRNAs-puro resistance-EGFP-loxP

cassette, and P293 Cas9-Blue Fluorescent Protein (BFP) were gifts from Prof. Michael Bassik.

Lenti-virus envelope and packaging vector, pCMV-VSV-G and pCMV-dR8.2 dvpr respectively,

were gifts from Prof. Bob Weinberg (Addgene plasmid #8454 and #8455).

pOG44 (V600520) was obtained from Thermo Fisher Scientific.

629   Lentiviral vectors containing single guide RNAs (sgRNAs) were generated by ligating 50 fmol

630   oligonucleotides encoding sgRNAs into 25 ng of the pMCB306 vector digested with BstXI

631   (R0113S, NEB) and BlpI (R0585S, NEB) restriction enzymes along with 0.25 μl of T4 ligase

632   (M0202S, NEB) in 2.5 μl total reaction volume. Before ligation, 4 μM of forward and reverse

633   oligonucleotides listed in the supplementary table were annealed in 50 μl of annealing buffer

634   (100 mM potassium acetate, 30 mM HEPES (pH7.4), and 3mM magnesium acetate) at room

635   temperature following denaturation in the same buffer at 95°C for 5 minutes. The targeting

636   sequence for sgRNAs are listed in the supplementary table "Source Data 1-Primers used for

637   genomic PCR and for generating sgRNA vectors". The guide RNA targeting sequence for

638   pMCB306-sgNCS1 vector used to create cells lacking both NCS1 and each of the other distal

639   appendage proteins shown in Figure 4 is the same as the one used to make NCS1 knockout cells.

640   The knockout cells for other distal appendage proteins were described in an accompanying paper

641   (Tomoharu Kanie et al., 2023).

642   pG-LAP6/puro vector (pCDNA5/TO/FRT/EGFP-TEV cleavage site-S tag-PreScission cleavage

643   site/DEST) used for the tandem affinity purification experiment was previously described (T.

644   Kanie et al., 2017). Gateway cloning compatible lentiviral vectors, pWPXLd/LAP-N/puro/DEST

645   vector and pWPXLd/LAP-C/puro/DEST vector, were previously described (T. Kanie et al.,

646   2017). pWPXLd/LAP-N/blast/long EF/DEST was created by inserting N-terminally LAP tag

647   (EGFP-TEV cleavage site-S tag-PreScission cleavage site)/DEST/blasticidin resistance cassette

648   into a second generation lenti-viral vector, pWPXLd. pWPXLd vector was a gift from Prof.

649   Didier Trono (Addgene plasmid #12258). pWPXLd/LAP-C/blast/long EF/DEST vector was

650   created by inserting DEST/C-terminally LAP tag/blasticidin resistance cassette into the pWPXLd

651   vector. pWPXLd/FLAG-N/blast/DEST vector was created by inserting FLAG/DEST/blasticidin

652 resistance cassette into the pWPXLd vector. All the lenti-viral vectors were propagated in Stbl3

653 competent cells to reduce unwanted recombination of long terminal repeat of the vectors.

654 pCS2-N-terminal 5×MYC/DEST and pCS2-N-terminal 3×HA/DEST (used for in vitro

655 translation) were created by inserting either 5×MYC tag or 3×HA tag and destination cassette

656 into pCS2+ vector, which contains Sp6 and CMV promoter.

657 The Gateway entry vector for Homo sapiens CEP89 was created by BP recombination using a

658 Polymerase Chain Reaction (PCR) product containing attB1 and attB2 site, which was amplified

659 using pCR4-TOPO-CEP89 (MHS6278-213243472, Open Biosystems) as a template. Gateway

660 entry vectors carrying truncation mutants of CEP89 (1-343a.a. and 344-783a.a.) were created by

661 using BP recombination between pDONR221 and PCR-amplified inserts.

662 The Gateway entry vectors for Homo sapiens NCS1 (HsCD00366520) and C3ORF14

663 (HsCD00365881) were obtained from Harvard plasmid. STOP codons were added or removed

664 by using Quick change mutagenesis if necessary. The Gateway entry vectors for NCS1 mutants

665 (myristoylation defective or EF-hand mutants) were created via Quick change mutagenesis using

666 the entry vector for NCS1 described above. The quick-change mutagenesis was performed by

667 PCR with a complementary primary set (forward and reverse) that has a point mutation in the

668 middle of the primers. Following the PCR, the PCR product was treated with 20U of DpnI

669 (R0176L, NEB) for 1 hour at 37°C to eliminate the template, and was then used to transform

670 competent cells.

671 The entry vectors for the CEP350 fragment (2470-2836 a.a.) and FGFR1OP (or FOP) was

672 previously described (T. Kanie et al., 2017).

673 Flp-In system compatible N-terminally LAP-tagged CEP89 was generated by LR recombination

674 between CEP89 entry vector and pG-LAP6/puro.

30

675   Lentiviral vector containing untagged CEP89 (minimal CMV promoter) was created by LR

676   recombination between CEP89 entry vector that contains a stop codon and

677   pWPXLd/LAPC/blast/minimal CMV/DEST vector.

678   Lentiviral vectors containing untagged NCS1 (long EF promoter or short EF promoter) were

679   created by LR recombination between NCS1 (wild-type and mutants) entry vectors that contain

680   stop codons and pWPXLd/LAPC/blast/long EF/DEST or pWPXLd/LAPC/blast/short EF/DEST

681   vectors.

682   N-terminally HA tagged CEP89, C3ORF14, and FGFR1OP (or FOP) vectors used for in vitro

683   binding assay were created by LR recombination between the respective entry vectors containing

684   a stop codon and the pCS2-N-terminal 3×HA/DEST vector. pCS2-N-terminal 5×MYC tagged

685   C3ORF14, NCS1, and the CEP350 fragment (2470-2836 a.a.) vectors were created by LR

686   recombination between the respective entry vectors that contain stop codons and the pCS2-N-

687   terminal 5×MYC/DEST vector.

688

Cell line, Cell culture, Transfection, and Lentiviral expression

690   hTERT RPE-1 cells and 293T cells were grown in DMEM/F-12 (12400024, Thermo Fisher

691   Scientific) supplemented with 10% FBS (100-106, Gemini), 1× GlutaMax (35050-079, Thermo

692   Fisher Scientific), 100 U/mL Penicillin-Streptomycin (15140163, Thermo Fisher Scientific) at

693   37°C in 5% CO_2. To induce cilium formation, cells were incubated in DMEM/F-12

694   supplemented with 1×GlutaMax and 100 U/mL Penicillin-Streptomycin (serum-free media).

695   Both cell lines were authenticated via a short-tandem-repeat based test. The authentication was

696   performed by MTCRO-COBRE Cell line authentication core of the University of Oklahoma

697   Health Science Center. Mycoplasma negativity of the original cell lines (hTERT RPE-1 and

698   293T) grown in antibiotics-free media were confirmed by a PCR based test (G238, Applied

699   Biological Materials).

700   RPE-FRT9 expressing N-terminally LAP tagged CEP89 used for tandem affinity purification

701   was generated by transfecting 150 ng of the preceding vectors with 850 ng of pOG44, followed

702   by selection with 10 μg/ml puromycin. Flp-In system compatible RPE cells (RPE-FRT9) were

703   previously described (Sang et al., 2011).

704   All other stable cell lines, including CRISPR knockout cells, were generated using lentivirus.

705   Lentivirus carrying either gene of interest or sgRNAs was produced by co-transfecting 293T

706   cells with 150 ng of pCMV-VSV-G, 350 ng of pCMV-dR8.2 dvpr, and 500 ng of lenti-viral

707   transfer plasmids previously described along with 3 μl of Fugene 6 (E2692, Promega)

708   transfection reagent. Media was replaced 24 hr after transfection to omit transfection reagent,

709   and virus was harvested at 48 hr post-transfection. Virus was then filtered with a 0.45 μm PVDF

710   filter (SLHV013SL, Millipore) and mixed with 4-fold volume of fresh media containing 12.5

711   μg/ml polybrene (TR-1003-G, Millipore). Following infection for 66 hr, cells were selected with

712   either 10 μg/ml puromycin (P9620, SIGMA-Aldrich) or 10 μg/ml blasticidin (30-100-RB,

713   Corning) for at least 10 days before subsequent analysis.

714

715   **CRISPR knockout**

716   RPE cells expressing BFP-Cas9 were generated by infection with lentivirus carrying P293 Cas9-

717   BFP, followed by sorting BFP-positive cells using FACSAria (BD). RPE-BFP-Cas9 cells were

718   then infected with lentivirus carrying sgRNAs in the pMCB306 vector to generate knockout

719   cells. After selection with 10 μg/ml puromycin, cells were subjected to immunoblotting,

720   immunofluorescence, or genomic PCR combined with TIDE analysis (Brinkman, Chen,

721 Amendola, & van Steensel, 2014) to determine knockout efficiency. The exact assay used for

722 each cell line is listed in "Source Data 7-summary of CRISPR knockout cells". Cells were then

723 infected with adenovirus carrying Cre-recombinase (1045N, Vector Biolabs) at a multiplicity of

724 infection of 50 to remove the sgRNA-puromycin resistance-EGFP cassette. 10 days after

725 adenovirus infection, GFP-negative single cells were sorted using FACSAria. The single cell

726 clones were expanded, and their knockout efficiency were determined by immunofluorescence,

727 Western blot, and/or genomic. The same number of validated single clones (typically three to

728 four different clones) were mixed to create pooled single cell knockout clones to minimize the

729 phenotypic variability occurred in single cell clones. The cells lacking both NCS1 and each of

730 the other distal appendage proteins shown in Figure 4 were created by infecting the knockout

731 cells with lenti-virus carrying sgNCS1. The experiments shown in Figure 4 were performed

732 without removing loxP-mU6-sgRNAs-puro resistance-EGFP-loxP cassette.

733 Cells used in the rescue experiments shown in Figure 3B, Figure 3- figure supplement 1A-C,

734 Figure 5A-F, and Figure 5- figure supplement 1A-C were created by infecting the respective

735 knockout cells with lenti-virus carrying untagged CEP89 or NCS1 (wild-type or mutants). To

736 rescue the ciliation defect of CEP89 knockout cells, the expression level of CEP89 was carefully

737 adjusted by using minimal CMV promoter to mimic endogenous CEP89 expression, since

738 overexpression of CEP89 under the control of long EF promoter significantly inhibited cilium

739 formation (data not shown).

740

741 **Tandem affinity purification**

742 5 mL packed cell volume of RPE-FRT9 cells expressing N-terminally LAP-tagged CEP89 were

743 re-suspended with 20 mL of LAP-resuspension buffer (300 mM KCl, 50 mM HEPES-KOH [pH

744   7.4], 1 mM EGTA, 1 mM MgCl$_2$, 10% glycerol, 0.5 mM dithiothreitol (DTT), and protease

745   inhibitors [PI88266, Thermo Scientific]), lysed by gradually adding 600 μL 10% NP-40 to a

746   final concentration of 0.3%, then incubated on ice for 10 min. The lysate was first centrifuged at

747   14,000 rpm (27,000 g) at 4°C for 10 min, and the resulting supernatant was centrifuged at 43,000

748   rpm (100,000 g) for 1 hr at 4°C to further clarify the lysate. High speed supernatant was mixed

749   with 500 μL of GFP-coupled beads (Torres, Miller, & Jackson, 2009) and rotated for 1 hr at 4°C

750   to capture GFP-tagged proteins, and washed five times with 1 mL LAP200N buffer (200 mM

751   KCl, 50 mM HEPES-KOH [pH 7.4], 1 mM EGTA, 1 mM MgCl$_2$, 10% glycerol, 0.5 mM DTT,

752   protease inhibitors, and 0.05% NP40). After re-suspending the beads with 1 mL LAP200N buffer

753   lacking DTT and protease inhibitors, the GFP-tag was cleaved by adding 5 μg of TEV protease

754   and rotating tubes at 4°C overnight. All subsequent steps until the cutting of bands from protein

755   gels were performed in a laminar flow hood. TEV-eluted supernatant was added to 100 μL of S-

756   protein agarose (69704-3, EMD Millipore) to capture S-tagged protein. After washing three

757   times with LAP200N buffer lacking DTT and twice with LAP100 buffer (100 mM KCl, 50 mM

758   HEPES-KOH [pH 7.4], 1 mM EGTA, 1 mM MgCl$_2$, and 10% glycerol), purified protein

759   complexes were eluted with 50 μL of 2×Lithium Dodecyl Sulfate (LDS) buffer (212 mM Tris-

760   HCl, 282 mM Tris-base, 4% LDS, 20% glycerol, 1.02 mM EDTA, 0.13% Brilliant Blue G250,

761   0.05% phenol red buffer) containing 10% DTT and boiled at 95°C for 3 min. Samples were then

762   run on Bolt® Bis-Tris Plus Gels (NW04120BOX, Thermo Fisher Scientific) in Bolt® MES SDS

763   Running Buffer (B000202, Thermo Fisher Scientific). Gels were fixed in 100 mL of fixing

764   solution (50% methanol, 10% acetic acid in Optima™ LC/MS grade water [W6-1, Thermo

765   Fisher Scientific]) at room temperature, and stained with Colloidal Blue Staining Kit (LC6025,

766   Thermo Fisher Scientific). After the buffer was replaced with Optima™ water, the bands were

767   cut into eight pieces, followed by washing twice with 500 μL of 50% acetonitrile in Optima™

768   water. The gel slices were then reduced and alkylated followed by destaining and in-gel

769   digestion using 125 ng Trypsin/LysC (V5072, Promega) as previously described (Shevchenko,

770   Tomas, Havlis, Olsen, & Mann, 2006) with the addition of Protease Max (V2071, Promega) to

771   increase digestion efficiency. Tryptic peptides were extracted from the gel bands and dried in a

772   speed vac. Prior to LC-MS, each sample was reconstituted in 0.1% formic acid, 2% acetonitrile,

773   and water. NanoAcquity (Waters) LC instrument was set at a flow rate of either 300 nL/min or

774   450 nL/min where mobile phase A was 0.2% formic acid in water and mobile phase B was 0.2%

775   formic acid in acetonitrile. The analytical column was in-house pulled and packed using C18

776   Reprosil Pur 2.4 μM (Dr. Maisch) where the I.D. was 100 μM and the column length was 20-25

777   cm. Peptide pools were directly injected onto the analytical column in which linear gradients (4-

778   40% B) were of either 80 or 120 min eluting peptides into the mass spectrometer. Either the

779   Orbitrap Elite or Orbitrap Fusion mass spectrometers were used, where a top 15 or "fastest"

780   MS/MS data acquisition was used, respectively. MS/MS was acquired using CID with a

781   collisional energy of 32-35. In a typical analysis, RAW files were processed using Byonic

782   (Protein Metrics) using 12 ppm mass accuracy limits for precursors and 0.4 Da mass accuracy

783   limits for MS/MS spectra. MS/MS data was compared to an NCBI GenBank FASTA database

784   containing all human proteomic isoforms with the exception of the tandem affinity bait construct

785   sequence and common contaminant proteins. Spectral counts were assumed to have undergone

786   fully specific proteolysis and allowing up to two missed cleavages per peptide. All data was

787   filtered and presented at a 1% false discovery rate (Elias & Gygi, 2007).

788

789   **Silver staining**

790   5μl of samples containing LDS buffer and DTT prepared for tandem affinity purification and

791   mass spectrometry described above were mixed with 0.5 μl of 500 mM iodoacetamide

792   (0210035105, MP Biomedicals). Proteins were separated in a 4-12% Bis-Tris gel (NP0321BOX,

793   Invitrogen), followed by fixation of the gel overnight in 50% methanol at room temperature.

794   The gel was impregnate with solution C (0.8% (w/v) silver nitrate (S6506, SIGMA), 207.2mM

795   ammonium hydroxide (A6899, SIGMA) and 18.9 mM sodium hydroxide) for 15 minutes,

796   followed by rinsing with water twice. The image was then developed in solution D (0.05% citric

797   and 0.0185% formaldehyde in Milli-Q) until intensity of the bands increase to optimal level. The

798   reaction was then terminated by adding stop solution (45% methanol and 10% acetic acid).

799

800   **Immunoblot**

801   For immunoblotting, cells were lysed in NP-40 lysis buffer (50 mM Tris-HCl [pH7.5], 150 mM

802   NaCl, 0.3% NP-40 [11332473001, Roche Applied Science]) containing 10 μg/ml LPC

803   (leupeptin, Pepstatin A, and chymostatin) and 1% phosphatase inhibitor cocktail 2 (P5726,

804   SIGMA). Following clarification of the lysate by centrifugation at 15,000 rpm (21,000 g) for 10

805   min, samples were mixed with 1× LDS buffer (106 mM Tris-HCl, 141 mM Tris-base, 2% LDS,

806   10% glycerol, 0.51mM EDTA, 0.065% Brilliant Blue G250, 0.025% phenol red) containing

807   2.5% 2-mercaptoethanol (M3148, SIGMA) and incubated at 95°C for 5 min. Proteins were

808   separated in an NuPAGE™ Novex™ 4-12% Bis-Tris protein gel (WG1402BOX, Thermo Fisher

809   Scientific) in NuPAGE™ MOPS SDS running buffer (50 mM MOPS, 50 mM Tris Base, 0.1%

810   SDS, 1 mM EDTA, pH 7.7), and transferred onto an Immobilon™-FL PVDF Transfer

811   Membrane (IPFL00010, EMD Millipore) in Towbin Buffer (25 mM Tris, 192 mM glycine, pH

812   8.3). Membranes were incubated in LI-COR Odyssey Blocking Buffer (NC9232238, LI-COR)

813   for 30 min at room temperature, and then probed overnight at 4°C with the appropriate primary

814   antibody diluted in the blocking buffer. Next, the membrane was washed 3 × 5 min in TBST

815   buffer (20 mM Tris, 150 mM NaCl, 0.1% Tween 20, pH 7.5) at room temperature, and incubated

816   with the appropriate IRDye® antibodies (LI-COR) diluted in the blocking buffer for 30 min at

817   room temperature. After washing three times in TBST buffer, the membrane was scanned on an

818   Odyssey CLx Imaging System (LI-COR) and proteins were detected at wavelengths 680 and 800

819   nm. Primary antibodies used for immunoblotting are listed in the "Source Data 4-List of the

820   antiboidies_CEP89-NCS1". Secondary antibodies used for immunoblotting were IRDye®

821   800CW donkey anti-rabbit (926-32213, LI-COR) and IRDye® 680CW donkey anti-mouse (926-

822   68072, LI-COR).

823

824   **Co-immunoprecipitation**

825   Cells were plated in a 10 cm dish and grown to confluent. Cells were then lysed with NP-40 lysis

826   buffer (50 mM Tris-HCl [pH7.5], 150 mM NaCl, and 0.3% NP-40) containing 10 μg/ml LPC

827   (leupeptin, Pepstatin A, and chymostatin) and 1% phosphatase inhibitor cocktail 2 (P5726,

828   SIGMA), followed by clarification of the lysate by centrifugation at 15,000 rpm (21,000 g) for

829   10 min. The protein concentration was measured by Bradford assay as described previously (see

830   procedure B step 8 in (T. Kanie & Jackson, 2018)). For GFP co-immunoprecipitation shown in

831   Figure 1D and Figure 5- figure supplement 1A, the soluble fraction was incubated with Protein A

832   beads cross-linked with rabbit anti-GFP antibody (Torres et al., 2009) (10 μl bed volume per 3

833   mg of lysate) with end-over-end rotation for 1.5 hr at 4°C. For co-immunoprecipitation with

834   endogenous NCS1 shown in Figure 1- figure supplement 1A, the lysate was incubated with

835   mouse monoclonal anti-NCS1 antibody (sc-376206, Santa Cruz) (1 μg of antibody per 4 mg of

37

836   lysate) for 1 hour with end-over-end rotation. The samples were then mixed with protein A beads

837   (20 μl bed volume) and incubated with end-over-end rotation for 1.5 hr at 4°C. After the

838   incubation with the beads (for both GFP co-IP and NCS1 co-IP), the samples were washed five

839   times with IP wash buffer (50 mM Tris-HCl [pH 7.5], 150 mM NaCl, and 0.1% NP-40). Samples

840   were then eluted with 2 × LDS buffer containing 2.5% 2-mercaptoethanol (M3148, SIGMA).

841

842   **Subcellular fractionation**

843   Cells were plated in a 15 cm dish at the density of 1.25×10^6 cells and grown in DMEM/F-12

844   media containing 10% FBS for 90 hours. Cells were detached from the plate using 0.05%

845   trypsin/EDTA (25300-054, Gibco) and pelleted down by centrifugation at 500 g at 4°C for 5

846   minutes. After washing once with 15 ml of ice cold low osmotic buffer (25mM HEPES-NaOH

847   (pH7.5), 0.5 mM $MgCl_2$), the cell pellet was re-suspended in 10 ml of the ice cold low osmotic

848   buffer and incubated on ice for 10 minutes to let the cells swollen. The swollen cells were

849   pelleted down and were re-suspended in 0.8 ml of the ice cold low osmotic buffer, followed by

850   nitrogen cavitation at 300 psi for 30 minutes on ice. The cavitate was centrifuged at 1000 g at

851   4°C for 10 minutes. The 1000 g supernatant was then centrifuged at 15,000 g at 4°C for 10

852   minutes. The 15,000 g supernatant was then transferred to an ultracentrifugation tube (343778,

853   Beckman) and ultracentrifuged at 100,000 g (R_{max}) in a TLA100.2 fixed angle rotor (Beckman) at

854   4°C for 1 hour. The supernatant samples were prepared by mixing 25 μl of supernatant from

855   each centrifugation speed with 25 μl of 2×LDS buffer containing 5% 2-mercaptoethanol. The

856   pellet samples were prepared by re-suspending the pellet with appropriate amount of 1× LDS

857   buffer containing 2.5% 2-mercaptoethanol.

858

859   *In vitro* **binding assay**

860   *Co-In vitro* translated (co-IVT) proteins were generated with pCS2-N-terminal 5×MYC vectors

861   and pCS2-N-terminal 3×HA vectors described above using TnT® Coupled Reticulocyte Lysate

862   System under the SP6 promoter (L4600, Promega) and by following manufacturer's

863   recommendations with few modifications. Briefly, instead of in vitro translating 1μg of plasmid

864   for each reaction, 0.5μg of HA-tagged protein along with 0.5μg of corresponding MYC-tagged

865   protein was co-translated. Note that we only observed the interaction between CEP89 and NCS1

866   when the two proteins were co-translated. The interaction between all the other proteins were

867   identical between original protocol and co-IVT. For each pull-down reaction, 50 μl of co-IVT

868   protein was added along with 5 μL (bed volume) of washed HA-beads (11815016001, Roche) in

869   300 μL binding buffer (25 mM HEPES-NaOH [pH 7.5], 500 mM NaCl, 1 mM CaCl2, and 0.1%

870   Triton X-100) and mixed for 2 hours at 4°C. The beads were washed five times with the same

871   buffer and eluted with 1×LDS buffer containing 2.5% 2-mercaptoethanol. The eluates were then

872   resolved by SDS-PAGE and analyzed by immunoblotting with anti-HA (901501, BioLegend)

873   and anti-MYC (ab9106, Abcam) antibodies.

874

875   **Transmission electron microscopy**

876   Either control (sgGFP) or NCS1 knockout RPE cells were grown to confluent on 12 mm round

877   coverslips (12-545-81, Fisher Scientific), followed by serum starvation for 3 hr. Cells were then

878   fixed with 4% paraformaldehyde (PFA) (433689M, Alfa Aesar) and 2% glutaraldehyde (G7526,

879   SIGMA) in sodium cacodylate buffer (100 mM sodium cacodylate and 2 mM $CaCl_2$, pH 7.4) for

880   1 hr at room temperature, followed by two washes with sodium cacodylate buffer. Cells were

881   then post fixed in cold/aqueous 1% osmium tetroxide (19100, Electron Microscopy Sciences) in

882   Milli-Q water for 1 hour at 4°C, allowed to warm to room temperature (RT) for 2 hours rotating

883   in a hood, and washed three times with Milli-Q water. The samples were then stained with 1%

884   uranyl acetate in Milli-Q water at room temperature overnight. Next, the samples were

885   dehydrated in graded ethanol (50%, 70%, 95%, and 100%), followed by infiltration in EMbed

886   812. Ultrathin serial sections (80 nm) were created using an UC7 (Leica, Wetzlar, Germany), and

887   were picked up on formvar/Carbon coated 100 mesh Cu grids, stained for 40 seconds in 3.5%

888   Uranyl Acetate in 50% Acetone followed by staining in Sato's Lead Citrate for 2 minutes.

889   Electron micrographs were taken on JEOL JEM1400 (120kV) equipped with an Orius 832

890   digital camera with 9 μm pixel (Gatan). To test the percentage of the ciliary vesicle positive

891   centriole, multiple serial sections (typically 3-4) were analyzed per each mother centriole, as

892   ciliary vesicles are often not attached to all nine blades of the distal appendage (i.e., ciliary

893   vesicles are often not found in all the sections of the same mother centriole).

894

895   **Immunofluorescence**

896   For wide-field microscopy, cells were grown on acid-washed 12 mm #1.5 round coverslips

897   (72230-10, Electron Microscopy Sciences) and fixed either in 4% paraformaldehyde (433689M,

898   Alfa Aesar) in phosphate buffered saline (PBS) for 15 min at room temperature or in 100%

899   methanol (A412-4, Fisher Scientific) for 5 min at -20°C. The primary antibodies used for

900   immunofluorescence are listed in the "Source Data 4-List of the antiboidies_CEP89-NCS1". All

901   staining condition such as fixation condition and dilution of the antibodies can be found in the

902   source data of each figure. After blocking with 5% normal serum that are matched with the

903   species used to raise secondary antibodies (005-000-121 or 017-000-121, Jackson

904   ImmunoResearch) in immunofluorescence (IF) buffer (3% bovine serum albumin (BP9703100,

905   Fisher Scientific), 0.02% sodium azide (BDH7465-2, VWR International), and 0.1% NP-40 in

906   PBS) for 30 min at room temperature, cells were incubated with primary antibody in IF buffer

907   for at least 3 hr at room temperature, followed by rinsing with IF buffer five times. The samples

908   were then incubated with fluorescent-labeled secondary antibody (listed below) in IF buffer for 1

909   hr at room temperature, followed by rinsing with IF buffer five times. After nuclear staining with

910   4',6-diamidino-2-phenylindole (DAPI) (40043, Biotium) in IF buffer at a final concentration of

911   0.5 μg/ml, coverslips were mounted with Fluoromount-G (0100-01, SouthernBiotech) onto glass

912   slides (3050002, Epredia). Images were acquired on an Everest deconvolution workstation

913   (Intelligent Imaging Innovations) equipped with a Zeiss Axio Imager Z1 microscope and a

914   CoolSnap HQ cooled CCD camera (Roper Scientific). A 40x NA1.3 Plan-Apochromat objective

915   lens (420762-9800, Zeiss) was used for ciliation assays, and a 63x NA1.4 Plan-Apochromat

916   objective lens (420780-9900, Zeiss) was used for other analyses.

917   For ciliation assays, cells were plated into a 6-well plate at a density of 2 x 10^5 cells/well and

918   grown for 66 hr. Cells were serum starved for 24 hr unless otherwise indicated and fixed in 4%

919   PFA. In the experiments presented in Figure 3A, the cells were incubated in serum free media for

920   12, 24, 48, 72, or 96 hours before fixation. After the blocking step, cells were stained with anti-

921   ARL13B (17711-1-AP, Proteintech), anti-CEP170 (41-3200, Invitrogen), and anti-acetylated

922   tubulin (Ac-Tub) antibodies (T7451, SIGMA), washed, then stained with anti-rabbit Alexa Fluor

923   488 (711-545-152, Jackson ImmunoResearch), goat anti-mouse IgG1-Alexa Fluor 568 (A-

924   21124, Invitrogen), and goat anti-mouse IgG2b Alexa Fluor 647 (A-21242, Invitrogen). All the

925   images were captured by focusing CEP170 without looking at a channel of the ciliary proteins to

926   avoid selecting specific area based on the percentage of ciliated cells. The structures extending

927   from the centrosome and positive for ARL13B with the length of more than 1 μm was counted as

928   primary cilia. At least 6 images from different fields per sample were captured for typical

929   analysis. Typically, at least 200 cells were analyzed per experiment. Exact number of cells that

930   we analyzed in each sample can be found in the Source Data of corresponding figures. The

931   percentage of ciliated cells were manually counted using the SlideBook software (Intelligent

932   Imaging Innovations).

933   For ciliary vesicle recruitment assays, cells were plated into a 6-well plate at a density of 2×10^5

934   cells/well, grown for 66 hr (without serum starvation), and fixed in 4% PFA. After the blocking

935   step, cells were stained with anti-RAB34 (27435-1-AP, Proteintech), anti-Myosin Va (sc-

936   365986, Santa Cruz), and anti-CEP170 (to mark centriole) antibodies (41-3200, Invitrogen),

937   washed, and then stained with goat anti-mouse IgG2a Alexa Fluor 488 (A-21131, Proteintech),

938   goat anti-rabbit Alexa Fluor 568 (A10042, Invitrogen), and goat anti-mouse IgG1 Alexa Fluor

939   647 (A-21240, Invitrogen). All the images were captured by focusing CEP170 without looking at

940   a channel of the ciliary vesicle markers to avoid selecting specific area based on the percentage

941   of ciliary vesicle positive centrioles. At least eight images from different fields per sample were

942   captured for typical analysis. Typically, at least 50 cells were analyzed per experiment. Exact

943   number of cells that we analyzed in each sample can be found in the Source Data of

944   corresponding figures.

945   For CP110 removal assays, cells were plated into a 6-well plate at a density of 2×10^5 cells/well

946   and grown for 66 hr. Cells were serum starved for 24 hr in 100% methanol. After the blocking

947   step, cells were stained with anti-CP110 (12780-1-AP, Proteintech), anti-FOP (H00011116-M01,

948   Abnova) (to mark both mother and daughter centrioles), and anti-CEP164 (sc-515403, Santa

949   Cruz) (to mark the mother centriole) antibodies, washed, then stained with anti-rabbit Alexa

950   Fluor 488 (711-545-152, Jackson ImmunoResearch), goat anti-mouse IgG2a-Alexa Fluor 568

951   (A-21134, Invitrogen), and goat anti-mouse IgG2b Alexa Fluor 647 (A-21242, Invitrogen). All

952   the images were captured by focusing FOP without looking at a channel of the other centriolar

953   proteins to avoid selecting specific area based on the percentage of CP110 positive centrioles.

954   CP110 localizing to both mother and daughter centrioles (as judged by colocalization with FOP)

955   were counted as two dots, and CP110 localizing only to daughter centriole (as judged by no

956   colocalization with CEP164) was counted as a one dot. Exact number of cells that we analyzed

957   in each sample can be found in the Source Data of corresponding figures.

958

959   For structured illumination microscopy, cells were grown on 18 mm square coverslips with the

960   thickness of 0.17 mm (474030-9000-000, Zeiss), fixed, and stained as described above. DAPI

961   staining was not included for the structured illumination samples. Coverslips were mounted with

962   SlowFade Gold Antifade Reagent (S36936, Life Technologies). Images were acquired on a

963   DeltaVision OMX V4 system equipped with a 100×/1.40 NA UPLANSAPO100XO objective

964   lens (Olympus), and 488 nm (100 mW), 561 nm (100 mW), and 642 nm (300 mW) Coherent

965   Sapphire solid state lasers and Evolve 512 EMCCD cameras (Photometrics). Image stacks of 2

966   μm z-steps were taken in 0.125 μm increments to ensure Nyquist sampling. Images were then

967   computationally reconstructed and subjected to image registration by using SoftWoRx 6.5.1

968   software.

969   Secondary antibodies used for immunofluorescence were donkey anti-rabbit Alexa Fluor 488

970   (711-545-152, Jackson ImmunoResearch), donkey anti-Chicken IgY Alexa Fluor 488 (703-545-

971   155, Jackson ImmunoResearch), donkey anti-mouse IgG DyLight 488 (715-485-150, Jackson

972   ImmunoResearch), goat anti-mouse IgG2a Alexa Fluor 488 (A-21131, Thermo Fisher

973   Scientific), goat anti-mouse IgG$_1$ Alexa Fluor 488 (A-21121, Thermo Fisher Scientific), donkey

974   anti-rabbit IgG Alexa Fluor 568 (A10042, Thermo Fisher Scientific), goat anti-mouse IgG2a-

975   Alexa Fluor 568 (A-21134, Thermo Fisher Scientific), goat anti-mouse IgG1-Alexa568 (A-

976   21124, Thermo Fisher Scientific), goat anti-mouse IgG2b Alexa Fluor 647 (A-21242, Thermo

977   Fisher Scientific), goat anti-mouse IgG1 Alexa Fluor 647 (A-21240, Thermo Fisher Scientific),

978   donkey anti-rabbit IgG Alexa Fluor 647 (711-605-152, Jackson ImmunoResearch).

979

980   **Mice**

981   *Ncs1*$^{-/-}$ mice in a C57BL/6J background were originally generated by the lab of Olaf Pongs

982   (Hermainski, 2012) and the strategy for the gene targeting was previously described (Ng et al.,

983   2016). Briefly, the 129 strain derived R1 embryonic stem cells carrying the targeting cassette

984   was injected into C57BL/6J blastocysts. The resulting *Ncs1*$^{-/-}$ mice, which lack exon 4-7 of *Ncs1*,

985   were backcrossed to C57BL/6J over 10 generations. The backcrossed mice were re-derived and

986   maintained at the Toronto Centre for Phenogenomics until they were transferred to Stanford

987   University.

988   All mice were maintained under specific pathogen-free conditions at the Stanford animal care

989   facility. All experiments were approved by Administrative Panel on Laboratory Animal Care at

990   Stanford University (Institutional Animal Care and Use Committee protocol number: 28556).

991   The primers used for genotyping PCR are mNCS1_genotyping-F: 5´-

992   GTCCACCCATACCAATCACT -3´, mNCS1_genotyping_WT-R: 5´-

993   ACAGAGAATCCAAAGCCAGC-3´, mNCS1_genotyping_KO-R: 5´-

994   TTGTGCTGGAGAAGGGAGAG-3´. The bands observed by PCR amplifications are 398 bp

995   and 514 bp for wild-type and knockout mice respectively.

996   The term "littermate controls" used in this paper means that the mice were born from the same

997   mother on the same day and were housed in the same cage as the test animals throughout the life.

998

999   <u>Assessment of viability of *Ncs1*^{-/-} mice</u>

1000   To test viability of *Ncs1*^{-/-} mice, *Ncs1*^{+/-} female and male mice were mated, and genotype of the

1001   offspring was examined by genomic PCR using the genotyping PCR primers described above at

1002   P21.

1003

1004   <u>Body weight measurement</u>

1005   The body weight of male or female *Ncs1*^{-/-} mice and their littermate controls were measured

1006   weekly between 9 am-12 pm. The statistics was obtained through 2-way ANOVA with Tukey's

1007   multiple comparisons test. All the raw data can be available in Figure 8B-Source Data.

1008

1009   <u>Measurement of fat weight</u>

1010   20 week old *Ncs1*^{-/-} and their litter mate *Ncs1*^{+/-} mice were anesthetized with isoflurane and

1011   euthanized by cervical dissociation. Inguinal or epididymal fat was then dissected out from the

1012   mice and were measured on a scale.

1013

1014   <u>Preparation, staining, and imaging of the tissue samples.</u>

1015   6- to 8-week-old *Ncs1*^{-/-} or their litter mate control animals were first anesthetized with 3%

1016   isoflurane (Fluriso, Bet-one) at a delivery rate of 1L/min. Complete anesthesia was confirmed by

1017   checking toe pinch reflex, and the animal was kept anesthetized throughout the procedure using a

1018   face mask that is connected to the anesthesia machine (VetEquip). Following exposure of the

1019   heart, an incision was made in the right atrium. Next, 27G½ gage needle (305109, BD)

1020   connected to a 20 ml syringe (302830, BD) was inserted into the left ventricle to transcardially

1021   perfuse the animal with 20 ml of PBS followed by 1.5 ml/g (-35 ml) of 4% (v/v)

1022   paraformaldehyde (PFA) (15710, Electron Microscopy Sciences). Note that the transcardial

1023   perfusion of 4% PFA is critical to preserve the sample to visualize primary cilia in tissues. The

1024   fixed tissues were dissected out and post-fixed in 20 ml of 100% methanol at -20°C for 20 hours.

1025   We found that the post fixation in methanol is critical for Ncs1 visualization in tissues likely

1026   through washing out the PFA from the tissue, since over-fixation of the samples in PFA greatly

1027   diminished the centrosomal signal of Ncs1 in monolayer cultured cells (data not shown). The

1028   post-fixed tissues were then submerged in graded concentration (10-20-30% (w/v)) of sucrose

1029   (S9378, SIGMA Aldrich) in PBS at 4°C until the tissue sunk in each solution to cryoprotect the

1030   samples. The tissues were then embedded into OCT compound (4583, Tissue-Tek). Cryosections

1031   (typically 7-10 μm thickness) were created on a Cryostat (3050S, Leica) and the sliced tissues

1032   were collected on adhesive microscope slides (16005-110, VWR). Samples were immunostained

1033   using the same procedure as the one used for wide-field microscopy experiments. The stained

1034   samples were imaged on the Marianas SDC spinning disk microscope (Intelligent Imaging

1035   Innovations) equipped with Cascade 1K camera (photometrics) and CSU22 confocal scanner

1036   unit (Yokogawa). A 63x NA1.4 Plan-Apochromat objective lens (420781-9910-000, Zeiss) was

1037   used to acquire images. Typically, image stacks of 10 -20 μm z-steps were taken in 0.5 μm

1038   increments.

1039

1040   <u>HE stains</u>

1041 20, 30, or 50 weeks old $Ncs1^{-/-}$ mice and their littermate controls were first fixed by transcardial

1042 perfusion of 4% PFA as described above and post-fixed in 4% PFA at 4°C for 72 hours. Tissues

1043 were then processed, embedded in paraffin blocks, sectioned on a microtome, and stained with

1044 Hematoxylin and eosin by standard techniques. Optimal number of tile pictures were obtained

1045 and stitched together via Keyence BZ-X710 fluorescent microscope.

1046

1047 Isolation of hippocampal neurons

1048 Hippocampus was dissected out from E18.5 mice, which were developed from $Ncs1^{+/-}$ female

1049 mouse crossed with $Ncs1^{+/-}$ male mice. The dissected hippocampus was dissociated by incubating

1050 the tissue in calcium magnesium free (CMF)-HBSS media (14175095, Gibco) supplemented

1051 with 10 mM HEPES (15630080, Gibco) containing 0.05% trypsin (15400-054, Gibco) at 37°C

1052 for 20 minutes. After washing the trypsinized tissue three times with 500 μl of CMF-HBSS

1053 containing 10 mM HEPES, the tissue was triturated with a fire polished Pasteur pipette. The

1054 dissociated cells were then plated on a 12 mm round coverslip (12-545-81, Fisher Scientific)

1055 coated with poly-D-lysine at a density of 60,000 cells per 24-well plate (930186, Thermo

1056 Scientific). The cells were grown in 500 μl of the Neurobasal Medium (21103049, Gibco)

1057 supplemented with 1×B27 (17504044, Gibco), 1×GlutaMax, 100 U/mL Penicillin-Streptomycin,

1058 and 10% horse serum (16050130, Gibco). 24 hours after plating, the media were replaced with

1059 the Neurobasal Medium media supplemented with 1×B27, 1×GlutaMax, and 100 U/mL

1060 Penicillin-Streptomycin. The genotype of the neurons was confirmed by genotyping PCR using

1061 the genotyping PCR primers described above.

1062

1063 Preparation of Mouse Embryonic Fibroblast

47

1064   Mouse embryonic fibroblasts (MEFs) were prepared from E13.5 mice embryos, which were

1065   developed from $Ncs1^{+/-}$ female mice crossed with $Ncs1^{+/-}$ male mice. After removing innards

1066   from the embryo, the remaining was minced with a razor blade (55411-050, VWR). The minced

1067   tissues were dissociated using 2 ml 0.05% trypsin/EDTA (25300-054, Gibco) for 20 minutes at

1068   37°C, followed by neutralization of trypsin by adding 4 ml of MEF media (DMEM high glucose

1069   (11995073, Gibco), 10% FBS (100-106, Gemini), 1×GlutaMax (35050-079, Thermo Fisher

1070   Scientific), and 100 U/mL Penicillin-Streptomycin (15140163, Thermo Fisher Scientific))

1071   containing 100 μg DNase I (LS002006, Worthington). Cells were then pelleted down, re-

1072   suspended in 15 ml of MEF media and plated into a T75 flask. The genotype of the MEFs were

1073   confirmed by genotyping PCR using the genotyping PCR primers described above. All

1074   experiments were performed with the cells that were passaged no more than three times.

1075

1076   <u>Immunoblotting of the tissue lysate</u>

1077   A 7-week-old $Ncs1^{-/-}$ and a 6-week-old $Ncs1^{+/+}$ mouse (not a littermate control) were anesthetized

1078   with isoflurane and euthanized by cervical dissociation. Tissues were quickly dissected out and

1079   minced with a razor blade (55411-050, VWR). The minced tissue is lysed in tissue lysis buffer

1080   (50 mM Tris-HCl [pH7.5], 150 mM NaCl, and 1% NP-40 (11332473001, Roche Applied

1081   Science)) for 15 minutes. Following clarification of the lysate at centrifugation at 15,000 rpm

1082   (21,000 g) for 15 minutes at 4°C, the concentration of the supernatant was measured by Bradford

1083   assay as previously described (see Procedure B step 8 in (T. Kanie & Jackson, 2018)). The lysate

1084   was mixed to prepare a sample containing 4 mg/ml lysate, 1×LDS buffer, and 2.5% 2-

1085   mercaptoethanol. 50 μg (for NCS1 blot) or 12 μg (for other proteins) were loaded onto

1086   NuPAGE™ Novex™ 4-12% Bis-Tris protein gels. Western blot was performed as described

1087   above and the fluorescent signal was detected on an Odyssey CLx Imaging System (LI-COR).

1088

1089   **Experimental replicates**

1090   The term "replicates" used in this paper indicate that the same cell lines were plated at different

1091   dates for each experiment. In most cases, cell lines were thawed from liquid nitrogen at different

1092   dates and immunostaining was performed at different dates among the replicates.

1093

1094   **Quantification of fluorescent intensity and statistical analysis**

1095   *Fluorescent intensity measurement*

1096   The fluorescent intensity was measured with 16-bit TIFF muti-color stack images acquired at

1097   63x magnification (NA1.4) by using Image J software. To measure the fluorescent intensity of

1098   centrosomal proteins, channels containing CEP170 and the protein of interest (POI) were

1099   individually extracted into separate images. A rolling ball background subtraction with a rolling

1100   ball radius of 5 pixels was implemented for both CEP170 and the POI to perform local

1101   background subtraction. The mask for both CEP170 and the POI was created by setting the lower

1102   threshold to the minimum level that covers only centrosome. Each mask was then combined by

1103   converting the two masks to a stack followed by z projection and then dilating the mask until the

1104   two masks are merged. After eroding the dilated masks several times, the fluorescent intensity of

1105   the POI was measured via "analyze particles" command with optimal size and circularity. The

1106   size and circularity are optimized for individual POI to detect most of the centrosome in the

1107   image without capturing non-centrosomal structure. Outliers (likely non-centrosomal structure)

1108   were then excluded from the data using the ROUT method with a false discovery rate of 1%

1109   using GraphPad Prism 9 software. Fluorescent intensity of ciliary proteins was measured

1110   similarly to centrosomal proteins but with several modifications. Mask was created for ciliary

1111   proteins by setting the lower threshold to the minimum level that covers only cilia. The size and

1112   circularity are optimized for individual POI to detect only cilia without capturing non-ciliary

1113   structure. Macros used for the intensity measurement are available from "Source Data- Macro for

1114   measuring fluorescent intensity of centrosomal proteins" and "Source Data-Macro for measuring

1115   fluorescent intensity of ciliary proteins" in an accompanying paper (Tomoharu Kanie et al.,

1116   2023).

1117   To test whether the difference in the signal intensity is statistically different between control and

1118   test samples, the intensity measured through the described method was compared between

1119   control and test samples using nested one-way ANOVA with Dunnett's multiple comparisons

1120   test or nested t-test if there are more than two replicates. In case there are less than three

1121   replicates, the statistical test was not performed in a single experiment, as the signal intensity is

1122   affected slightly by staining procedure and statistical significance is affected largely by the

1123   number of cells examined. For example, we saw statistical significance in the signal intensity

1124   with the same samples that are stained independently if we analyze large number of the cells

1125   (more than 100 cells). Instead, we confirmed the same tendency in the change of fluorescent

1126   intensity in the test samples across two replicates.

1127

1128   *Statistical analysis for ciliation, ciliary vesicle recruitment, and CP110 removal assay*

1129   For ciliation, ciliary vesicle recruitment, and CP110 removal assay, the number of ciliated cells

1130   from the indicated number of replicates were compared between control (sgGFP or sgSafe) and

50

1131   the test samples using Welch's t test. The exact number of samples and replicated are indicated

1132   in the Source Data of the corresponding figures.

1133

1134   For all the statistics used in this paper, asterisks denote *: $0.01 \leq p < 0.05$, **: $p < 0.01$, ***: $p <$

1135 0.001, n.s.: not significant. All the statical significance was calculated by using GraphPad Prism

1136   9 software.

1137

1138   **Materials Availability Statement**

1139   All the newly created materials used in this paper including plasmids and stable cell lines are

1140   readily available from the corresponding authors (Tomoharu-Kanie@ouhsc.edu or

1141   pjackson@stanford.edu) upon request.

1142

1143   **Figure supplements**

1144   Figure 1-figure supplement 1. *Co-immunoprecipitation of endogenous NCS1 and the localization*

1145   *of CEP89 mutants shown in Figure 1C.*

1146   Figure 1-figure supplement 2. *A negative control for the experiment shown in Figure 1E and F.*

1147   Figure 2-figure supplement 1. *Localization of GFP tagged NCS1.*

1148   Figure 2-figure supplement 2. *Quantification data and immunoblot related to Figure 2.*

1149   Figure 2-figure supplement 3. *Localization of other distal appendage proteins in NCS1*

1150   *knockouts.*

1151   Figure 3-figure supplement 1. *Quantification of ciliary signal intensity of ARL13B in CEP89 and*

1152   *NCS1 knockouts.*

1153   Figure 5-figure supplement 1. *Calcium is required mainly for the stability of NCS1.*

51

1154 Figure 7-figure supplement 1. *The expression of NCS1 in various tissues*.

1155 Figure 7-figure supplement 2. *NCS1 localizes to the ciliary base in most ciliated tissues but not*

1156 *in photoreceptor cells*.

1157 Figure 7-figure supplement 3. *Localization of ciliary GPCRs is mildly decreased in hippocampal*

1158 *neurons prepared from Ncs1$^{-/-}$ mice*.

1159

1160 **Source Data**

1161 Figure 1A- Source Data. Uncropped image of silver staining of the tandem affinity purification

1162 analysis of CEP89.

1163 Figure 1B-Source Data. Mass spectrometry analysis of tandem affinity purification of CEP89.

1164 Figure 1D-Source Data. The original files of the full raw unedited blots shown in Figure 1D.

1165 Figure 1E-Source Data. The original files of the full raw unedited blots shown in Figure 1D.

1166 Figure 1F-Source Data. The original files of the full raw unedited blots shown in Figure 1E.

1167 Figure 2A-Source Data. Immunofluorescence conditions in the experiment shown in Figure 2A.

1168 Figure 2B-Source Data. Immunofluorescence conditions in the experiment shown in Figure 2B.

1169 Figure 2C-Source Data. Immunofluorescence conditions, raw image quantification data, and

1170 detailed statistics of the experiment shown in Figure 2C.

1171 Figure 2D-I-Source Data. Immunofluorescence conditions in the experiment shown in Figure

1172 2D-I.

1173 Figure 2K-Source Data. Immunofluorescence conditions in the experiment shown in Figure 2K.

1174 Figure 2L-Source Data. Immunofluorescence conditions in the experiment shown in Figure 2L.

1175 Figure 2M-Source Data. Immunofluorescence conditions in the experiment shown in Figure 2M.

1176 Figure 3A-Source Data. Raw quantification data, immunofluorescence conditions and detailed

1177 statistics of the experiment shown in Figure 3A.

1178 Figure 3B-Source Data. Raw quantification data, immunofluorescence conditions and detailed

1179 statistics of the experiment shown in Figure 3B.

1180 Figure 3C-Source Data. Raw quantification data, immunofluorescence conditions and detailed

1181 statistics of the experiment shown in Figure 3C.

1182 Figure 3E-Source Data. Raw quantification data and detailed statistics of the experiment shown

1183 in Figure 3E.

1184 Figure 3F-Source Data. Raw quantification data, immunofluorescence conditions and detailed

1185 statistics of the experiment shown in Figure 3F.

1186 Figure 3F-Source Data. Raw quantification data, immunofluorescence conditions and detailed

1187 statistics of the experiment shown in Figure 3F.

1188 Figure 3G-Source Data. Raw quantification data, immunofluorescence conditions and detailed

1189 statistics of the experiment shown in Figure 3G.

1190 Figure 3H-Source Data. Raw quantification data, immunofluorescence conditions and detailed

1191 statistics of the experiment shown in Figure 3H.

1192 Figure 4A-Source Data. The original files of the full raw unedited blots shown in Figure 4A.

1193 Figure 4B-Source Data. Raw quantification data, immunofluorescence conditions and detailed

1194 statistics of the experiment shown in Figure 4B.

1195 Figure 4C-Source Data. Raw quantification data, immunofluorescence conditions and detailed

1196 statistics of the experiment shown in Figure 4C.

1197 Figure 4D-Source Data. Raw quantification data, immunofluorescence conditions and detailed

1198 statistics of the experiment shown in Figure 4D.

1199   Figure 5A-Source Data. The original files of the full raw unedited blots shown in Figure 5A.

1200   Figure 5B-Source Data. The original files of the full raw unedited blots shown in Figure 5B.

1201   Figure 5C-Source Data. Immunofluorescence conditions in the experiment shown in Figure 5C.

1202   Figure 5D-Source Data. Raw quantification data and immunofluorescence conditions of the

1203   experiment shown in Figure 5D.

1204   Figure 5E-Source Data. Raw quantification data, immunofluorescence conditions and detailed

1205   statistics of the experiment shown in Figure 5E.

1206   Figure 5F-Source Data. Raw quantification data, immunofluorescence conditions and detailed

1207   statistics of the experiment shown in Figure 5F.

1208   Figure 6B-Source Data. Immunofluorescence conditions in the experiment shown in Figure 6B.

1209   Figure 6C-Source Data. Raw quantification data, immunofluorescence conditions and detailed

1210   statistics of the experiment shown in Figure 6C.

1211   Figure 6D-Source Data. Raw quantification data, immunofluorescence conditions and detailed

1212   statistics of the experiment shown in Figure 6D.

1213   Figure 6E-Source Data. Raw quantification data and immunofluorescence conditions of the

1214   experiment shown in Figure 6E.

1215   Figure 6F-Source Data. Raw quantification data and immunofluorescence conditions of the

1216   experiment shown in Figure 6F.

1217   Figure 7A-Source Data. Immunofluorescence conditions in the experiment shown in Figure 7A.

1218   Figure 7B-Source Data. Immunofluorescence conditions in the experiment shown in Figure 7B.

1219   Figure 7C-Source Data. Immunofluorescence conditions in the experiment shown in Figure 7C.

1220   Figure 7D-Source Data. Immunofluorescence conditions in the experiment shown in Figure 7D.

1221   Figure 7E-Source Data. Raw quantification data, immunofluorescence conditions and detailed

1222   statistics of the experiment shown in Figure 7E.

1223   Figure 7F-Source Data. Raw quantification data, immunofluorescence conditions and detailed

1224   statistics of the experiment shown in Figure 7F.

1225   Figure 7G-Source Data. Raw quantification data, immunofluorescence conditions and detailed

1226   statistics of the experiment shown in Figure 7G.

1227   Figure 7H-Source Data. Raw quantification data, immunofluorescence conditions and detailed

1228   statistics of the experiment shown in Figure 7H.

1229   Figure 8A-Source Data. Detailed information of the mice and detailed statistics of the

1230   experiment shown in Figure 8A.

1231   Figure 8B-C-Source Data. Raw data and detailed statistics of the experiment shown in Figure

1232   8B-C.

1233   Figure 8D-Source Data. Raw data and detailed statistics of the experiment shown in Figure 8D.

1234   Figure 8E-G-H-Source Data. Information of the mice used in the experiments shown in Figure

1235   8E, G and H.

1236   Figure 8F-Source Data. Raw data and detailed statistics of the experiment shown in Figure 8F.

1237

1238   Figure 1-figure supplement 1A-Source Data. The original files of the full raw unedited blots

1239   shown in Figure 1-figure supplement 1A.

1240   Figure 1-Figure Supplement 1B-Source Data. Immunofluorescence conditions in the experiment

1241   shown in Figure 1-Figure supplement 1B.

1242   Figure 1-figure supplement 2A-Source Data. The original files of the full raw unedited blots

1243   shown in Figure 1-figure supplement 2A.

1244   Figure 2-Figure Supplement 1-Source Data. Immunofluorescence conditions in the experiment

1245   shown in Figure 2-Figure supplement 1.

1246   Figure 2-Figure Supplement 2A-Source Data. Immunofluorescence conditions and raw

1247   quantification data of the experiment shown in Figure 2-Figure supplement 2A.

1248   Figure 2-Figure Supplement 2B-Source Data. Immunofluorescence conditions and raw

1249   quantification data of the experiment shown in Figure 2-Figure supplement 2B.

1250   Figure 2-Figure Supplement 2C-Source Data. Immunofluorescence conditions and raw

1251   quantification data of the experiment shown in Figure 2-Figure supplement 2C.

1252   Figure 2-figure supplement 2D-Source Data. The original files of the full raw unedited blots

1253   shown in Figure 2-figure supplement 2D.

1254   Figure 2-figure supplement 2E-Source Data. The original files of the full raw unedited blots

1255   shown in Figure 2-figure supplement 2E.

1256   Figure 2-Figure Supplement 3A-Source Data. Immunofluorescence conditions, raw

1257   quantification data and detailed statistics of the experiment shown in Figure 2-Figure supplement

1258   3A.

1259   Figure 2-Figure Supplement 3B-Source Data. Immunofluorescence conditions, raw

1260   quantification data and detailed statistics of the experiment shown in Figure 2-Figure supplement

1261   3B.

1262   Figure 2-Figure Supplement 3C-Source Data. Immunofluorescence conditions and raw

1263   quantification data of the experiment shown in Figure 2-Figure supplement 3C.

1264   Figure 2-Figure Supplement 3D-Source Data. Immunofluorescence conditions and raw

1265   quantification data of the experiment shown in Figure 2-Figure supplement 3D.

1266   Figure 3-Figure Supplement 1-Source Data. Immunofluorescence conditions, raw quantification

1267   data and detailed statistics of the experiment shown in Figure 3-Figure supplement 1A-C.

1268   Figure 5-figure supplement 1A-Source Data. The original files of the full raw unedited blots

1269   shown in Figure 5-figure supplement 1A.

1270   Figure 5-Figure Supplement 1B-Source Data. Immunofluorescence conditions and raw

1271   quantification data of the experiment shown in Figure 5-Figure supplement 1B.

1272   Figure 5-Figure Supplement 1C-Source Data. Immunofluorescence conditions, raw

1273   quantification data and detailed statistics of the experiment shown in Figure 5-Figure supplement

1274   1C.

1275   Figure 7-figure supplement 1A-Source Data. The original files of the full raw unedited blots

1276   shown in Figure 7-figure supplement 1A.

1277   Figure 7-Figure Supplement 2-Source Data. Immunofluorescence conditions in the experiment

1278   shown in Figure 7-Figure supplement 2A-E.

1279   Figure 7-Figure Supplement 3A-Source Data. Immunofluorescence conditions, raw

1280   quantification data and detailed statistics of the experiment shown in Figure 7-Figure supplement

1281   3A.

1282   Figure 7-Figure Supplement 3B-Source Data. Immunofluorescence conditions, raw

1283   quantification data and detailed statistics of the experiment shown in Figure 7-Figure supplement

1284   3B.

1285   Source Data 1-Primers used for genomic PCR and for generating sgRNA vectors.

1286   Source Data 2- The list of mouse embryonic fibroblasts used in this paper.

1287   Source Data 3- The list of Hippocampal Neurons used in this paper.

1288   Source Data 4- The list of antibodies used in this paper.

1289   Source Data 5- The list of cell lines used in this paper.

1290   Source Data 6- uncropped images of the Immunoblot with label.

1291   Source Data 7-summary of CRISPR knockout cells.

1292

1293   **References**

1294   Acs, P., Bauer, P. O., Mayer, B., Bera, T., Macallister, R., Mezey, E., & Pastan, I. (2015). A

1295   novel form of ciliopathy underlies hyperphagia and obesity in Ankrd26 knockout mice. Brain

1296   Struct Funct, 220(3), 1511-1528. doi:10.1007/s00429-014-0741-9

1297   Ames, J. B., Hendricks, K. B., Strahl, T., Huttner, I. G., Hamasaki, N., & Thorner, J. (2000).

1298   Structure and calcium-binding properties of Frq1, a novel calcium sensor in the yeast

1299   Saccharomyces cerevisiae. Biochemistry, 39(40), 12149-12161. doi:10.1021/bi0012890

1300   Ames, J. B., Ishima, R., Tanaka, T., Gordon, J. I., Stryer, L., & Ikura, M. (1997). Molecular

1301   mechanics of calcium-myristoyl switches. Nature, 389(6647), 198-202. doi:10.1038/38310

1302   Anderson, R. G. (1972). The three-dimensional structure of the basal body from the rhesus

1303   monkey oviduct. J Cell Biol, 54(2), 246-265. doi:10.1083/jcb.54.2.246

1304   Aravind, P., Chandra, K., Reddy, P. P., Jeromin, A., Chary, K. V., & Sharma, Y. (2008).

1305   Regulatory and structural EF-hand motifs of neuronal calcium sensor-1: Mg 2+ modulates Ca 2+

1306   binding, Ca 2+ -induced conformational changes, and equilibrium unfolding transitions. J Mol

1307   Biol, 376(4), 1100-1115. doi:10.1016/j.jmb.2007.12.033

1308   Baksheeva, V. E., Nemashkalova, E. L., Firsov, A. M., Zalevsky, A. O., Vladimirov, V. I.,

1309   Tikhomirova, N. K., . . . Zernii, E. Y. (2020). Membrane Binding of Neuronal Calcium Sensor-1:

1310   Highly Specific Interaction with Phosphatidylinositol-3-Phosphate. Biomolecules, 10(2).

1311   doi:10.3390/biom10020164

1312   Barnes, B. G. (1961). Ciliated secretory cells in the pars distalis of the mouse hypophysis. J

1313   Ultrastruct Res, 5, 453-467. doi:10.1016/s0022-5320(61)80019-1

1314   Bera, T. K., Liu, X. F., Yamada, M., Gavrilova, O., Mezey, E., Tessarollo, L., . . . Pastan, I.

1315   (2008). A model for obesity and gigantism due to disruption of the Ankrd26 gene. Proc Natl

1316   Acad Sci U S A, 105(1), 270-275. doi:10.1073/pnas.0710978105

1317   Berbari, N. F., Bishop, G. A., Askwith, C. C., Lewis, J. S., & Mykytyn, K. (2007). Hippocampal

1318   neurons possess primary cilia in culture. J Neurosci Res, 85(5), 1095-1100.

1319   doi:10.1002/jnr.21209

1320   Berbari, N. F., Malarkey, E. B., Yazdi, S. M., McNair, A. D., Kippe, J. M., Croyle, M. J., . . .

1321   Yoder, B. K. (2014). Hippocampal and cortical primary cilia are required for aversive memory in

1322   mice. PLoS One, 9(9), e106576. doi:10.1371/journal.pone.0106576

1323   Bernatik, O., Pejskova, P., Vyslouzil, D., Hanakova, K., Zdrahal, Z., & Cajanek, L. (2020).

1324   Phosphorylation of multiple proteins involved in ciliogenesis by Tau Tubulin kinase 2. Mol Biol

1325   Cell, 31(10), 1032-1046. doi:10.1091/mbc.E19-06-0334

1326   Bishop, G. A., Berbari, N. F., Lewis, J., & Mykytyn, K. (2007). Type III adenylyl cyclase

1327   localizes to primary cilia throughout the adult mouse brain. J Comp Neurol, 505(5), 562-571.

1328   doi:10.1002/cne.21510

1329   Bornens, M. (2012). The centrosome in cells and organisms. Science, 335(6067), 422-426.

1330   doi:10.1126/science.1209037

1331   Bourne, Y., Dannenberg, J., Pollmann, V., Marchot, P., & Pongs, O. (2001).

1332   Immunocytochemical localization and crystal structure of human frequenin (neuronal calcium

1333   sensor 1). J Biol Chem, 276(15), 11949-11955. doi:10.1074/jbc.M009373200

1334   Bowler, M., Kong, D., Sun, S., Nanjundappa, R., Evans, L., Farmer, V., . . . Loncarek, J. (2019).

1335   High-resolution characterization of centriole distal appendage morphology and dynamics by

1336   correlative STORM and electron microscopy. Nat Commun, 10(1), 993. doi:10.1038/s41467-

1337   018-08216-4

1338   Brechbuhl, J., Klaey, M., & Broillet, M. C. (2008). Grueneberg ganglion cells mediate alarm

1339   pheromone detection in mice. Science, 321(5892), 1092-1095. doi:10.1126/science.1160770

1340   Breunig, J. J., Sarkisian, M. R., Arellano, J. I., Morozov, Y. M., Ayoub, A. E., Sojitra, S., . . .

1341   Town, T. (2008). Primary cilia regulate hippocampal neurogenesis by mediating sonic hedgehog

1342   signaling. Proc Natl Acad Sci U S A, 105(35), 13127-13132. doi:10.1073/pnas.0804558105

1343   Brinkman, E. K., Chen, T., Amendola, M., & van Steensel, B. (2014). Easy quantitative

1344   assessment of genome editing by sequence trace decomposition. Nucleic Acids Res, 42(22),

1345   e168. doi:10.1093/nar/gku936

1346   Burgoyne, R. D., & Weiss, J. L. (2001). The neuronal calcium sensor family of Ca2+-binding

1347   proteins. Biochem J, 353(Pt 1), 1-12. Retrieved from

1348   https://www.ncbi.nlm.nih.gov/pubmed/11115393

1349   Cajanek, L., & Nigg, E. A. (2014). Cep164 triggers ciliogenesis by recruiting Tau tubulin kinase

1350   2 to the mother centriole. Proc Natl Acad Sci U S A, 111(28), E2841-2850.

1351   doi:10.1073/pnas.1401777111

1352   Cheeseman, I. M., & Desai, A. (2005). A combined approach for the localization and tandem

1353   affinity purification of protein complexes from metazoans. Sci STKE, 2005(266), pl1.

1354   doi:10.1126/stke.2662005pl1

Chong, W. M., Wang, W. J., Lo, C. H., Chiu, T. Y., Chang, T. J., Liu, Y. P., . . . Liao, J. C. (2020). Super-resolution microscopy reveals coupling between mammalian centriole subdistal appendages and distal appendages. Elife, 9. doi:10.7554/eLife.53580

Craft, J. M., Harris, J. A., Hyman, S., Kner, P., & Lechtreck, K. F. (2015). Tubulin transport by IFT is upregulated during ciliary growth by a cilium-autonomous mechanism. J Cell Biol, 208(2), 223-237. doi:10.1083/jcb.201409036

Dason, J. S., Romero-Pozuelo, J., Atwood, H. L., & Ferrus, A. (2012). Multiple roles for frequenin/NCS-1 in synaptic function and development. Mol Neurobiol, 45(2), 388-402. doi:10.1007/s12035-012-8250-4

Dateyama, I., Sugihara, Y., Chiba, S., Ota, R., Nakagawa, R., Kobayashi, T., & Itoh, H. (2019). RABL2 positively controls localization of GPCRs in mammalian primary cilia. J Cell Sci, 132(2). doi:10.1242/jcs.224428

de Rezende, V. B., Rosa, D. V., Comim, C. M., Magno, L. A., Rodrigues, A. L., Vidigal, P., . . . Romano-Silva, M. A. (2014). NCS-1 deficiency causes anxiety and depressive-like behavior with impaired non-aversive memory in mice. Physiol Behav, 130, 91-98. doi:10.1016/j.physbeh.2014.03.005

Delgehyr, N., Sillibourne, J., & Bornens, M. (2005). Microtubule nucleation and anchoring at the centrosome are independent processes linked by ninein function. J Cell Sci, 118(Pt 8), 1565-1575. doi:10.1242/jcs.02302

Delling, M., DeCaen, P. G., Doerner, J. F., Febvay, S., & Clapham, D. E. (2013). Primary cilia are specialized calcium signalling organelles. Nature, 504(7479), 311-314. doi:10.1038/nature12833

1377   Dickinson, M. E., Flenniken, A. M., Ji, X., Teboul, L., Wong, M. D., White, J. K., . . . Murray, S.

1378   A. (2016). High-throughput discovery of novel developmental phenotypes. Nature, 537(7621),

1379   508-514. doi:10.1038/nature19356

1380   Ding, X., Fragoza, R., Singh, P., Zhang, S., Yu, H., & Schimenti, J. C. (2020). Variants in

1381   RABL2A causing male infertility and ciliopathy. Hum Mol Genet, 29(20), 3402-3411.

1382   doi:10.1093/hmg/ddaa230

1383   Dingemans, K. P. (1969). The relation between cilia and mitoses in the mouse adenohypophysis.

1384   J Cell Biol, 43(2), 361-367. doi:10.1083/jcb.43.2.361

1385   Einstein, E. B., Patterson, C. A., Hon, B. J., Regan, K. A., Reddi, J., Melnikoff, D. E., . . .

1386   Tallent, M. K. (2010). Somatostatin signaling in neuronal cilia is critical for object recognition

1387   memory. J Neurosci, 30(12), 4306-4314. doi:10.1523/JNEUROSCI.5295-09.2010

1388   Elias, J. E., & Gygi, S. P. (2007). Target-decoy search strategy for increased confidence in large-

1389   scale protein identifications by mass spectrometry. Nat Methods, 4(3), 207-214.

1390   doi:10.1038/nmeth1019

1391   Fath, M. A., Mullins, R. F., Searby, C., Nishimura, D. Y., Wei, J., Rahmouni, K., . . . Sheffield,

1392   V. C. (2005). Mkks-null mice have a phenotype resembling Bardet-Biedl syndrome. Hum Mol

1393   Genet, 14(9), 1109-1118. doi:10.1093/hmg/ddi123

1394   Forsyth, R. L., & Gunay-Aygun, M. (2020). Bardet-Biedl Syndrome

1395   Overview. 2003 Jul 14 [Updated 2020 Jul 23]. In E. D. Adam MP, Mirzaa GM, et al (Ed.),

1396   GeneReviews® [Internet]. Seattle (WA).

1397   Forsythe, E., & Beales, P. L. (2013). Bardet-Biedl syndrome. Eur J Hum Genet, 21(1), 8-13.

1398   doi:10.1038/ejhg.2012.115

1399   Ganga, A. K., Kennedy, M. C., Oguchi, M. E., Gray, S., Oliver, K. E., Knight, T. A., . . .

1400   Breslow, D. K. (2021). Rab34 GTPase mediates ciliary membrane formation in the intracellular

1401   ciliogenesis pathway. Curr Biol, 31(13), 2895-2905 e2897. doi:10.1016/j.cub.2021.04.075

1402   Gierke, P., Zhao, C., Brackmann, M., Linke, B., Heinemann, U., & Braunewell, K. H. (2004).

1403   Expression analysis of members of the neuronal calcium sensor protein family: combining

1404   bioinformatics and Western blot analysis. Biochem Biophys Res Commun, 323(1), 38-43.

1405   doi:10.1016/j.bbrc.2004.08.055

1406   Gomez, M., De Castro, E., Guarin, E., Sasakura, H., Kuhara, A., Mori, I., . . . Nef, P. (2001).

1407   Ca2+ signaling via the neuronal calcium sensor-1 regulates associative learning and memory in

1408   C. elegans. Neuron, 30(1), 241-248. doi:10.1016/s0896-6273(01)00276-8

1409   Graham, J. M. (2015). Fractionation of Subcellular Organelles. Curr Protoc Cell Biol, 69, 3 1 1-3

1410   1 22. doi:10.1002/0471143030.cb0301s69

1411   Graser, S., Stierhof, Y. D., Lavoie, S. B., Gassner, O. S., Lamla, S., Le Clech, M., & Nigg, E. A.

1412   (2007). Cep164, a novel centriole appendage protein required for primary cilium formation. J

1413   Cell Biol, 179(2), 321-330. doi:10.1083/jcb.200707181

1414   Gupta, G. D., Coyaud, E., Goncalves, J., Mojarad, B. A., Liu, Y., Wu, Q., . . . Pelletier, L.

1415   (2015). A Dynamic Protein Interaction Landscape of the Human Centrosome-Cilium Interface.

1416   Cell, 163(6), 1484-1499. doi:10.1016/j.cell.2015.10.065

1417   Han, Y. G., Spassky, N., Romaguera-Ros, M., Garcia-Verdugo, J. M., Aguilar, A., Schneider-

1418   Maunoury, S., & Alvarez-Buylla, A. (2008). Hedgehog signaling and primary cilia are required

1419   for the formation of adult neural stem cells. Nat Neurosci, 11(3), 277-284. doi:10.1038/nn2059

1420   Hermainski, J. G. (2012). Untersuchungen zur Funktion des Neuronalen Calcium Sensors 1

1421   (NCS-1) an genetisch veränderten Mauslinien (Mus musculus, Linnaeus 1758). (Dissertation).

1422   Hibbard, J. V. K., Vazquez, N., Satija, R., & Wallingford, J. B. (2021). Protein turnover

1423   dynamics suggest a diffusion-to-capture mechanism for peri-basal body recruitment and

1424   retention of intraflagellar transport proteins. Mol Biol Cell, 32(12), 1171-1180.

1425   doi:10.1091/mbc.E20-11-0717

1426   Huttlin, E. L., Bruckner, R. J., Navarrete-Perea, J., Cannon, J. R., Baltier, K., Gebreab, F., . . .

1427   Gygi, S. P. (2021). Dual proteome-scale networks reveal cell-specific remodeling of the human

1428   interactome. Cell, 184(11), 3022-3040 e3028. doi:10.1016/j.cell.2021.04.011

1429   Kanie, T., Abbott, K. L., Mooney, N. A., Plowey, E. D., Demeter, J., & Jackson, P. K. (2017).

1430   The CEP19-RABL2 GTPase Complex Binds IFT-B to Initiate Intraflagellar Transport at the

1431   Ciliary Base. Dev Cell, 42(1), 22-36 e12. doi:10.1016/j.devcel.2017.05.016

1432   Kanie, T., & Jackson, P. K. (2018). Guanine Nucleotide Exchange Assay Using Fluorescent

1433   MANT-GDP. Bio Protoc, 8(7). doi:10.21769/BioProtoc.2795

1434   Kanie, T., Love, J. F., Fisher, S. D., Gustavsson, A.-K., & Jackson, P. K. (2023). A hierarchical

1435   pathway for assembly of the distal appendages that organize primary cilia. bioRxiv,

1436   2023.2001.2006.522944. doi:10.1101/2023.01.06.522944

1437   Kurtulmus, B., Yuan, C., Schuy, J., Neuner, A., Hata, S., Kalamakis, G., . . . Pereira, G. (2018).

1438   LRRC45 contributes to early steps of axoneme extension. J Cell Sci, 131(18).

1439   doi:10.1242/jcs.223594

1440   Lemire, S., Jeromin, A., & Boisselier, E. (2016). Membrane binding of Neuronal Calcium

1441   Sensor-1 (NCS1). Colloids Surf B Biointerfaces, 139, 138-147.

1442   doi:10.1016/j.colsurfb.2015.11.065

1443   Lim, S., Strahl, T., Thorner, J., & Ames, J. B. (2011). Structure of a Ca2+-myristoyl switch

1444   protein that controls activation of a phosphatidylinositol 4-kinase in fission yeast. J Biol Chem,

1445   286(14), 12565-12577. doi:10.1074/jbc.M110.208868

1446   Lo, C. H., Lin, I. H., Yang, T. T., Huang, Y. C., Tanos, B. E., Chou, P. C., . . . Wang, W. J.

1447   (2019). Phosphorylation of CEP83 by TTBK2 is necessary for cilia initiation. J Cell Biol,

1448   218(10), 3489-3505. doi:10.1083/jcb.201811142

1449   Loktev, A. V., & Jackson, P. K. (2013). Neuropeptide Y family receptors traffic via the Bardet-

1450   Biedl syndrome pathway to signal in neuronal primary cilia. Cell Rep, 5(5), 1316-1329.

1451   doi:10.1016/j.celrep.2013.11.011

1452   Loktev, A. V., Zhang, Q., Beck, J. S., Searby, C. C., Scheetz, T. E., Bazan, J. F., . . . Nachury,

1453   M. V. (2008). A BBSome subunit links ciliogenesis, microtubule stability, and acetylation. Dev

1454   Cell, 15(6), 854-865. doi:10.1016/j.devcel.2008.11.001

1455   Lu, Q., Insinna, C., Ott, C., Stauffer, J., Pintado, P. A., Rahajeng, J., . . . Westlake, C. J. (2015).

1456   Early steps in primary cilium assembly require EHD1/EHD3-dependent ciliary vesicle

1457   formation. Nat Cell Biol, 17(3), 228-240. doi:10.1038/ncb3109

1458   Mazo, G., Soplop, N., Wang, W. J., Uryu, K., & Tsou, M. F. (2016). Spatial Control of Primary

1459   Ciliogenesis by Subdistal Appendages Alters Sensation-Associated Properties of Cilia. Dev Cell,

1460   39(4), 424-437. doi:10.1016/j.devcel.2016.10.006

1461   Mirzadeh, Z., Merkle, F. T., Soriano-Navarro, M., Garcia-Verdugo, J. M., & Alvarez-Buylla, A.

1462   (2008). Neural stem cells confer unique pinwheel architecture to the ventricular surface in

1463   neurogenic regions of the adult brain. Cell Stem Cell, 3(3), 265-278.

1464   doi:10.1016/j.stem.2008.07.004

1465   Molla-Herman, A., Ghossoub, R., Blisnick, T., Meunier, A., Serres, C., Silbermann, F., . . .

1466   Benmerah, A. (2010). The ciliary pocket: an endocytic membrane domain at the base of primary

1467   and motile cilia. J Cell Sci, 123(Pt 10), 1785-1795. doi:10.1242/jcs.059519

1468   Mun, H. S., Saab, B. J., Ng, E., McGirr, A., Lipina, T. V., Gondo, Y., . . . Roder, J. C. (2015).

1469   Self-directed exploration provides a Ncs1-dependent learning bonus. Sci Rep, 5, 17697.

1470   doi:10.1038/srep17697

1471   Mykytyn, K., Mullins, R. F., Andrews, M., Chiang, A. P., Swiderski, R. E., Yang, B., . . .

1472   Sheffield, V. C. (2004). Bardet-Biedl syndrome type 4 (BBS4)-null mice implicate Bbs4 in

1473   flagella formation but not global cilia assembly. Proc Natl Acad Sci U S A, 101(23), 8664-8669.

1474   doi:10.1073/pnas.0402354101

1475   Nakamura, T. Y., Jeromin, A., Mikoshiba, K., & Wakabayashi, S. (2011). Neuronal calcium

1476   sensor-1 promotes immature heart function and hypertrophy by enhancing Ca2+ signals. Circ

1477   Res, 109(5), 512-523. doi:10.1161/CIRCRESAHA.111.248864

1478   Nakamura, T. Y., Nakao, S., Nakajo, Y., Takahashi, J. C., Wakabayashi, S., & Yanamoto, H.

1479   (2017). Possible Signaling Pathways Mediating Neuronal Calcium Sensor-1-Dependent Spatial

1480   Learning and Memory in Mice. PLoS One, 12(1), e0170829. doi:10.1371/journal.pone.0170829

1481   Ng, E., Georgiou, J., Avila, A., Trought, K., Mun, H. S., Hodgson, M., . . . Wong, A. H. C.

1482   (2020). Mice lacking neuronal calcium sensor-1 show social and cognitive deficits. Behav Brain

1483   Res, 381, 112420. doi:10.1016/j.bbr.2019.112420

1484   Ng, E., Varaschin, R. K., Su, P., Browne, C. J., Hermainski, J., Le Foll, B., . . . Wong, A. H.

1485   (2016). Neuronal calcium sensor-1 deletion in the mouse decreases motivation and dopamine

1486   release in the nucleus accumbens. Behav Brain Res, 301, 213-225.

1487   doi:10.1016/j.bbr.2015.12.037

1488   Nguyen, L. D., Nolte, L. G., Tan, W. J. T., Giuvelis, D., Santos-Sacchi, J., Bilsky, E., & Ehrlich,

1489   B. E. (2021). Comprehensive somatosensory and neurological phenotyping of NCS1 knockout

1490   mice. Sci Rep, 11(1), 2372. doi:10.1038/s41598-021-81650-5

1491   Nishimura, D. Y., Fath, M., Mullins, R. F., Searby, C., Andrews, M., Davis, R., . . . Sheffield, V.

1492   C. (2004). Bbs2-null mice have neurosensory deficits, a defect in social dominance, and

1493   retinopathy associated with mislocalization of rhodopsin. Proc Natl Acad Sci U S A, 101(47),

1494   16588-16593. doi:10.1073/pnas.0405496101

1495   O'Callaghan, D. W., Ivings, L., Weiss, J. L., Ashby, M. C., Tepikin, A. V., & Burgoyne, R. D.

1496   (2002). Differential use of myristoyl groups on neuronal calcium sensor proteins as a

1497   determinant of spatio-temporal aspects of Ca2+ signal transduction. J Biol Chem, 277(16),

1498   14227-14237. doi:10.1074/jbc.M111750200

1499   O'Callaghan, D. W., Tepikin, A. V., & Burgoyne, R. D. (2003). Dynamics and calcium

1500   sensitivity of the Ca2+/myristoyl switch protein hippocalcin in living cells. J Cell Biol, 163(4),

1501   715-721. doi:10.1083/jcb.200306042

1502   Oguchi, M. E., Okuyama, K., Homma, Y., & Fukuda, M. (2020). A comprehensive analysis of

1503   Rab GTPases reveals a role for Rab34 in serum starvation-induced primary ciliogenesis. J Biol

1504   Chem, 295(36), 12674-12685. doi:10.1074/jbc.RA119.012233

1505   Olafsson, P., Soares, H. D., Herzog, K. H., Wang, T., Morgan, J. I., & Lu, B. (1997). The Ca2+

1506   binding protein, frequenin is a nervous system-specific protein in mouse preferentially localized

1507   in neurites. Brain Res Mol Brain Res, 44(1), 73-82. doi:10.1016/s0169-328x(96)00188-x

1508   Paintrand, M., Moudjou, M., Delacroix, H., & Bornens, M. (1992). Centrosome organization and

1509   centriole architecture: their sensitivity to divalent cations. J Struct Biol, 108(2), 107-128.

1510   doi:10.1016/1047-8477(92)90011-x

1511   Peitzsch, R. M., & McLaughlin, S. (1993). Binding of acylated peptides and fatty acids to

1512   phospholipid vesicles: pertinence to myristoylated proteins. Biochemistry, 32(39), 10436-10443.

1513   doi:10.1021/bi00090a020

1514   Pongs, O., Lindemeier, J., Zhu, X. R., Theil, T., Engelkamp, D., Krah-Jentgens, I., . . . et al.

1515   (1993). Frequenin--a novel calcium-binding protein that modulates synaptic efficacy in the

1516   Drosophila nervous system. Neuron, 11(1), 15-28. doi:10.1016/0896-6273(93)90267-u

1517   Ratai, O., Hermainski, J., Ravichandran, K., & Pongs, O. (2019). NCS-1 Deficiency Is

1518   Associated With Obesity and Diabetes Type 2 in Mice. Front Mol Neurosci, 12, 78.

1519   doi:10.3389/fnmol.2019.00078

1520   Reiter, J. F., & Leroux, M. R. (2017). Genes and molecular pathways underpinning ciliopathies.

1521   Nat Rev Mol Cell Biol, 18(9), 533-547. doi:10.1038/nrm.2017.60

1522   Rhee, S., Kirschen, G. W., Gu, Y., & Ge, S. (2016). Depletion of primary cilia from mature

1523   dentate granule cells impairs hippocampus-dependent contextual memory. Sci Rep, 6, 34370.

1524   doi:10.1038/srep34370

1525   Rigaut, G., Shevchenko, A., Rutz, B., Wilm, M., Mann, M., & Seraphin, B. (1999). A generic

1526   protein purification method for protein complex characterization and proteome exploration. Nat

1527   Biotechnol, 17(10), 1030-1032. doi:10.1038/13732

1528   Saab, B. J., Georgiou, J., Nath, A., Lee, F. J., Wang, M., Michalon, A., . . . Roder, J. C. (2009).

1529   NCS-1 in the dentate gyrus promotes exploration, synaptic plasticity, and rapid acquisition of

1530   spatial memory. Neuron, 63(5), 643-656. doi:10.1016/j.neuron.2009.08.014

1531   Sang, L., Miller, J. J., Corbit, K. C., Giles, R. H., Brauer, M. J., Otto, E. A., . . . Jackson, P. K.

1532   (2011). Mapping the NPHP-JBTS-MKS protein network reveals ciliopathy disease genes and

1533   pathways. Cell, 145(4), 513-528. doi:10.1016/j.cell.2011.04.019

1534 Schmidt, K. N., Kuhns, S., Neuner, A., Hub, B., Zentgraf, H., & Pereira, G. (2012). Cep164

1535 mediates vesicular docking to the mother centriole during early steps of ciliogenesis. J Cell Biol,

1536 199(7), 1083-1101. doi:10.1083/jcb.201202126

1537 Shalata, A., Ramirez, M. C., Desnick, R. J., Priedigkeit, N., Buettner, C., Lindtner, C., . . .

1538 Martignetti, J. A. (2013). Morbid obesity resulting from inactivation of the ciliary protein CEP19

1539 in humans and mice. Am J Hum Genet, 93(6), 1061-1071. doi:10.1016/j.ajhg.2013.10.025

1540 Shevchenko, A., Tomas, H., Havlis, J., Olsen, J. V., & Mann, M. (2006). In-gel digestion for

1541 mass spectrometric characterization of proteins and proteomes. Nat Protoc, 1(6), 2856-2860.

1542 doi:10.1038/nprot.2006.468

1543 Sillibourne, J. E., Hurbain, I., Grand-Perret, T., Goud, B., Tran, P., & Bornens, M. (2013).

1544 Primary ciliogenesis requires the distal appendage component Cep123. Biol Open, 2(6), 535-

1545 545. doi:10.1242/bio.20134457

1546 Sillibourne, J. E., Specht, C. G., Izeddin, I., Hurbain, I., Tran, P., Triller, A., . . . Bornens, M.

1547 (2011). Assessing the localization of centrosomal proteins by PALM/STORM nanoscopy.

1548 Cytoskeleton (Hoboken), 68(11), 619-627. doi:10.1002/cm.20536

1549 Simon, M. M., Greenaway, S., White, J. K., Fuchs, H., Gailus-Durner, V., Wells, S., . . . Brown,

1550 S. D. (2013). A comparative phenotypic and genomic analysis of C57BL/6J and C57BL/6N

1551 mouse strains. Genome Biol, 14(7), R82. doi:10.1186/gb-2013-14-7-r82

1552 Sorokin, S. (1962). Centrioles and the formation of rudimentary cilia by fibroblasts and smooth

1553 muscle cells. J Cell Biol, 15, 363-377. doi:10.1083/jcb.15.2.363

1554 Sorokin, S. P. (1968). Reconstructions of centriole formation and ciliogenesis in mammalian

1555 lungs. J Cell Sci, 3(2), 207-230. doi:10.1242/jcs.3.2.207

1556   Spektor, A., Tsang, W. Y., Khoo, D., & Dynlacht, B. D. (2007). Cep97 and CP110 suppress a

1557   cilia assembly program. Cell, 130(4), 678-690. doi:10.1016/j.cell.2007.06.027

1558   Stuck, M. W., Chong, W. M., Liao, J. C., & Pazour, G. J. (2021). Rab34 is necessary for early

1559   stages of intracellular ciliogenesis. Curr Biol, 31(13), 2887-2894 e2884.

1560   doi:10.1016/j.cub.2021.04.018

1561   Tanos, B. E., Yang, H. J., Soni, R., Wang, W. J., Macaluso, F. P., Asara, J. M., & Tsou, M. F.

1562   (2013). Centriole distal appendages promote membrane docking, leading to cilia initiation.

1563   Genes Dev, 27(2), 163-168. doi:10.1101/gad.207043.112

1564   Torres, J. Z., Miller, J. J., & Jackson, P. K. (2009). High-throughput generation of tagged stable

1565   cell lines for proteomic analysis. Proteomics, 9(10), 2888-2891. doi:10.1002/pmic.200800873

1566   Vorobjev, I. A., & Chentsov Yu, S. (1982). Centrioles in the cell cycle. I. Epithelial cells. J Cell

1567   Biol, 93(3), 938-949. doi:10.1083/jcb.93.3.938

1568   Wang, Z., Phan, T., & Storm, D. R. (2011). The type 3 adenylyl cyclase is required for novel

1569   object learning and extinction of contextual memory: role of cAMP signaling in primary cilia. J

1570   Neurosci, 31(15), 5557-5561. doi:10.1523/JNEUROSCI.6561-10.2011

1571   Wright, K. J., Baye, L. M., Olivier-Mason, A., Mukhopadhyay, S., Sang, L., Kwong, M., . . .

1572   Jackson, P. K. (2011). An ARL3-UNC119-RP2 GTPase cycle targets myristoylated NPHP3 to

1573   the primary cilium. Genes Dev, 25(22), 2347-2360. doi:10.1101/gad.173443.111

1574   Wright, M. H., Heal, W. P., Mann, D. J., & Tate, E. W. (2010). Protein myristoylation in health

1575   and disease. J Chem Biol, 3(1), 19-35. doi:10.1007/s12154-009-0032-8

1576   Wu, C. T., Chen, H. Y., & Tang, T. K. (2018). Myosin-Va is required for preciliary vesicle

1577   transportation to the mother centriole during ciliogenesis. Nat Cell Biol, 20(2), 175-185.

1578   doi:10.1038/s41556-017-0018-7

1579   Wu, Y., & Shroff, H. (2018). Faster, sharper, and deeper: structured illumination microscopy for

1580   biological imaging. Nat Methods, 15(12), 1011-1019. doi:10.1038/s41592-018-0211-z

1581   Zhang, Y., Hao, J., Tarrago, M. G., Warner, G. M., Giorgadze, N., Wei, Q., . . . Hu, J. (2021).

1582   FBF1 deficiency promotes beiging and healthy expansion of white adipose tissue. Cell Rep,

1583   36(5), 109481. doi:10.1016/j.celrep.2021.109481

1584

Main Figures

1585

A

B

Protein	PSMs	Unique	Coverage (%)	AAs
CEP89 (bait)	1914	223	75.99	783
NCS1	148	25	75.79	190
C3ORF14	28	9	57.81	128

C

D Co-IP assay using RPE cell lysate

E In vitro binding assay using IVT proteins

F In vitro binding assay using IVT proteins

G

Kanie et al., Figure 1
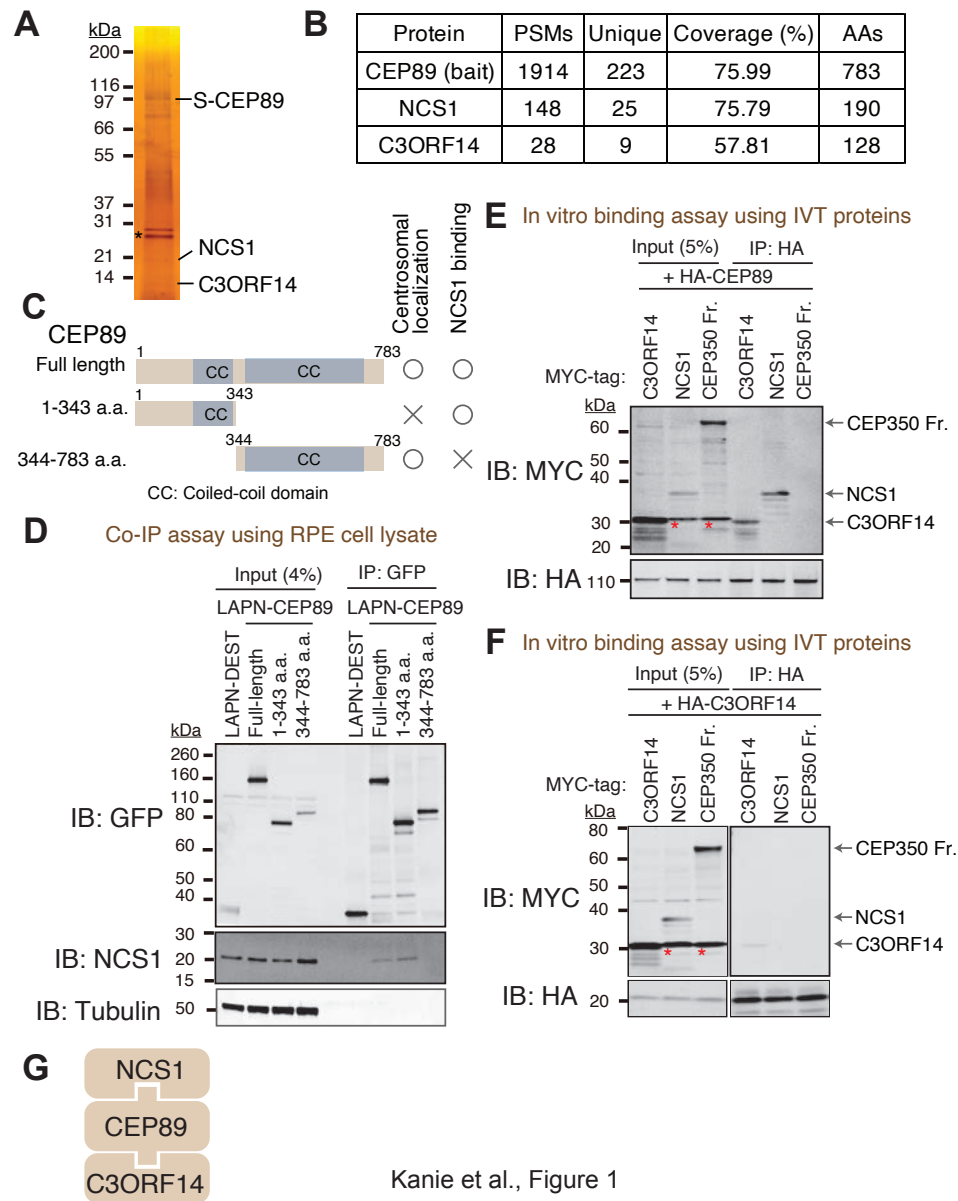
Figure 1 *Identification of Neuronal Calcium Sensor-1 as a stoichiometric interactor of CEP89.*

A. Silver staining of the eluate following tandem affinity purification of N-terminally LAP (EGFP-TEV cleavage site-S tag-PreScission cleavage site)-tagged CEP89 expressed in confluent RPE cells. The cell lysates were purified with GFP antibodies and S-protein beads, resolved by Sodium Dodecyl Sulfate–Polyacrylamide Gel Electrophoresis (SDS-PAGE) and visualized by silver staining. The bands corresponding to S tagged CEP89 (S-CEP89), NCS1, and C3ORF14 are indicated. Molecular weights (kDa) estimated from a protein marker are indicated. Asterisk denotes a band corresponding to TEV protease used for tandem affinity purification.

B. Tabulation of peptide-spectrum matches (PSMs), unique peptide counts, coverage, and the length of the amino acids from the mass spectrometry analysis of the eluate shown in (A).

C. A cartoon depicting the region of CEP89 important for centrosomal localization or binding to NCS1. Localization data can be found in Figure 1-figure supplement 1A.

D. Immunoblot (IB) analysis of the eluates from a co-immunoprecipitation assay of the full length or the indicated fragments of N-terminally LAP-tagged CEP89 expressed in confluent RPE cells. The cell lysates were purified with GFP antibodies, resolved by SDS-PAGE and immunoblotted with the indicated antibodies. Molecular weights (kDa) estimated from a protein marker are indicated.

E-F. Immunoblot (IB) analysis of the eluates from *in vitro* binding assay of the *in vitro* translated (IVT) N-terminally HA-tagged CEP89 (E) or C3ORF14 (F) and the indicated N-terminally MYC tagged proteins. The *in vitro* translated proteins were mixed and captured by HA-agarose beads, resolved by SDS-PAGE and immunoblotted with the indicated antibodies. The CEP350 fragment (2470-2836 a.a.), which binds to FOP efficiently (Figure 1-figure supplement 2A)(Kanie et al. 2017) serves as a negative control. Red asterisks indicate non-specific bands, which overlap with the MYC-tagged C3ORF14. Molecular weights (kDa) estimated from a protein marker are indicated.

G. The order of binding for CEP89-NCS1-C3ORF14 interaction.

1586

Kanie et al., Figure 2
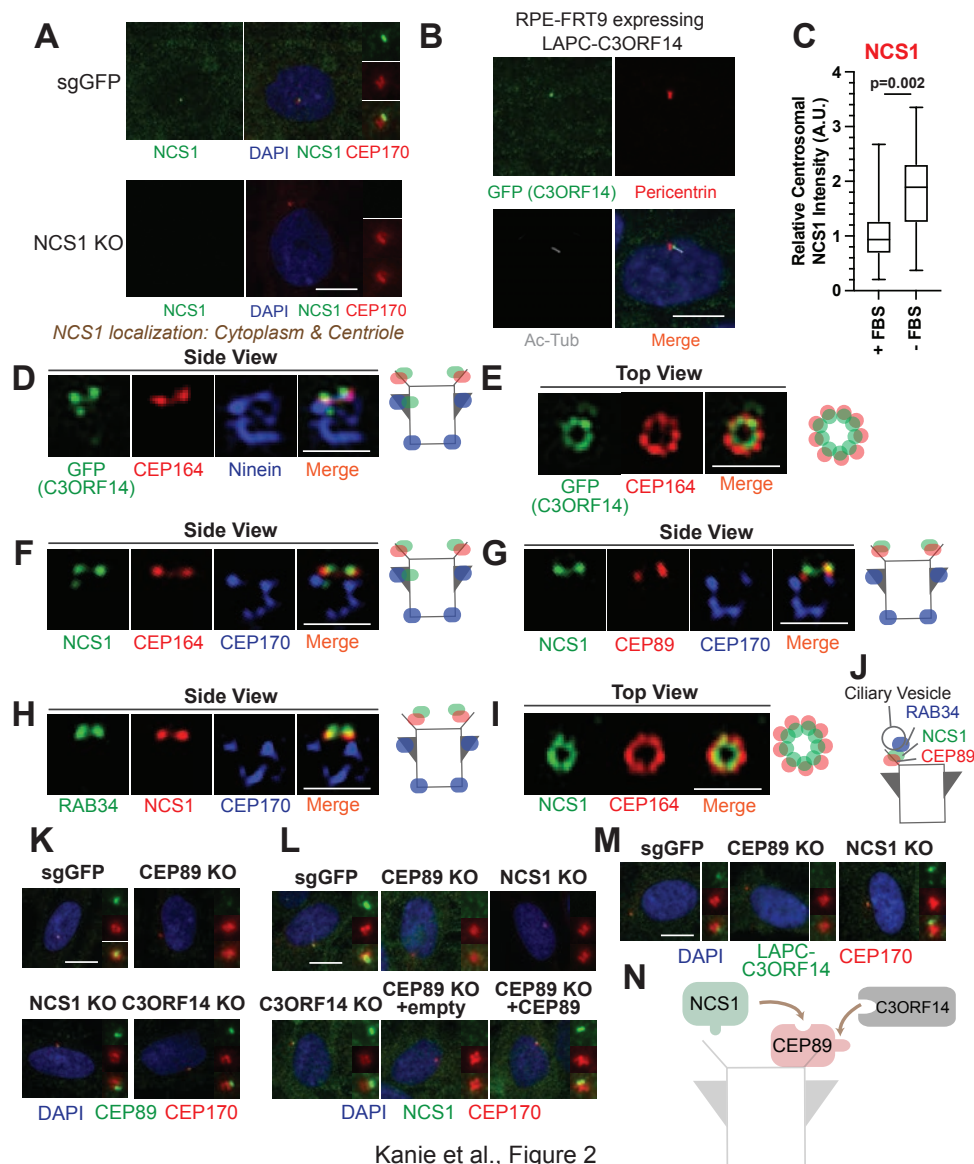
Figure 2 *NCS1 is recruited to the distal appendage by CEP89.*

A. Immunofluorescence images taken via wide-field microscopy. Control (sgGFP) or NCS1 knockout RPE cells were serum starved for 24 hours, fixed, and stained with indicated antibodies. Insets at the right panels are the enlarged images of the mother centriole. Ac-Tub indicates acetylated α-tubulin. Scale bar: 10 μm.

B. Immunofluorescence images taken via wide-field microscopy. RPE cells expressing C-terminally LAP (LAPC) tagged C3ORF14 were serum starved for 24 hours, fixed, and stained with indicated antibodies. Scale bar: 10 μm.

C. Box plots showing centrosomal signal intensity of NCS1. RPE cells were grown in fetal bovine serum (FBS)-containing media for 24 hours, and then grown in either fetal bovine serum (FBS)-containing media (+ FBS) or serum free media (-FBS) for an additional 24 hours. Cells were fixed and stained with NCS1 antibody. Centrosomal signal intensity of NCS1 was measured from fluorescence images using the method described in Materials and Methods. A.U., arbitrary units. Data are combined from three replicates. Statistical significance was calculated from a nested T-test. The raw data, experimental conditions, and detailed statistics are available in Figure 2C-Source data

D-I. Immunofluorescence images taken via 3D-structured illumination microscopy. Side view (D, F, G, and H) or Top view (E and I) is shown. RPE cells were either grown to confluent (H) or serum starved for 24 hours (D-G and I), fixed and stained with indicated antibodies. Each individual image is from a representative z-slice. Scale bar: 1 μm. CEP170: a marker of subdistal appendage and proximal end of the mother centriole. A cartoon at the right of each figure shows estimated positions of each protein at the mother centriole.

J. A cartoon depicting the localization of NCS1 relative to RAB34 and CEP89. NCS1 is sandwiched between RAB34 and CEP89.

K-M. Immunofluorescence images taken via wide-filed microscopy. Control (sgGFP) or indicated knockout RPE cells were serum starved for 24 hours, fixed, and stained with indicated antibodies. Scale bar: 10 μm. Insets at the right panels are the enlarged images of the mother centriole. Quantification data are available in Figure 2-figure supplement 2A-C.

N. A cartoon depicting the order of recruitment of the CEP89-NCS1-C3ORF14 complex.

73

1587
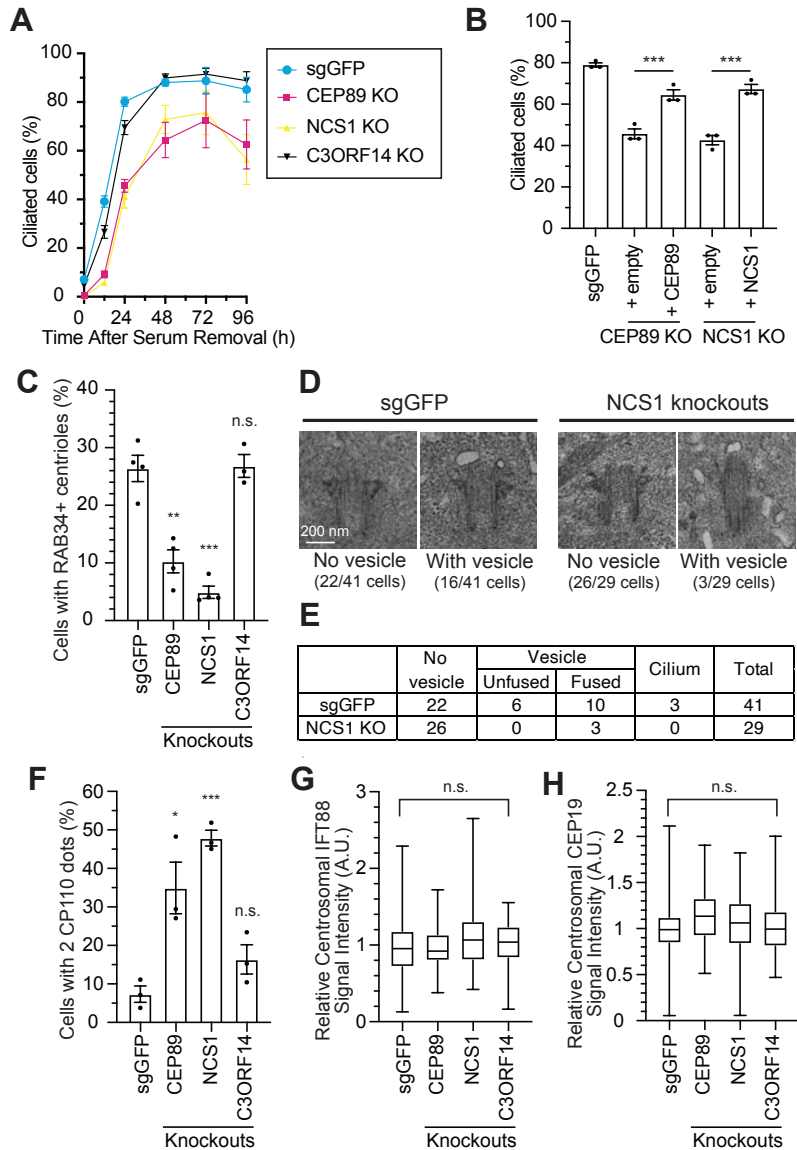
Kanie et al., Figure 3

Figure 3 *NCS1 is important for ciliary vesicle recruitment, but not for IFT88/CEP19 recruitment.*

A. Time course of cilium formation assay in control (sgGFP) and indicated knockout RPE cells. The indicated cells were serum starved for 12, 24,48,72,96 hours, fixed, stained with α-ARL13B (to mark cilium) and α-CEP170 (to mark centriole), and imaged via wide-field microscopy. Data averaged from four independent experiments. Error bars represent ± SEM. Statistics obtained through comparing between each knockout and control by Welch's t-test. The raw data, experimental conditions, detailed statistics are available in Figure 3A-Source data.

B. Cilium formation assay in control (sgGFP) and indicated knockout RPE cells serum starved for 24 hours. Data averaged from three independent experiments, and each black dot indicates the value from the individual experiment. Error bars represent ± SEM. Statistics obtained by Welch's t-test. The raw data, experimental conditions, and detailed statistics are available in Figure 3B-Source data.

 C. Ciliary vesicle recruitment assay in control (sgGFP) or indicated knockout RPE cells grown to confluence (without serum starvation). The data are averaged from 4 independent experiments, and each black dot indicates the value from each individual experiment. Error bars represent ± SEM. Statistics obtained through comparing between each knockout and control by Welch's t-test. The raw data, experimental conditions, and detailed statistics are available in Figure 3C-Source data.

D. Transmission electron microscopy analysis of the mother centriole in control (sgGFP) or NCS1 knockout RPE cells serum starved for 3 hours. The representative images of the mother centrioles without (left) or with (right) ciliary vesicle at the distal appendage are shown. Scale: 200 nm.

E. Quantification of the data from the experiments shown in Figure 3D. The raw data and detailed statistics are available in Figure 3E-Source data. This experiment was synchronized with the experiment shown in the Figure 4C of (Tomoharu Kanie et al., 2023), hence the values for sgGFP are exactly the same as the ones shown in (Tomoharu Kanie et al., 2023).

F. CP110 removal assay in control (sgGFP) and indicated knockout RPE cells serum starved for 24 hours. Data are averaged from three independent experiments, and each black dot indicates the value from the individual experiment. Error bars represent ± SEM. Statistics obtained through comparing between each knockout and control by Welch's t-test. The raw data, experimental conditions, and detailed statistics are available in Figure 3F-Source data.

G-H. Quantification of the centrosomal signal intensity of IFT88 (G) or CEP19 (H) in control (sgGFP) and indicated knockout RPE cells serum starved for 24 hours. The data are combined from three independent experiments. Statistical significance was calculated from nested T test. The raw data, experimental conditions, detailed statistics are available in Figure 3G-H-Source Data.

A.U., arbitrary units; n.s., not significant; *p < 0.05, **p < 0.01, ***p < 0.001
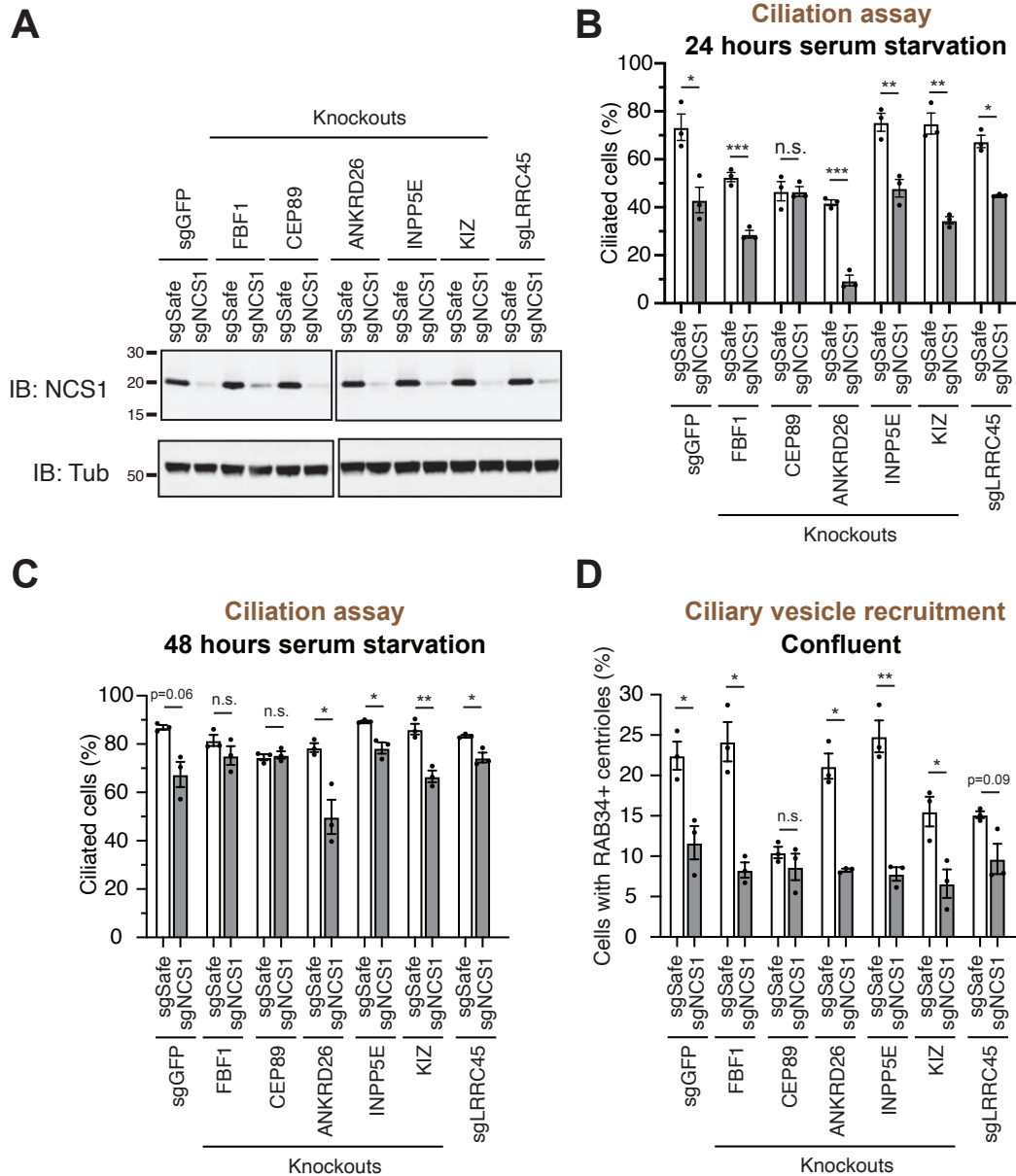
Kanie et al., Figure 4

Figure 4 A *ciliary vesicle recruitment defect in NCS1 knockout cells is compensated by yet unknown distal appendage proteins.*
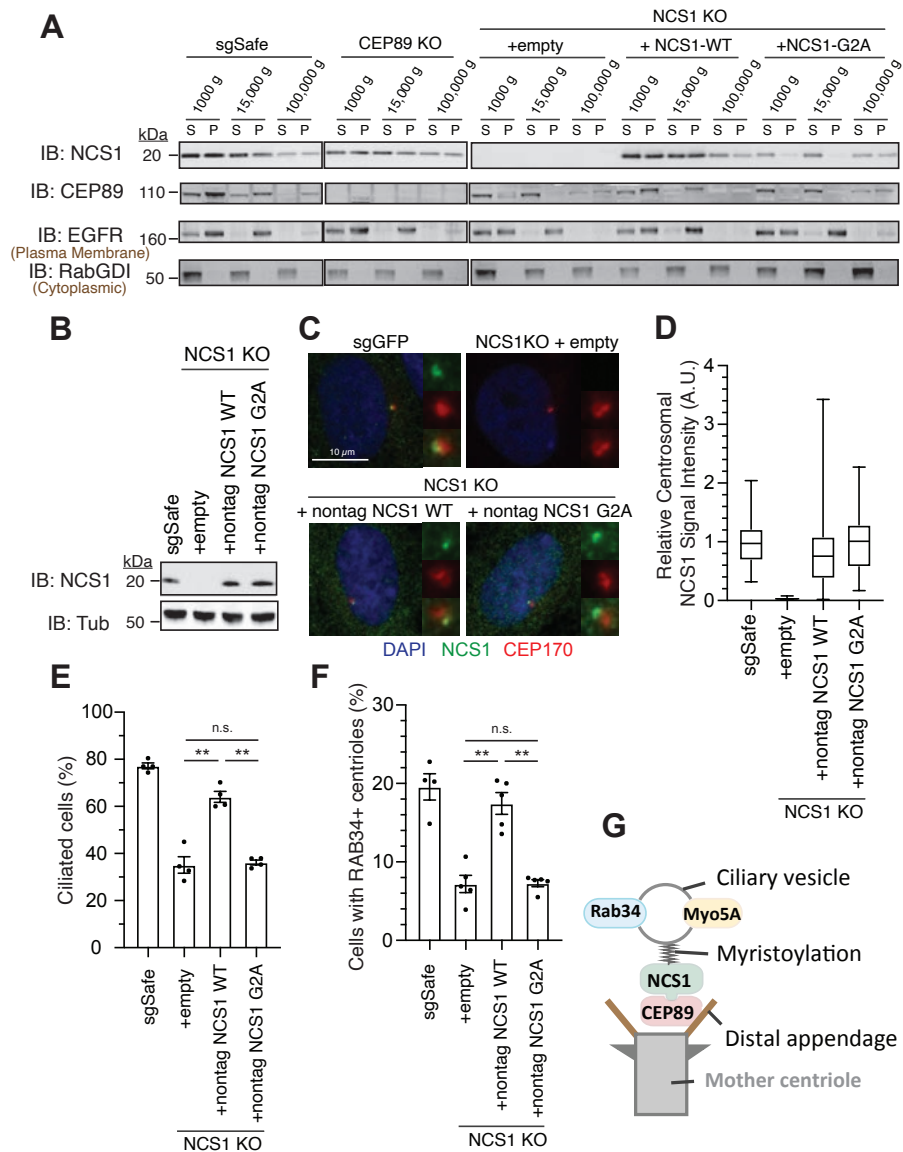
A. Immunoblot (IB) analysis of expression of NCS1 (IB: NCS1) and α-tubulin (IB: Tub) in control (sgGFP) or indicated knockout RPE cells stably expressing either sgSafe (non-targeting) or sgNCS1. The cells were grown to confluence (without serum starvation), lysed and analyzed by immunoblot. Molecular weights (kDa) estimated from a protein marker are indicated.

B-C. Cilium formation assay in control (sgGFP) and indicated knockout RPE cells stably expressing either sgSafe (non-targeting) or sgNCS1. The cells were serum starved for 24 (B) or 48 (C) hours. Data averaged from three independent experiments, and each black dot indicates the value from the individual experiment. Error bars represent ± SEM. Statistics obtained by Welch's t-test. The raw data, experimental conditions, and detailed statistics are available in Figure 4B-C-Source Data.

D. Ciliary vesicle recruitment assay in control (sgGFP) or indicated knockout RPE cells stably expressing either sgSafe (control) or sgNCS1. Cells were grown to confluence (without serum starvation). Data are averaged from three independent experiments. Error bars represent ± SEM. Statistics obtained by Welch's t-test. The raw data, experimental conditions, and detailed statistics are available in Figure 4D-Source data.

n.s., not significant; *p < 0.05, **p < 0.01, ***p < 0.001

1588

1589

Kanie et al., Figure 5

Figure 5 *NCS1 captures the ciliary vesicle via its myristoylation motif.*

A. Immunoblot (IB) analysis of expression of NCS1, CEP89, EGFR, and RabGDI. The control (sgSafe) and indicated knockout cells were grown to confluence, lysed by nitrogen cavitation, and fractionated by differential centrifugation at 1,000, 15,000, and 100,000 x g. S: supernatant; P: pellet. Molecular weights (kDa) estimated from a protein marker are indicated. EGFR and RabGDI serves as representative markers for plasma membrane or cytoplasmic proteins, respectively.

B. Immunoblot (IB) analysis of expression of NCS1 and α-tubulin in control (sgSafe) or or indicated RPE cells. Molecular weights (kDa) estimated from a protein marker are indicated.

C. Immunofluorescence images taken via wide-filed microscopy in the cells described in (B) serum starved for 24 hours. Insets at the right panels are the enlarged images of the mother centriole. Scale bar: 10 μm.

D. Box plots showing centrosomal signal intensity of NCS1 in cells described in (B) that were serum starved for 24 hours. A.U., arbitrary units. The data from a representative experiment are shown. The raw data and experimental conditions are available in Figure 5D-Source data.

E. Cilium formation assay in the cells described in (B) serum starved for 24 hours. Data averaged from four independent experiments, and each black dot indicates the value from the individual experiment. Error bars represent ± SEM. Statistics obtained by Welch's t-test. The raw data, experimental conditions, and detailed statistics are available in Figure 5E-Source data.

F. Ciliary vesicle recruitment assay in the cells described in (B) grown to confluence (without serum starvation). Data averaged from 5 independent experiments. Error bars represent ± SEM. Statistics obtained through comparing between each knockout and control by Welch's t-test. The raw data, experimental conditions, and detailed statistics are available in Figure 5F-Source data.

G. A cartoon depicting the model generated by our results. NCS1 is recruited to the distal appendage by CEP89 and captures ciliary vesicle via its myristoylation motif.

n.s., not significant; *p < 0.05, **p < 0.01, ***p < 0.001

76
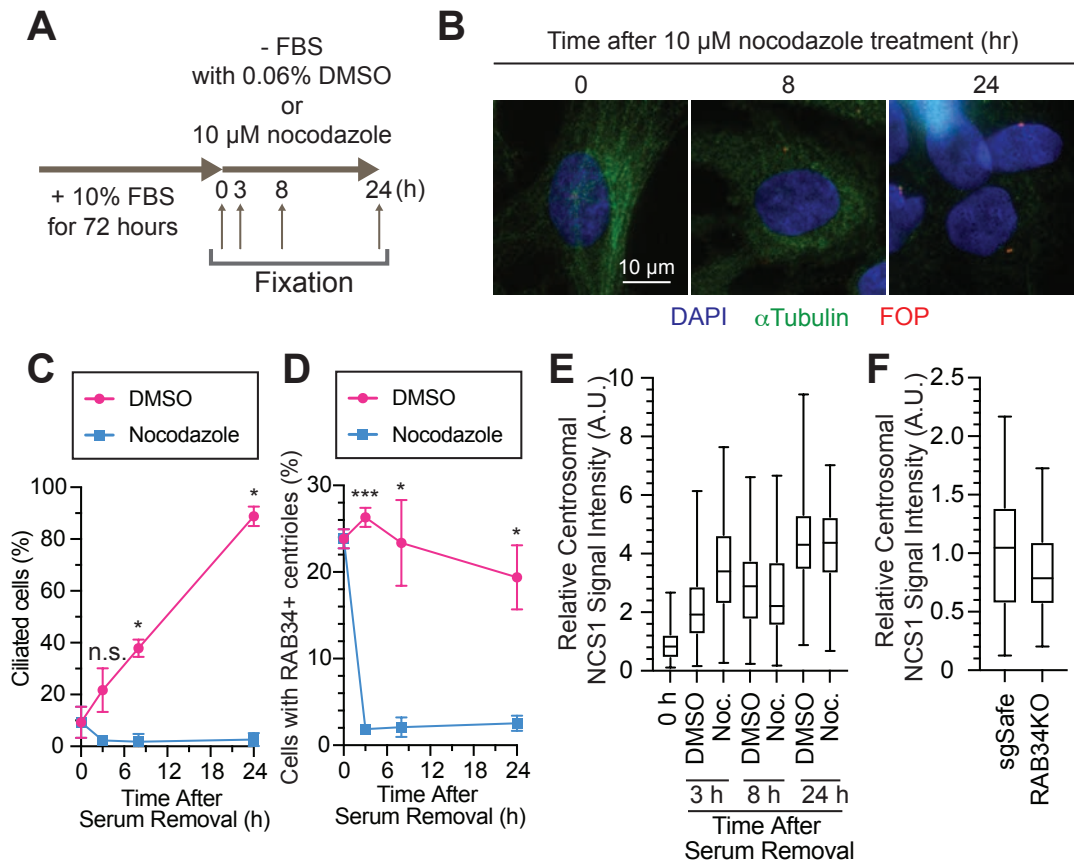
Kanie et al., Figure 6

Figure 6 *Ciliary vesicle, but not NCS1 and CEP89, is recruited to the centriole via microtubule.*

A. A cartoon showing the method used to test the requirement of microtubules in ciliary vesicle recruitment and NCS1 localization. RPE cells were cultured in media containing 10% FBS for 72 hours, then serum starved (-FBS) for indicated times in the presence of nocodazole or dimethyl sulfoxide (DMSO).

B. Immunofluorescence images taken via wide-filed microscopy. RPE cells were cultured as shown in (A), fixed, and stained with antibodies against α-Tubulin and FGFR1OP (FOP). Scale bar: 10 μm.

C. The time course of cilium formation in cells treated with either DMSO (magenta) or nocodazole (blue). The cells were fixed at indicated time points, stained with α-ARL13B (to mark cilium) and α-CEP170 (to mark centriole), and imaged via wide-field microscopy. Data averaged from three independent experiments. Error bars represent ± SEM. Statistics obtained through comparing between DMSO and nocodazole treated cells at each time point by Welch's t-test. The raw data, experimental conditions, and detailed statistics are available in Figure 6C-Source data.

D. The time course of ciliary vesicle recruitment in cells treated with either DMSO (magenta) or nocodazole (blue). The cells were fixed at indicated time points, stained with α-RAB34 (to mark ciliary vesicle) and α-CEP170 (to mark centriole), and imaged via wide-field microscopy. Data are averaged from three independent experiments. Error bars represent ± SEM. Statistics obtained through comparing between DMSO and nocodazole treated cells at each time point by Welch's t-test. The raw data, experimental conditions, and detailed statistics are available in Figure 6D-Source data.

E. Box plots showing centrosomal signal intensity of NCS1 in RPE cells prepared using the method described in (A). The data from the representative experiment are shown. The raw data and experimental conditions are available in Figure 6E-Source data.

F. Quantification of the centrosomal signal intensity of NCS1 in control or RAB34 knockout RPE cells serum starved for 24 hours. The data from the representative experiment are shown. The raw data and experimental conditions are available in Figure 6F-Source data.

A.U., arbitrary units; n.s., not significant; *p < 0.05, **p < 0.01, ***p < 0.001

1590

1591
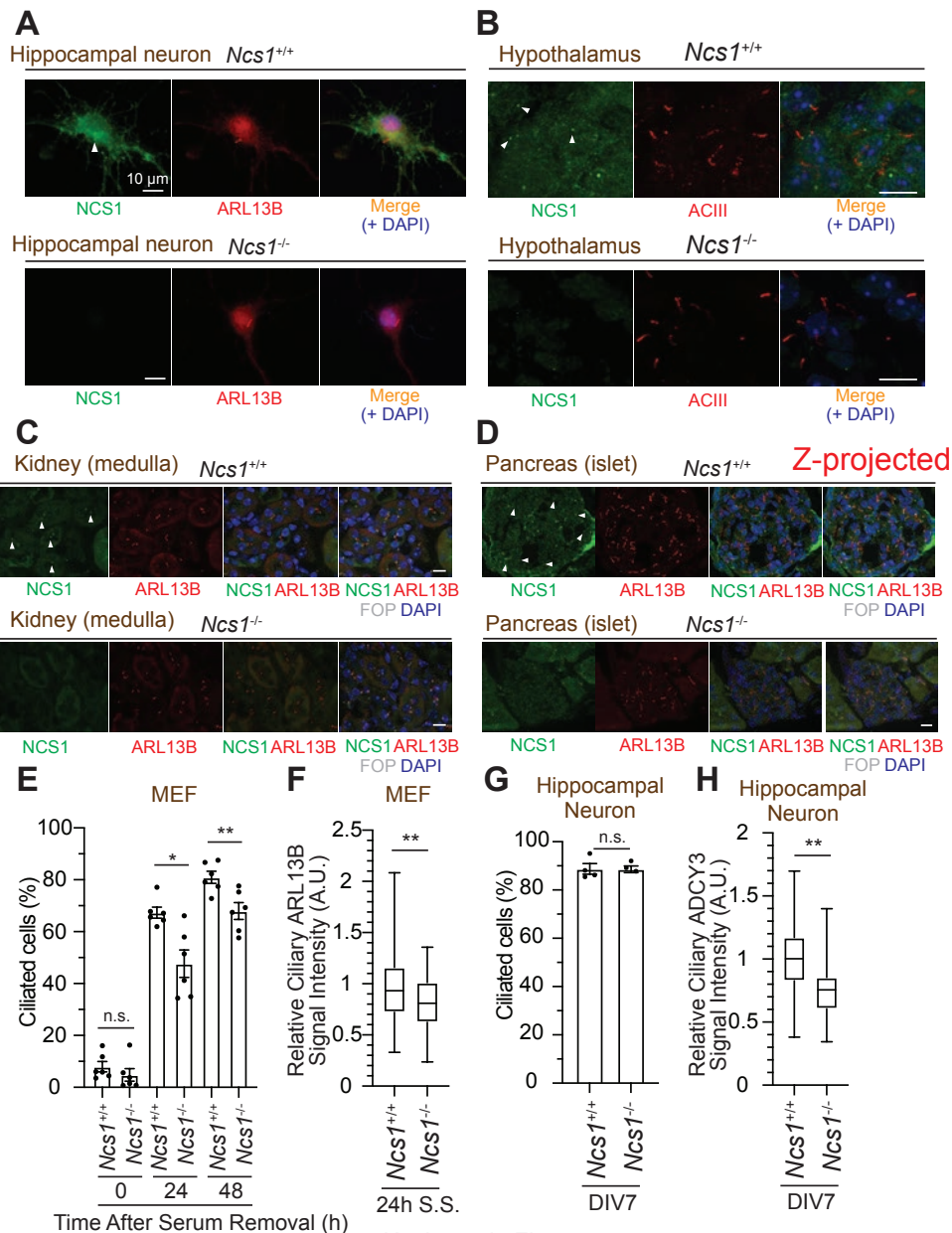
Kanie et al., Figure 7

Figure 7 *NCS1 localizes to the ciliary base in ciliated tissues and gets involved in cilium formation and ciliary membrane protein trafficking.*

A. Immunofluorescence images of cultured hippocampal neurons taken by wide-field microscopy. The isolated hippocampal neurons from E18.5 mice were fixed and stained for the indicated markers. Arrow indicates Ncs1 localization at the ciliary base. The individual image is from a representative z-slice. Scale bar: 10 μm.

B-D. Immunofluorescence images of indicated mouse tissues taken via spinning disk confocal microscopy. Tissue sections prepared from 8 week old *Ncs1*^{+/+} or *Ncs1*^{-/-} mice with the method described in Materials and Methods were stained for indicated markers. The images shown in (D) were created by maximum intensity z-projection. The other images were from representative z-slices. Arrowheads indicate NCS1 localization. Scale bar: 10 μm.

E. Cilium formation assay in *Ncs1*^{+/+} or *Ncs1*^{-/-} mouse embryonic fibroblasts (MEFs) serum starved for indicated time. Data averaged from six different MEFs per genotype. Each black dot indicates the value from the individual experiment. Error bars represent ± SEM. Statistics obtained through comparing between the two genotypes at each time point by Welch's t-test. The raw data, experimental conditions, and detailed statistics are available in Figure 7E-Source data.

F. Box plots showing ciliary signal intensity of ARL13B in *Ncs1*^{+/+} or *Ncs1*^{-/-} MEFs. The cells were serum starved for 24 hours, fixed, stained with α-ARL13B (to mark cilium) and α-CEP170 (to mark centriole), and imaged via wide-field microscopy. Data averaged from six different MEFs per genotype. Statistical significance was calculated from nested T test. The raw data, experimental conditions, and detailed statistics are available in Figure 7F-Source data.

G. Cilium formation assay in isolated hippocampal neurons prepared from *Ncs1*^{+/+} or *Ncs1*^{-/-} E18.5 mouse embryos at 7 days in vitro (DIV). Data are averaged from four different hippocampal neurons per genotype. Each black dot indicates the value from the individual experiment. Error bars represent ± SEM. Statistics obtained through comparing between the two genotypes at each time point by Welch's t-test. The raw data, experimental conditions, detailed statistics are available in Figure 7G-Source data.

H. Box plots showing ciliary signal intensity of ADCY3 in isolated hippocampal neurons prepared from *Ncs1*^{+/+} or *Ncs1*^{-/-} E18.5 mouse embryos at DIV7. The cells were fixed and stained with α-ADCY3 antibody, and imaged via wide-field microscopy. Data are averaged from five different neurons per genotype. Statistical significance was calculated from nested T test. The raw data, experimental conditions, and detailed statistics are available in Figure 7H-Source data.

A.U., arbitrary units; n.s., not significant; *p < 0.05, **p < 0.01, ***p < 0.001

1592
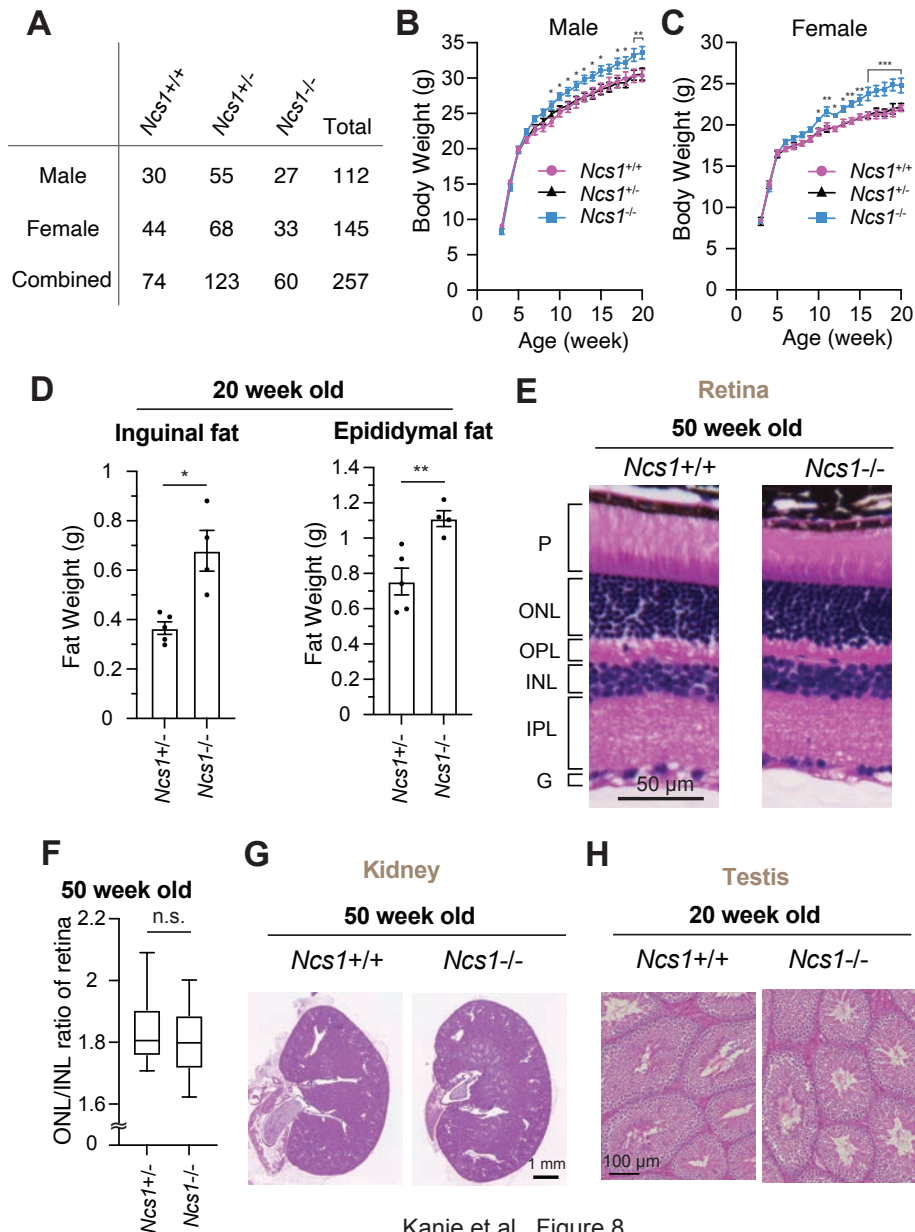
Kanie et al., Figure 8

Figure 8 *Ncs1* knockout mice display obesity but no other ciliopathy-related phenotypes.

A. A table showing viability of *Ncs1^+/+^*, *Ncs1^+/-^*, or *Ncs1^-/-^* mice, generated by crossing *Ncs1^+/-^* male and female, at P21. Detailed information of the mice and statistics are available in Figure 8A-Source Data.

B-C. Body weight analysis of *Ncs1^+/+^*, *Ncs1^+/-^*, or *Ncs1^-/-^* male (B) and female (C) mice. Raw data and detailed statistics are available from Figure 8B-C-Source Data.

D. Measurements of the weights of inguinal fat (left) or epididymal fat (right) from 20-week-old *Ncs1^+/+^* or *Ncs1^-/-^* male mice. Raw data and detailed statistics are available in Figure D-Source Data.

E. Hematoxylin and Eosin (H&E) staining of the retina prepared from 50-week-old *Ncs1^+/+^* or *Ncs1^-/-^* female mice. Scale bar: 50 μm. G, ganglion cell layer; IPL, inner plexiform layer; INL, inner nuclear layer; OPL, outer plexiform layer; ONL, outer nuclear layer; P, photoreceptor cell layer. Representative images from five *Ncs1^+/+^* or *Ncs1^-/-^* mice are shown. Detailed information of the mice is available in Figure 8E-G-H-Source Data.

F. Quantification of ONL/INL ration of the retina prepared from 50-week-old *Ncs1^+/+^* or *Ncs1^-/-^* mice. 8 areas per mouse and 5 mice from each genotype were analyzed. Statistical significance was calculated from nested T test. The raw data, detailed information of the mice, and detailed statistics are available in Figure 8F-Source Data.

G-H. H&E staining of the kidney (G) or Testis (H) prepared from 50-week-old *Ncs1^+/+^* or *Ncs1^-/-^* female mice (G) or 20-week-old *Ncs1^+/+^* or *Ncs1^-/-^* male mice. Scale bar: 1mm (G) and 100 μm (H). Representative images from five (G) or three (H) *Ncs1^+/+^* or *Ncs1^-/-^* mice are shown. Detailed information of the mice is available in Figure 8E-G-H-Source Data.

n.s., not significant; *p < 0.05, **p < 0.01, ***p < 0.001
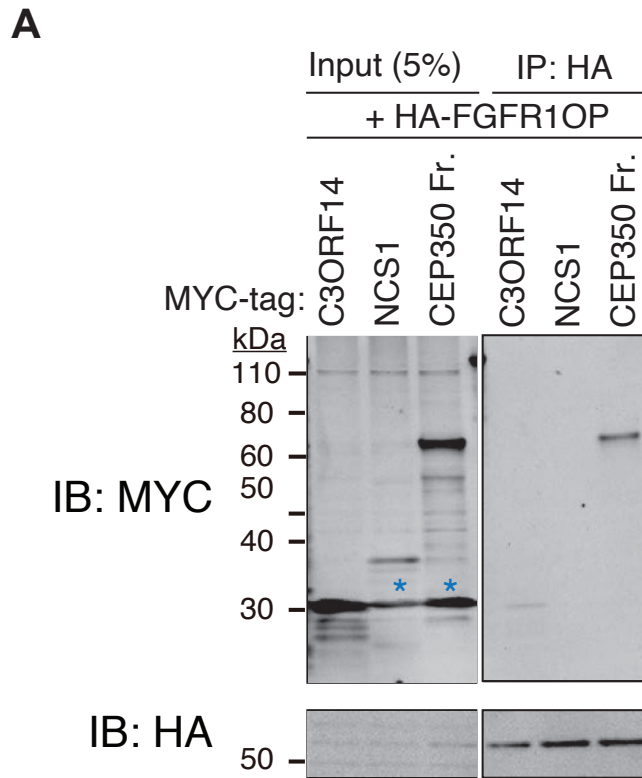
Figure supplements
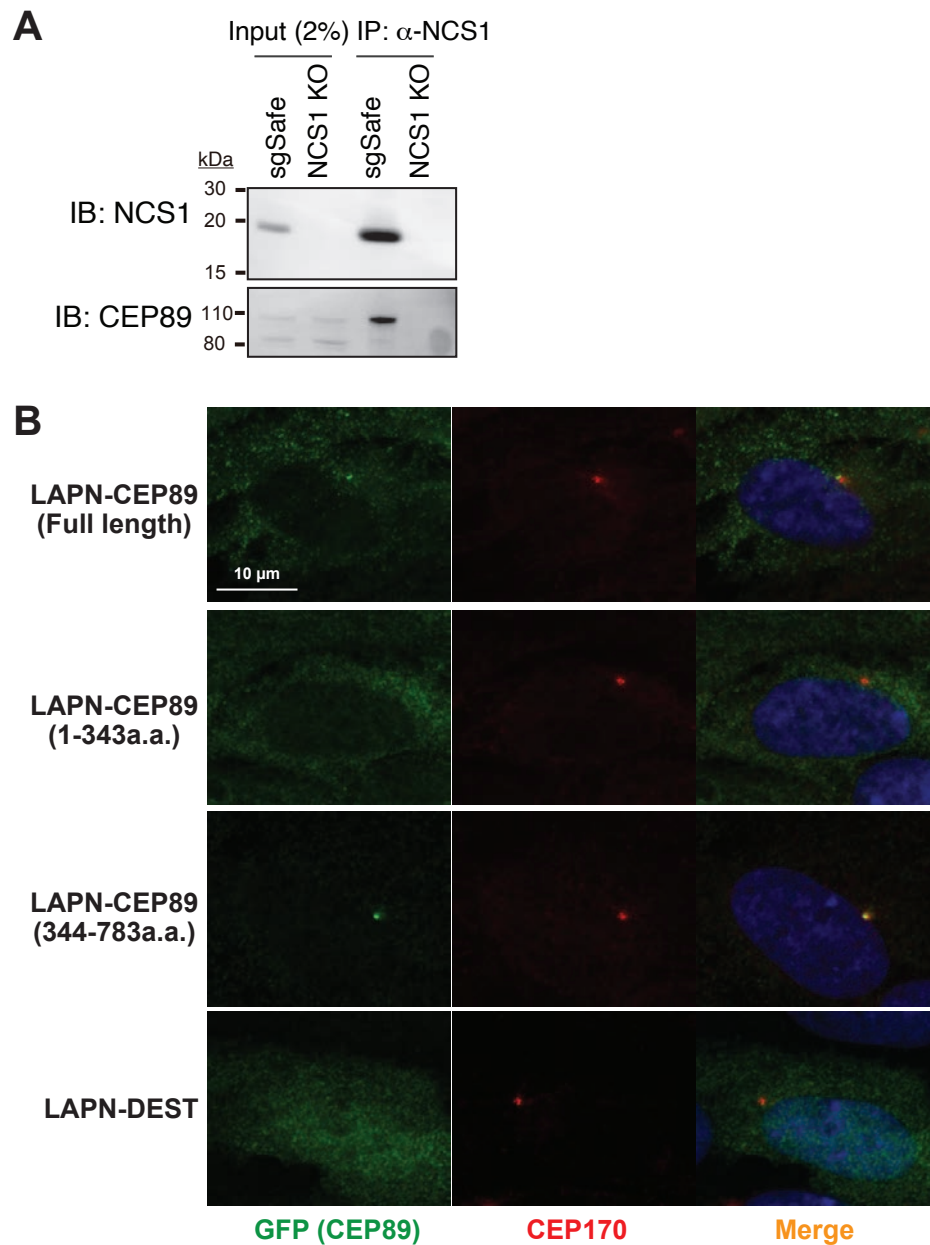
Kanie et al., Figure 1-figure supplement 1

Figure 1-figure supplement 1 *Individual channels of the images shown in Figure 1A.*

A. Immunoblot (IB) analysis of the eluates from co-immunoprecipitation assay of endogenous NCS1 in the control (sgSafe) or NCS1 knockout cells. The eluates were immunoblotted with antibodies against NCS1 or CEP89. Molecular weights (kDa) estimated from a protein marker are indicated.
B. Immunofluorescence images taken via wide-field microscopy. RPE cells expressing the indicated N-terminally LAP (EGFP and S) tagged fragments of CEP89 or LAPN (control) were serum starved for 24 hours, fixed, and stained with antibodies against GFP and CEP170. Scale bar: 10 μm.

1593

Kanie et al., Figure 1-figure supplement 2

Figure 1-figure supplement 2 *A negative control for the experiment shown in Figure 1E and F.*

A. Immunoblot (IB) analysis of the eluates from *in vitro* binding assay of the *in vitro* translated N-terminally HA-tagged FGFR1OP and the indicated N-terminally MYC tagged proteins. The *in vitro* translated proteins were mixed and captured by HA-agarose beads, resolved by SDS-PAGE and immunoblotted with the indicated antibodies. The CEP350 fragment (2470-2836 a.a.), which binds to FGFR1OP efficiently (Kanie et al. 2017) serves as a positive control. Blue asterisks indicate non-specific bands, which overlap with the MYC-tagged C3ORF14. Molecular weights (kDa) estimated from a protein marker are indicated.

1594

A RPE-hTERT expressing LAPN-NCS1-WT
NCS1 localizartion: Cytoplasm, Centriole, Nucleus

B RPE-hTERT expressing LAPN-NCS1-G2A
NCS1 localizartion: Cytoplasm, Centriole, Nucleus

C RPE-hTERT expressing LAPC-NCS1-WT
NCS1 localizartion: ER, Plasma membrane, Nucleus

D RPE-hTERT expressing LAPC-NCS1-G2A
NCS1 localizartion: Cytoplasm, Nucleus
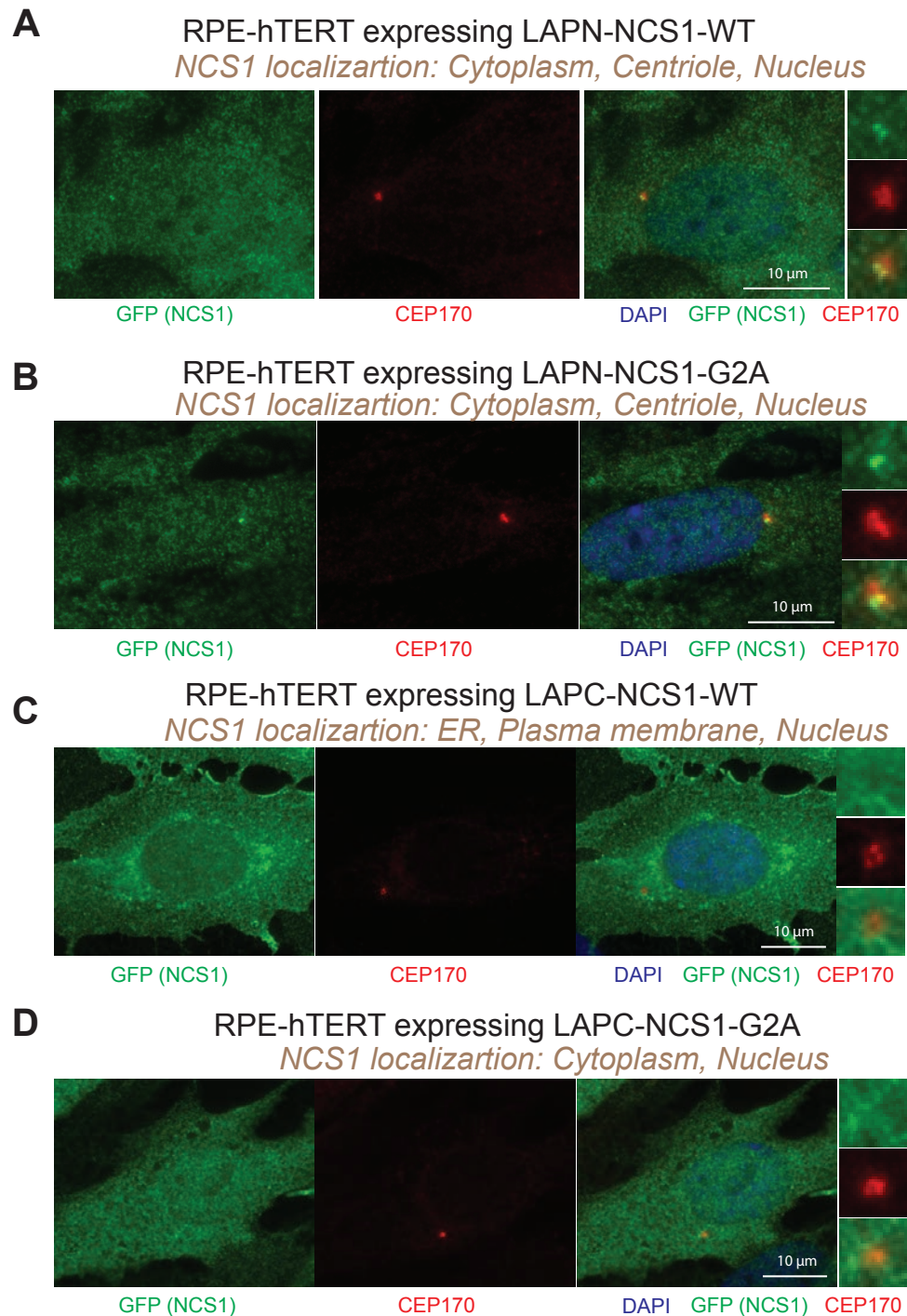
Kanie et al., Figure 2-figure supplement 1

Figure 2-figure supplement 1 *Localization of GFP tagged NCS1.*

A-D. Immunofluorescence images taken via wide-field microscopy. RPE cells expressing N-terminally LAP tagged wilde-type NCS1 (A), N-terminally LAP tagged myristoylation defective mutant (G2A) of NCS1 (B), C-terminally LAP tagged wild-type NCS1 (C), or C-terminally LAP tagged myristoylation defective mutant (G2A) of NCS1 (D) were serum starved for 24 hours, fixed, and stained with indicated antibodies. Scale bar: 10 μm. Insets at the right panels are the enlarged images of the mother centriole. The experimental conditions are available in Figure 2-Figure Supplement 1-Source Data.
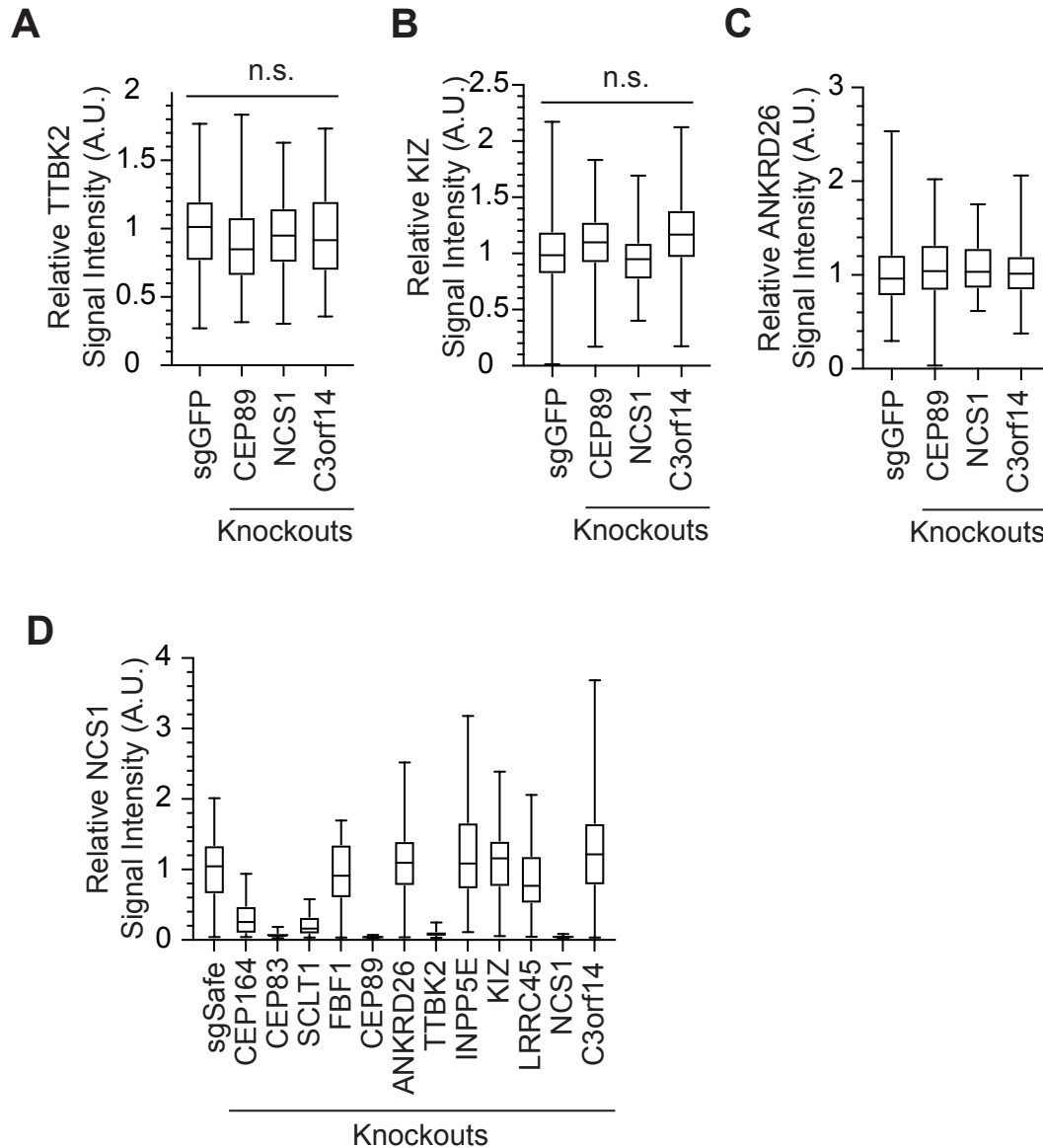
1595
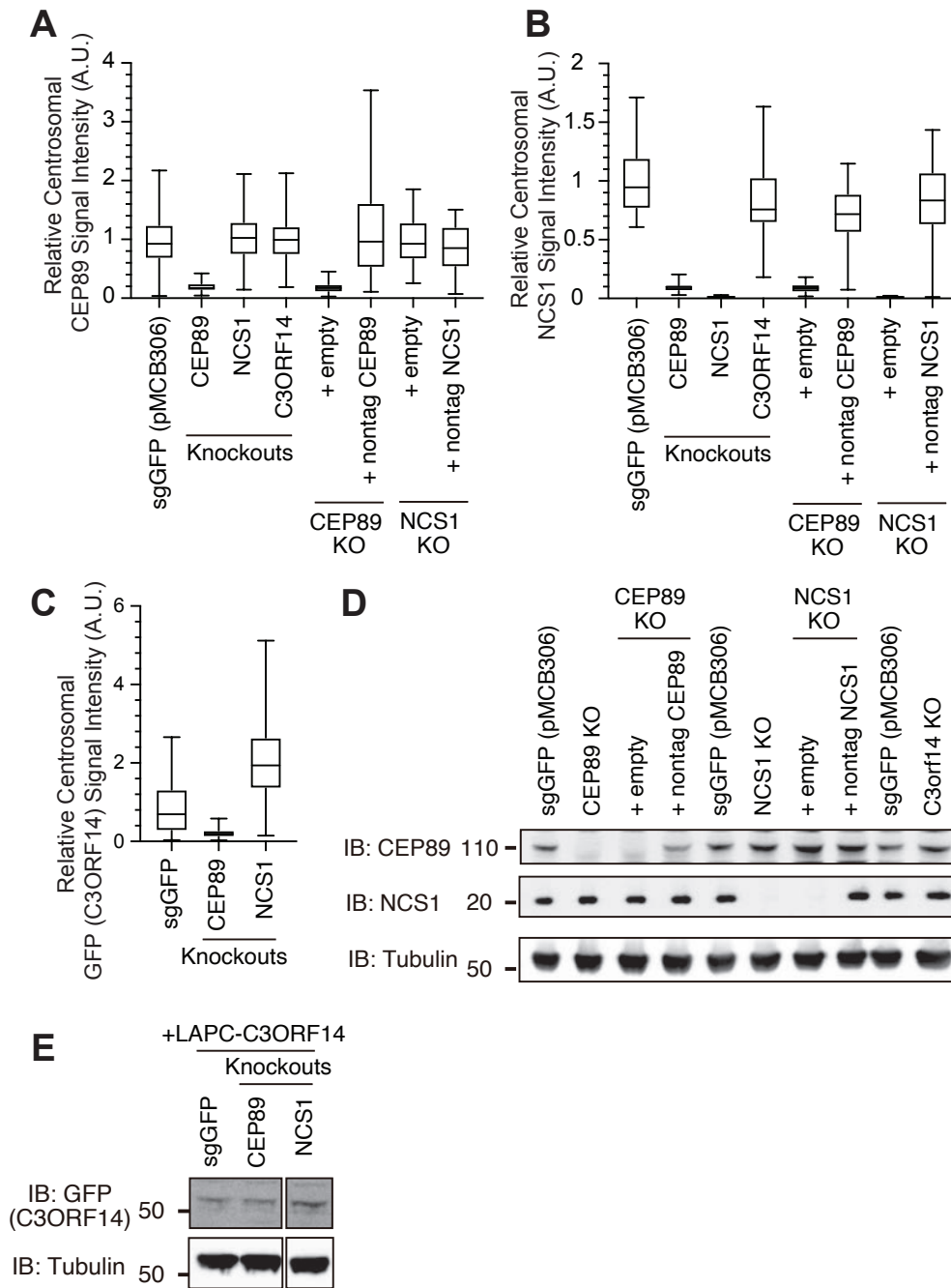
Kanie et al., Figure 2-figure supplement 2

Figure 2-figure supplement 2 *Quantification data and Westen blot related to Figure 2.*

A-C. Box plots showing centrosomal signal intensity of CEP89 (A), NCS1 (B), or GFP-C3ORF14 (C) from the immunofluorescence experiments shown in Fig.2K-M. Data from a representative experiment are shown. A.U., arbitrary units. The raw data and experimental conditions are available in Figure 2-Figure Supplement 2A-C-Source Data.

D-E. Immunoblot (IB) analysis of expression of CEP89, NCS1, and LAPC-C3ORF14 in indicated RPE cells. The cells were serum starved for 24 hours, lysed and analyzed by immunoblot. Molecular weights (kDa) estimated from a protein marker are indicated.

A.U., arbitrary units; n.s., not significant

1596

Kanie et al., Figure 2-figure supplement 3

Figure 2-figure supplement 3 *Localization of distal appendage protein in NCS1 knockouts.*

A-B. Box plots showing centrosomal signal intensity of TTBK2 (A) and KIZ (B) in control (sgGFP), CEP89, NCS1, or C3ORF14 knockout RPE cells. The data combined from three independent experiments. Statistical significance was calculated from nested T test. The raw data, experimental conditions, detailed statistics are available in Figure 2-figure supplement 3A-B-Source data.

C-D. Quantification of centrosomal signal intensity of ANKRD26 (C) and NCS1 (D) in indicated RPE cells. The data from the representative experiment are shown. The raw data and experimental condition are available in the source data of Figure 2-figure supplement 3C-D-Source data.

1597
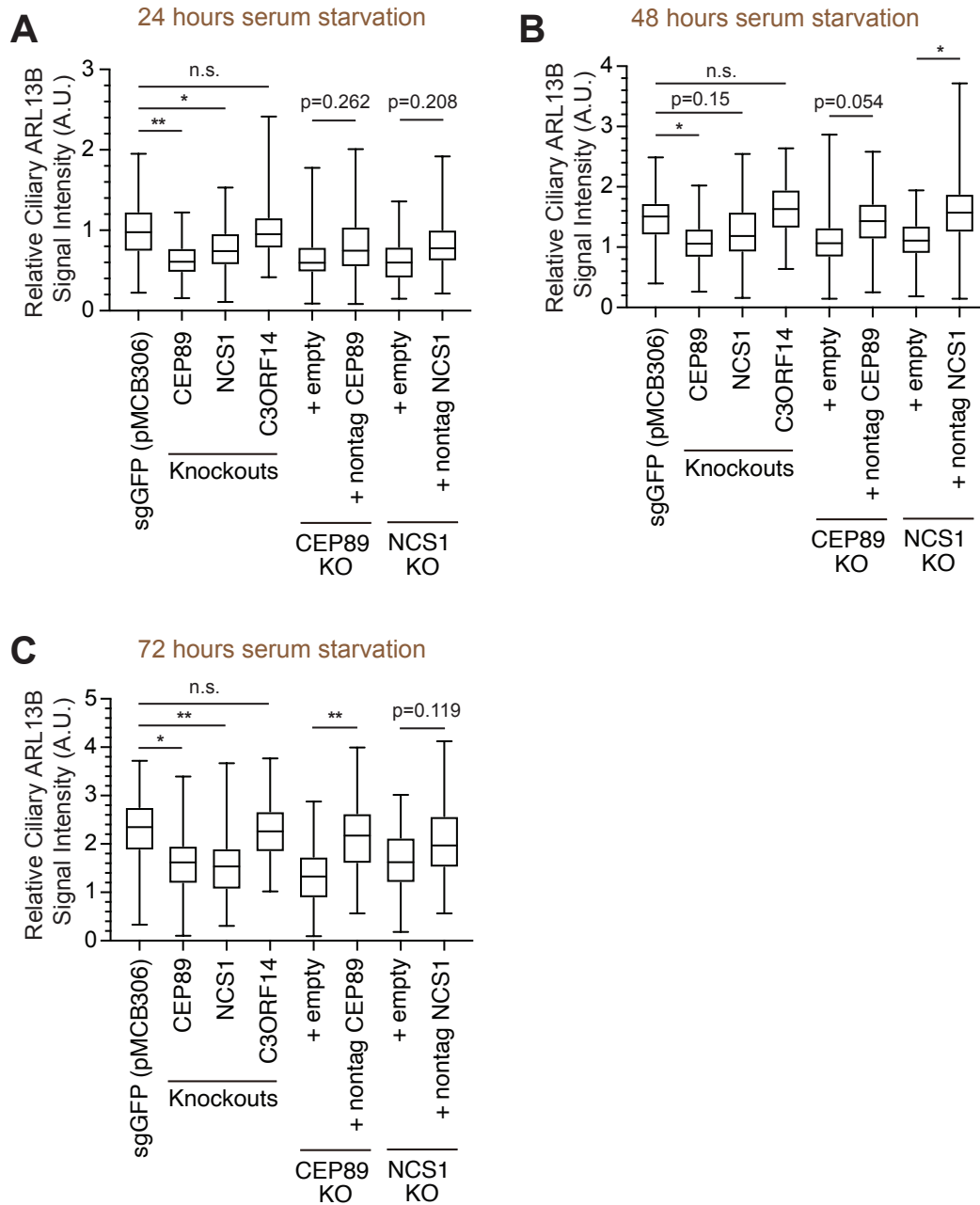
Kanie et al., Figure 3-figure supplement 1

Figure 3-figure supplement 1 *Quantification of ciliary signal intensity of ARL13B in CEP89 and NCS1 knockouts.*

A-C. Quantification of ciliary signal intensity of ARL13B in indicated cells. The cells were serum starved for 24 (A), 48 (B), and 72 (C) hours, fixed, stained with α-ARL13B (cilium marker) and α-CEP170 (centriole marker), and imaged via wide-field microscopy. Data are averaged from three independent experiments. Error bars represent ± SEM. Statistics obtained by One-way ANOVA with Šídák's multiple comparison test. The raw data, experimental conditions, detailed statistics are available in Figure3-figure supplement 1-Source data.

A.U., arbitrary units.

1598
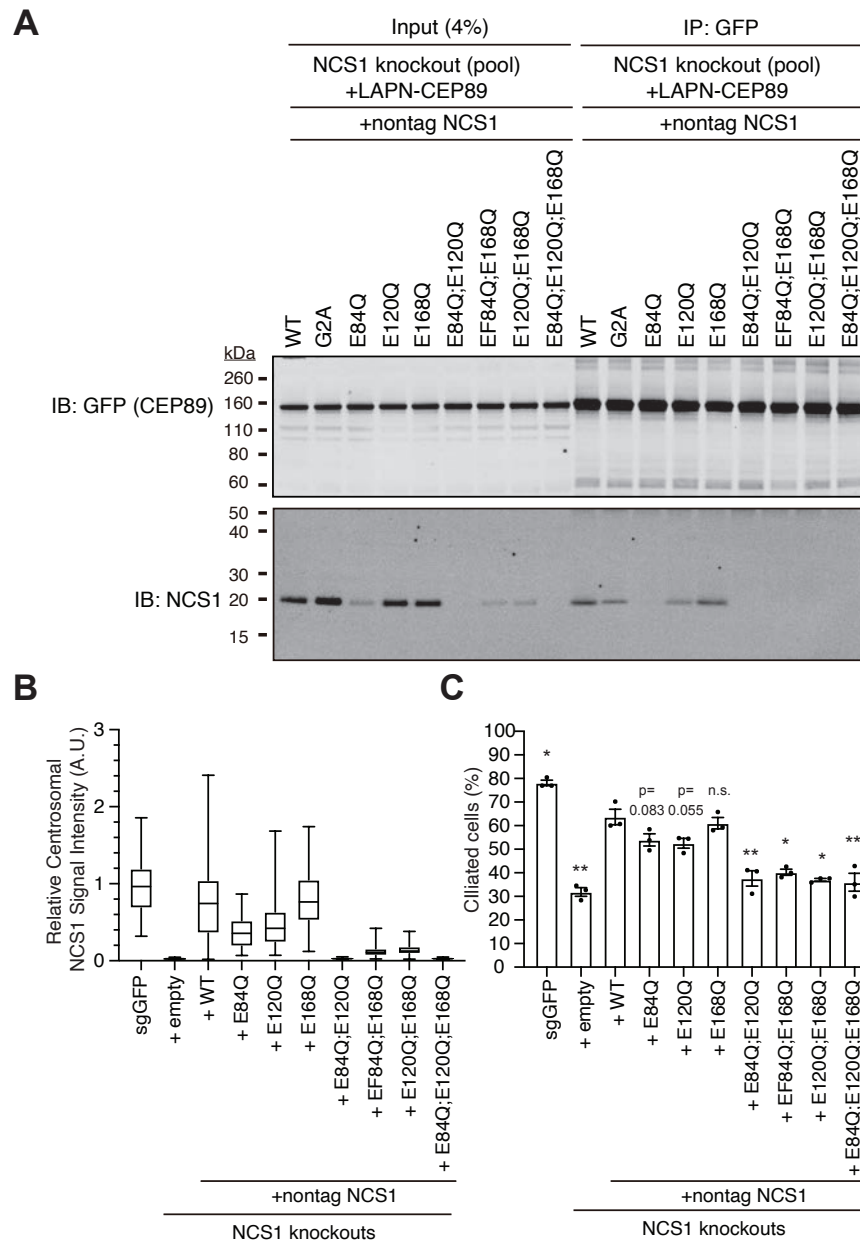
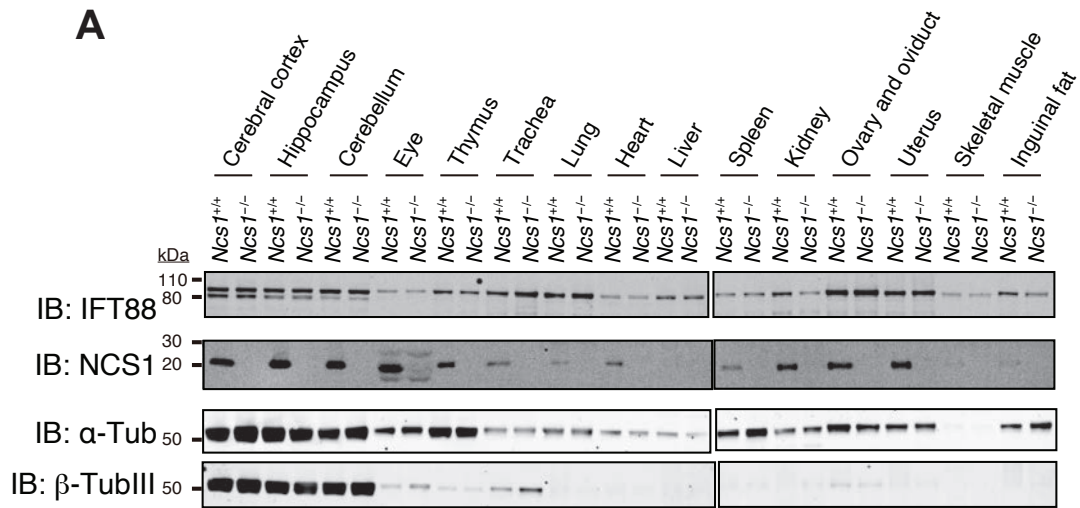Kanie et al., Figure 5-figure supplement 1

Figure 5-figure supplement 1 *Calcium is required mainly for the stability of NCS1.*

A. Immunoblot (IB) analysis of the eluates from co-immunoprecipitation assay of NCS1 knockout RPE cells stably expressing wild-type or indicated point mutants of untagged NCS1 and N-terminally LAP (EGFP and S) tagged CEP89. The cell lysates were co-immunoprecipitated with GFP antibodies, resolved by SDS-PAGE and immunoblotted with indicated antibodies. Molecular weights (kDa) estimated from a protein marker are indicated.

B. Box plots showing centrosomal signal intensity of NCS1. Control (sgGFP) or NCS1 knockout RPE cells stably expressing wild-type or indicated point mutants of NCS1 were serum starved for 24 hours. Cells were fixed and stained with NCS1 antibody. Centrosomal signal intensity of NCS1 was measured from fluorescent images with the method described in Materials and Methods. A.U., arbitrary units. Data from a representative experiment are shown. The raw data and experimental conditions are available in Figure 5-figure supplement 1B-Source data.

C. Cilium formation assay in cells described in (B) serum starved for 24 hours. Data are averaged from three independent experiments, and each black dot indicates the value from the individual experiment. Error bars represent ± SEM. Statistics obtained through comparing between each mutant and wild-type NCS1 by Welch's t-test. The raw data, experimental conditions, and detailed statistics are available in Figure 5-figure supplement 1C-Source data.

n.s., not significant; *p < 0.05, **p < 0.01, ***p < 0.001

A

Kanie et al., Figure 7-figure supplement 1

Figure 7-figure supplement 1 *The expression of NCS1 in various tissues.*

A. Immunoblot (IB) analysis of the indicated tissue lysate from *Ncs1$^{+/+}$* (7-week-old) or *Ncs1$^{-/-}$* (6-week-old) mice. 50 μg (for NCS1 detection) or 12 μg (for detection of other proteins) of each tissue lysate was loaded and analyzed by immunoblot with the indicated antibodies. Molecular weights (kDa) estimated from a protein marker are indicated.

1600
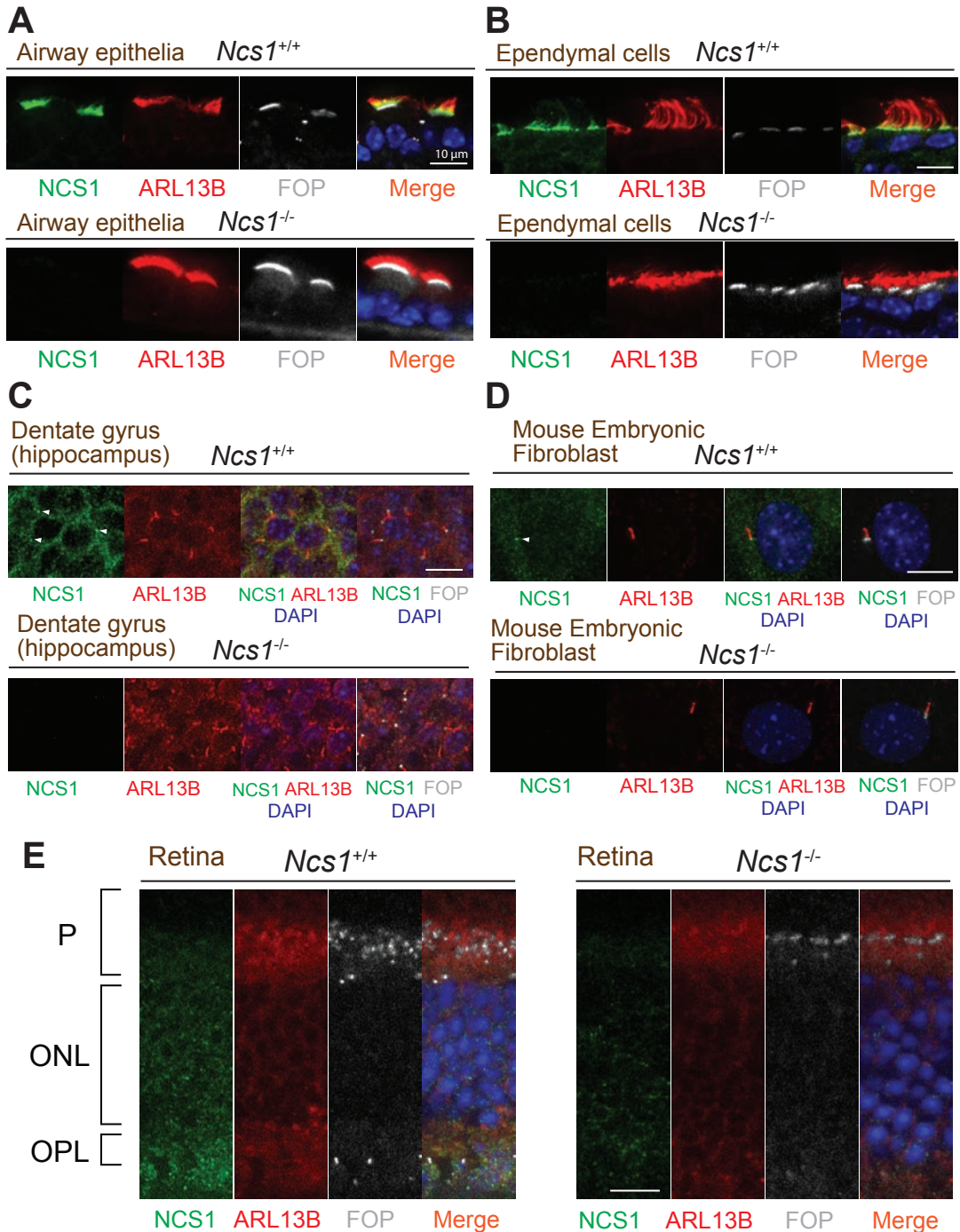
Kanie et al., Figure 7-figure supplement 2

Figure 7-figure supplement 2 *NCS1 localizes to the ciliary base in most ciliated tissues but not in photoreceptor cells.*

A-E. Immunofluorescence images of indicated mouse tissues taken via spinning disk confocal microscopy. Tissue sections prepared from 8-week-old *Ncs1*^{+/+} or *Ncs1*^{-/-} mice with the method described in materials and methods were stained for indicated markers. Arrowheads indicate NCS1 localization. The individual image is from a representative z-slice. Scale bar: 10 μm. P, photoreceptor cell layer; ONL, outer nuclear layer; OPL, outer plexiform layer.

1601
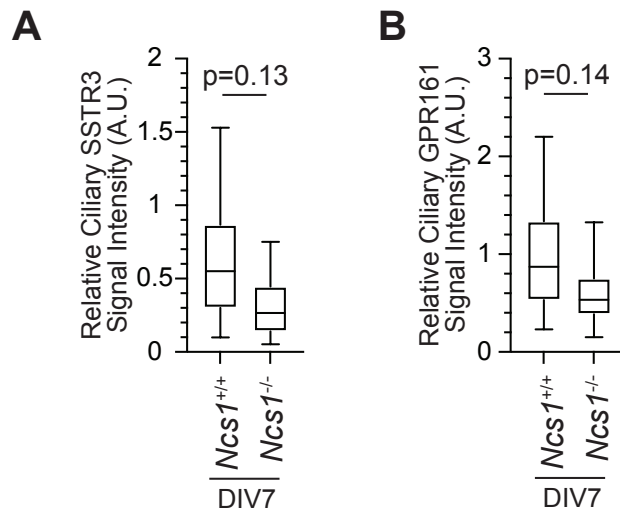
Kanie et al., Fig.7- figure supplement 3

Figure 7-figure supplement 3 *Localization of ciliary GPCRs is mildly decreased in hippocampal neurons prepared from Ncs1$^{-/-}$ mice.*

A-B. Box plots showing ciliary signal intensity of SSTR3 (A) or GPR161 (B) in isolated hippocampal neurons prepared from E18.5 *Ncs1$^{+/+}$* or *Ncs1$^{-/-}$* mouse embryos. The cells were cultured in vitro for 7 days (DIV7), fixed, and stained with either SSTR3 or GPR161 together with α-ARL13B (to mark cilium) and α-FGFR1OP (to mark centriole), and imaged via wide-field microscopy. Data are averaged from five different neurons per genotype for SSTR3 and 3 *Ncs1$^{+/+}$* and 4 *Ncs1$^{-/-}$* neurons for GPR161. Statistical significance was calculated from nested T test. The raw data, experimental conditions, detailed statistics are available in Figure 7-figure supplement 3A-B-Source data.

1602